[redacted] UNCLASSIFIED

[redacted]

Classification Changed
UNCLASSIFIED
JPL - Letter to Authority NASA-Langley
on Nov. 4, 1970, signed by W.E. Hanson
Date: Jan. 4 1971 | By: A. Castarina

Space Programs Summary No. 37-29, Volume II

for the period July 1, 1964 to August 31, 1964

The Planetary – Interplanetary Program

(Title Unclassified)

JET PROPULSION LABORATORY
LIBRARY
JUL 30 1965
CALIFORNIA INSTITUTE OF TECHNOLOGY

508

Copy No._____

JET PROPULSION LABORATORY
CALIFORNIA INSTITUTE OF TECHNOLOGY
PASADENA, CALIFORNIA

September 30, 1964

[redacted] CONFIDENTIAL

[redacted] Downgraded [redacted] intervals;
GROUP [redacted] declassified [redacted] years.

[redacted] UNCLASSIFIED

LAB B01261

1367641

Preface

The *Space Programs Summary* is a six volume, bimonthly publication designed to report on JPL space exploration programs, and related supporting research and advanced development projects. The subtitles of all volumes of the *Space Programs Summary* are:

Vol. I. The Lunar Program (Confidential)

Vol. II. The Planetary–Interplanetary Program (Confidential)

Vol. III. The Deep Space Network (Unclassified)

Vol. IV. Supporting Research and Advanced Development (Unclassified)

Vol. V. Supporting Research and Advanced Development (Confidential)

Vol. VI. Space Exploration Programs and Space Sciences (Unclassified)

The *Space Programs Summary,* Volume VI consists of an unclassified digest of appropriate material from Volumes I, II, and III and a reprint of the space science instrumentation studies of Volumes I and II.

W. H. Pickering, *Director*
Jet Propulsion Laboratory

Space Programs Summary No. 37-29, Volume II

Copyright © 1964, Jet Propulsion Laboratory, California Institute of Technology

Prepared under Contract No. NAS 7-100, National Aeronautics & Space Administration

This [redacted] contains information affecting the national defense of the United States, within the meaning of the [redacted], Section 793 and 794, the transmission or revelation of which [redacted] unauthorized person is prohibited by law.

[redacted] UNCLASSIFIED

Contents

I. *Mariner* Mars 1964 Project 1
A. Introduction 1
B. Systems 2
C. Spacecraft Design 11
D. Guidance and Control 23
E. Telecommunications 37
F. Space Sciences 51
G. Supporting Activities 55
References 57
II. Future Missions 59

UNCLASSIFIED [redacted]

[redacted] UNCLASSIFIED

I. *Mariner* Mars 1964 Project

A. Introduction

The early objective of the Planetary-Interplanetary Program is the initial probing of the planets Mars and Venus by unmanned spacecraft. The initial probing of Venus was successfully accomplished by *Mariner 2*. The next step toward this objective is the initial probing of Mars by *Mariner C* spacecraft planned for the 1964–1965 opportunity.

The primary objective of the *Mariner C* mission (*Mariner* Mars-1964 Project) is to conduct closeup (flyby) scientific observations of the planet Mars during the 1964–1965 opportunity and to transmit the results of these observations back to Earth. The planetary observations should, to the greatest practical extent, provide maximum information about Mars. TV, cosmic dust and a reasonable complement of fields and particles experiments will be carried. In addition, Earth occultation experiment equipment will be carried on spacecraft launched during the Type I trajectory launch period to obtain data relating to the scale height and pressure in the atmosphere of Mars. One spacecraft may be launched on a Type II trajectory and the occultation experiment may be waived on this mission if such action maximizes the probability of success of the total mission.

A secondary objective is to provide experience and knowledge about the performance of the basic engineering equipment of an attitude-stabilized flyby spacecraft during a long duration flight in space farther away from the Sun than the Earth. An additional secondary objective is to perform certain field and/or particle measurements in interplanetary space during the trip and in the vicinity of Mars.

The *Atlas-Agena D* launch vehicle to be used in this project will provide a minimum separated spacecraft weight of 570 lb.

Plans have been made for two launchings of the *Mariner C* design spacecraft from two separate launch pads. All activities will be planned to exploit the limited launch period to the maximum extent. To accomplish this, spacecraft and launch vehicles will be processed in parallel, so that following the launch of the first spacecraft, the second may be launched without delay, no earlier than two days after the first.

The first of the flight spacecraft (*MC-2*) successfully completed its series of tests and was shipped to the Air Force Eastern Test Range (AFETR) for the launch preparation. The test series included many system type

[redacted] UNCLASSIFIED

UNCLASSIFIED [redacted]

qualifying tests such as: (1) 250 hr uninterrupted time in the JPL 25-ft Space Simulator followed by an additional 90 hr in a minimum operational support equipment test cables configuration, (2) vibration of the assembled spacecraft, (3) a "free mode" configuration, where all external cables are disconnected and the spacecraft is powered by solar energy and controlled with its own programmed sequences or by radio command, (4) and a final microscopic inspection of all subsystems with disassembly down to the subchassis level. The *MC-3* spacecraft will be subjected to the same test sequence at a 2-wk interval. *MC-4* spacecraft follows by approximately another 2 wk, but will not see a final inspection or free mode test prior to shipment to the AFETR.

Both *Atlas 288D* and *289D* have arrived at AFETR. The *289D* was erected on Launch Complex (LC) 13 in preparation for the combined system test and safely survived hurricane Cleo. The *MC-2* spacecraft was delayed one day while enroute to AFETR by the hurricane. The first *Agena D 6931* is also at AFETR and *Agena D 6932* is scheduled for shipment early in September.

A series of project review meetings were held including: (1) A final design review on the launch vehicle at Lockheed Missiles and Space Company in early July, (2) A spacecraft review in late July, where all open Problem/Failure Reports and Engineering Change Requirements were covered, (3) A Headquarters quarterly review in the latter part of August, during which time the status of each spacecraft was reviewed and any corrective action was taken. Also the remaining systems, Deep Space Network and launch vehicles were reviewed as to their state of readiness for launch operations, (4) a mission operations planning review was held in August establishing the first launch days as Day 15 (November 4) for LC 13 and Day 17 (November 6) for LC 12. All operations planning was to be based on these days, holding the earlier Day 5 (October 25) as a possibility in the event that one launch complex were made unavailable due to damage from another mission launch. The launch Days 15 through 21 require the use of Type II trajectories; it was found that by making the arrival date July 17 (previous plans for Type II were July 19, 21) and by accepting some penalty in launch energy, it was possible to utilize an aiming point which provides good occultation and good TV coverage.

At the close of this reporting period, no problem areas are known in any of the systems which would preclude launching on schedule.

B. Systems

1. Spaceflight Operations

Mariner Mars 1964 spaceflight operations activities have been directed toward the planning and generation of documents, and participation in tests concerning the spaceflight operations (SFO).

a. Documents.

SFO System Design Specifications (SDS). This document provides a single source of information pertaining to the functional units of the SFO system that are required for the *Mariner* Mars 1964 SFO. A number of rough drafts for this document were generated during July and August 1964.

Spaceflight Operations Plan (SFOP) (EPD-122). The purpose of this document is to define the plans and procedures by which the spaceflight operations will be conducted in both the standard case and anticipated departures from the standard case. Revision 1 of this document was published on August 17, 1964.

b. Tests.

Compatibility tests. These tests are intended to verify the design and the operational compatibility between the spacecraft and the SFO system. The following tests were conducted during July and August 1964, as outlined in the SFO Test Plan (EPD-173, Rev. 1).

Real-time system tests. These tests were conducted during the proof-test model and flight spacecraft system tests on a noninterference basis with the Spacecraft Assembly Facility. The spacecraft transmitted telemetry data, in real time, to the DSIF ground data handling system. The teletype encoder output was then transmitted to the SFOF data processing system in real time via the SFOF communications system. The SFOF received, processed, and displayed, through the various types of output devices, the data being received for examination by the analysis groups.

SFOF 7040/7094 program demonstrations. The purpose of these demonstrations was to exercise all of the user programs, both in the 7040 and in the 7094. These demonstrations acquainted the users (SPAC, SSAC, FPAC) with the program capabilities and restraints. This group of demonstrations was performed during July and August 1964.

UNCLASSIFIED [redacted]

DSIF-SFOF compatibility tests. These tests were employed to verify the compatibility of DSIF Station 11 (Pioneer) with the SFOF using *Mariner* Mars 1964 data. The tests were conducted on August 6 and 24. The August 6 test consisted of processing telemetry through the demodulator and teletype encoder. The August 24 test consisted of processing telemetry through the DSIF S-Band receiver and the demodulator and teletype encoder. The resultant data from both tests were transmitted to the SFOF where a comparison was made with the original data. All anomalies and problem areas were investigated and are being corrected.

SFO training tests. The SFO training tests indoctrinated and exercised the mission-oriented and facility-oriented technical support personnel in the procedures and systems to be used for the mission under both standard and anticipated nonstandard flight conditions. There was a total of five SFO training tests conducted during the month of August 1964.

2. Data Simulation

Since early 1963 the preflight mission simulation capability of the *Mariner* Mars 1964 project has progressed steadily. This capability is being used to develop hardware, and to train personnel. Specifically the objective was to test the SFO system under simulated flight conditions.

Several types of tests are being conducted: (1) compatibility tests exercise the many interfaces within and between the SFO Facility in Pasadena and the worldwide Deep Space Instrumentation Facility (DSIF); (2) training tests familiarize personnel with facilities and procedures to be used during the mission; (3) command procedures tests are designed to develop proficiency in the transmission of spacecraft commands from the SFOF in Pasadena to the DSIF sites for relay to the spacecraft; and (4) facilities integration tests insure proper interaction of all components in the entire complex, including the Air Force Eastern Test Range (AFETR) launch site.

A prime requirement is to simulate the data to be sent from the *Mariner* spacecraft during the actual mission. This will consist of tracking data, antenna angles and received doppler frequency count; and telemetry data, engineering and science experiment measurements transmitted by the spacecraft radio system. Preflight tracking data must, of necessity, be computer generated; telemetry may be derived directly from the spacecraft itself, although this source is of limited usefulness due to the many constraints imposed by the ground environment. For this reason, computer programs are being developed for the generation of both tracking and telemetry data.

Computer programs for the simulation of tracking data are currently based upon the actual programs used in the reduction of tracking data during the mission. In order to render the reduction of this data nontrivial and realistic, discrete known perturbations are added during the simulation process. The end product of the tracking data simulation is a package of data for each test, in the DSIF or AFETR formats. A realistic trajectory is plotted which upon reduction may require a midcourse maneuver or other correction action. These data are played into the SFO complex during the test, with the insertion point being either local or at a remote site, depending largely upon the over-all test objectives. Personnel and facilities in the operations complex process these data as they would during the actual flight. Thus, the communications and data processing equipment are realistically applied, and personnel gain valuable experience in performing their in-flight tasks and analysis.

A more comprehensive tracking data simulator computer program (TDSP) is currently being developed to meet the increasing requirements for providing more realistic tracking data for mission simulation. At this time, tracking data are generated with the JPL orbit determination program (ODP) by means of the generation of a data tape containing prediction information computed by the ODP. This data tape is then read by one of two computer programs (one for AFETR data punching, the other for DSIF data punching), and punched into standard format cards on teletype tape. This current method is somewhat undesirable for the following reasons:

(1) The ODP computers transmit only center-count doppler, while the DSIF stations normally transmit end-count doppler. This makes it necessary to compute angles at a different time tag than the doppler in order to assemble a message in DSIF format.

(2) ODP input restrictions are not compatible with simulation requirements. This is, of course, because the ODP is not primarily a simulation tool and is not designed for easy data simulation. Although a simulation capability is built into the ODP, it is not designed for mission simulation, but for accuracy studies.

(3) There is no adequate way to check out the calculation of the data types in the ODP (other than hand calculation), and therefore an error in these

calculations might not be caught until a mission is flown. Although it might be argued that an independent calculation of the data types in the TDSP is also subject to error, it is unlikely that compensating errors would be made.

(4) Because the ODP must be capable of fitting real data in a reasonable time, approximations are made in certain computations for purposes of speedy computation. Speed is not a prime consideration in the TDSP; therefore more elaborate (and experimental) computation can be performed.

(5) Improved models can easily be added to the TDSP on a modular basis. This is generally undesirable in a flight program, such as the ODP, and is often extremely difficult. These and other considerations make an independent TDSP necessary.

The TDSP will be used primarily as a tracking data simulator for use in conjunction with mission simulations. It will have extended simulation capability unique to this function. Some of these capabilities are:

(1) Simulation of acquisition characteristics such as switching from the acquisition aid to the main antenna, acquisition in one-way, two-way, or three-way, generation of search patterns, etc.

(2) Simulation of powered flight portions of the trajectory such as booster burns, retros, midcourse and terminal burns.

(3) Highly automated operation-automatic view period generation, random failure, etc. Since it is important that inputs to the program be kept to a minimum, many data which are now required as input will be generated automatically.

Computer programs used for the generation of telemetry are not true spacecraft simulators in that they do not calculate the various telemetry measurements from a mathematical model of the spacecraft. Rather, they plan functions and formats which process data tables of the normal time-versus-function value relationships supplied by engineers familiar with each spacecraft subsystem. The computer simulates the commutation function of the spacecraft data encoder, sampling the various measurements in the proper sequence, and with appropriate scaling conversion factors, provides as output a digital magnetic tape having a bit configuration equivalent to the spacecraft bit stream. These resulting data are used to modulate appropriate data and synchronization subcarrier signals in real-time during the SFO tests. For tests involving remote DSIF playback of data, analog recordings of the composite signal described above are supplied to the DSIF sites, where the signal is relayed through the station's data-handling system, the DSIF to Pasadena communications link, and hence into the control and operation facility at JPL. There the data are processed by a control and data-handling system and analyzed in real-time by spacecraft performance analysts. When these data are received concurrently with tracking data, a realistic mission is simulated. In addition to usages during formal tests, these simulated data have proved valuable in checking out operational computer programs and hardware.

Similar simulation programs are actively under way for both *Ranger* and *Surveyor* Projects.

3. Spacecraft Simulator

The function of the spacecraft simulator is one of test for the launch complex facility from the Operation Support Equipment (OSE) launch pad and the blockhouse installation areas to the umbilical connector interface on the spacecraft. It is as its nomenclature implies, the electrical counterpart, simplified to make it a portable piece of test equipment. It is within the capability of one man to carry and operate. The panel layout and chassis view is given in Fig. 1.

The catenary umbilical launch complex cable can be connected to the simulator and all OSE functions and operations can be performed as if a spacecraft were being tested. A list of these functions is given as well as the signal sources and characteristics. The use of the simulator checks the operation of the cabling and its wire conductivity, the umbilical tower junction box and amplifier–signal condition and operation of each of the OSE subsystems as integrated to the spacecraft. Calibration adjustments on equipment can be made from signal sources within the simulator. A compilation of the individual functions of the subsystems is given in Table 1.

Power voltage sources are independently variable. This capability is nonexistent in either the spacecraft or other test equipment.

A form of the air-half umbilical receptacle is mounted in the simulator (Fig. 2). This is accessible under a hinged door in the case. To facilitate mounting, the funnel housing has been removed, since it is not needed. Power connectors and test points are provided under a door on the opposite side of the simulator (Fig. 3).

Table 1. Functions of simulator subsystems

Umbilical connection pin No.	Function	Source	Quantity	Remarks
Power				
8 & 13	2400-cps Inverter Monitor No. 1	Simulator	48 to 52 vac	[a]
17 & 12	2400-cps Inverter Monitor No. 2	Simulator	48 to 52 vac	[a]
21 & 26	400-cps Inverter Monitor 1 ph	Simulator	20 to 32 vac	Square wave 20 μsec rise time[a]
29–32 & 35	400 cps, 3-phase	Simulator	24 to 30.5 vac	
7 & 11	External power supply	OSE	4 amp	
18 & 47	External power supply return			
1 & 3	Battery terminal voltage monitor	Simulator	25 to 36 vdc	[a]
2	Battery charge	OSE	2 amp	Constant current[b]
16	Internal power control	OSE	18 to 36 v	[b]
20	External power control	OSE	18 to 36 v	[b]
25	Power control and indicator return			
5 & 9	Battery temperature monitor	Simulator	Low-med-high	
4	Primary system voltage monitor	Simulator	25 to 50 vdc	On internal supply condition
		OSE	25 to 50 vdc	On external supply condition
Central computer and sequencer				
51 & 52	Relay hold (high and low)	OSE	0.3A/50 Ω	[c]
62	Relay hold high voltage	Simulator		[c]
40 & 43	Inhibit (high and low)	OSE	2.5A/2 Ω	Inhibit high return
46 & 57	Clear (high and low)	OSE	1A/2 Ω	Clear low return[b]
19	L-K5 clear light	Simulator	Ground	2-min delay from clear signal
23	Encounter update	OSE	100 μsec/10 pps	Plus 28-v signal[b]
14	Encounter verify	Simulator	10–30 msec ground	Repeat of each encounter update signal
Data encoder				
68	Event counter reset	OSE	28-v pulse	[b]
64 & 67	Commutator control relay	OSE	28 v	[b]

Umbilical connection pin No.	Function	Source	Quantity	Remarks
Data encoder (Cont'd)				
38	Slow rate sync	Simulator		Signal used to verify reception at OSE from free running multivibrator, and sequentially switched in simulator.
53	Medium rate sync	Simulator		
48	Fast rate sync	Simulator		
31	Bit rate sync	Simulator		
36	Word sync	Simulator		
60 & 65	Telemetry modulation	Simulator		
44	Commutator control	Simulator		
54	Launch mode command	OSE	28-v pulse	[b]
69	Data encoder return			
Pyrotechnic				
15	Pyro arm safe	Simulator	Short	Normally open
28	Pin puller safe	Simulator	Open	Normally closed
24	Pyro return			
Tape recorder				
33–30	Data track step	OSE	Plus 6 v	Pulse—2 to 10 msec[b]
34–37	2.4-kc tape recorder off	OSE	28 v	[b]
58	Recorder launch mode set	OSE	6 v/45 Ω	Reset ret. pos. ON negative off[b]
66	Recorder launch mode reset	OSE	6 v/90 Ω	Set ret. neg. ON positive off
Data automation and science				
61	Tape sync	Simulator	10 μsec/10 kc +5 v	
50	Buffer output	Simulator	50 μsec/10 kc +5 v	
59 & 63	Integrator monitor	Simulator	5 μsec/10 pps +5 on +10 v pedestal	
39 & 6	Scan stimulus	OSE		[b]
42 & 6	TV and NAMG[d] stimulus	OSE		[b]
Radio-frequency				
A	High-gain antenna probe	None		Because of cost, complexities and size these functions have been deferred to external test equipment
B	Precision power output monitor			

[a] Voltage setability and maintainability to exceed 0.5% due to tolerance detectors in OSE.

[b] Simulator lamp operation is given for verification.

[c] The *inhibit* function from the OSE is complemented by a similar one in the simulator representing the separation connector inhibit loop from the *Agena* adapter.

[d] Narrow angle Mars gate.

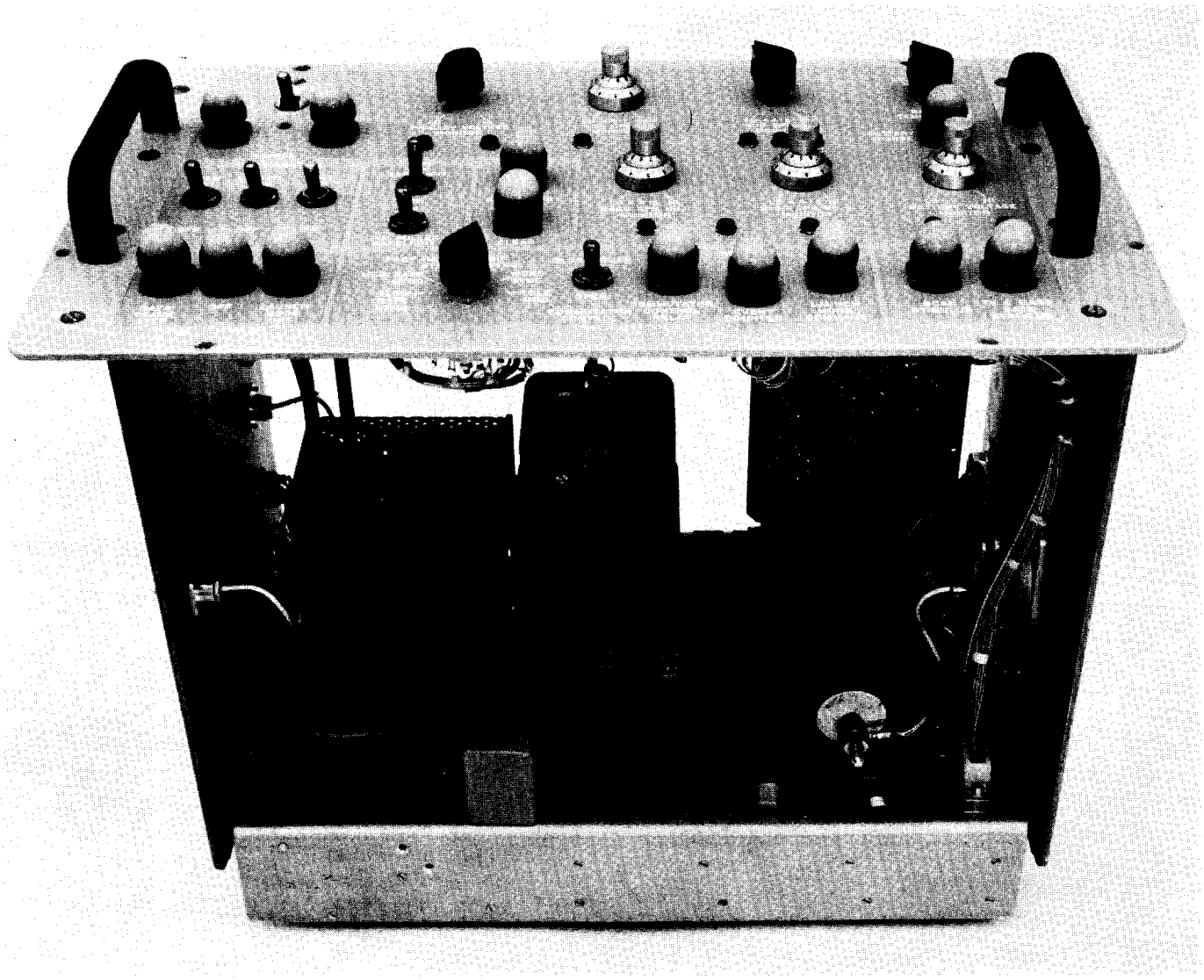

Fig. 1. Panel-chassis assembly

The waterproof case is 18 in. wide, 17½ in. high and 11 in. deep. Cables are stored in a compartment located in the lid, bringing the total weight of the unit to 25 lb.

4. Mariner C-2

The activity during this period included investigations of problems noted on System Test 1, *Agena* matchmate simulated precountdown simulated countdown, and mechanical and electrical updating.

A noise investigation was performed, and the data encoder operational support equipment (OSE) was found to have an oscilloscope improperly terminated. The removal of the ground cleared up the noise.

An investigation was also performed on the updating of the Canopus cone angle with the central computer and sequencer (CC&S) master timer (MT) commands. It was established that the time necessary for sequential commands is 3 sec, and that the problem encountered in system testing with the insertion of the updates was caused by an insufficient amount of time being allowed between sequential commands.

The problems encountered in system testing concerned with power transients that affected the data encoder and radio could not be reproduced during a special investigation. The problem will be reinvestigated when the updated spacecraft is reassembled.

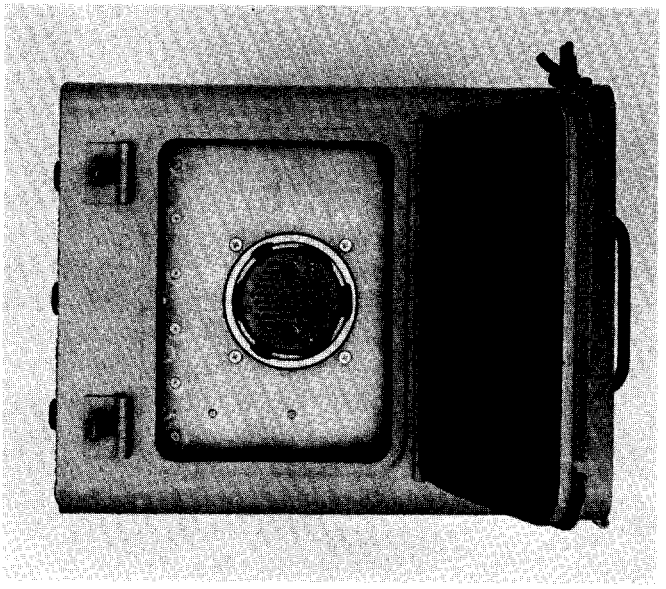

Fig. 2. Spacecraft umbilical receptacle

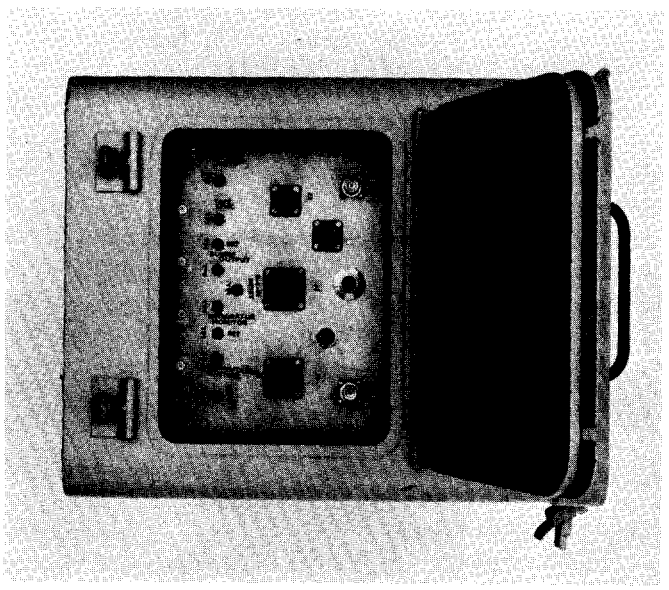

Fig. 3. Power connections and test points

On June 3, 1964 the data-automation-system cosmic ray telescope interface problem was investigated, and the OSE was found to have been partially responsible for the difficulty.

A TV encounter sequence check was performed, and a normal TV fast shutter was obtained.

On June 3 the video storage system was replaced with a flight spare. This was the first step in cycling out the flight tape machines for servicing to meet the requirement of having less than 500 tape passes prior to launch.

On June 5 preparation was started for the first *Agena* matchmate test, which consisted of mating the spacecraft with the *Agena* flight adapter and shroud. Upon completion of the test, the spacecraft was placed in the pit area for the simulated precountdown and countdown.

The formal precountdown was started on June 12 and the simulated countdown on June 13. The problems experienced during precountdown would have delayed the launch, even though ground support equipment, rather than flight equipment, caused the difficulties. Although the OSE would have again called a hold on the launch day, the countdown was very successful. The procedures and personnel were checked out satisfactorily, and the actual countdown procedure was finalized.

The cooling shroud was found to be unnecessary during the dummy run in the air-conditioned building. However, familiarization was established with the installation of the sheath, and time studies have been requested for the mating and demating of the sheath. The length of time of this operation will be a factor in spacecraft turnaround in case of failure.

On June 15 and 16 a matchmate test with the spare adapter and shroud was performed. Some problems in procedures and hardware were discovered which will have to be corrected prior to flight. There is an unacceptable amount of RF leakage in the shroud, and several items will have to be sealed to permit spacecraft purging. In addition, the inflight disconnect was 180 deg out-of-phase, the spacecraft V-band safety straps came in contact with the louvers, the separation-initiated timer bracket was found to be too close to the spacecraft thermal shield, and the transporter hardware boxes interfered with the shroud guide-rail system.

On June 17 updating operations on the spacecraft began in which all engineering change requirements were incorporated.

The attitude-control gas system was installed on June 25. Tedlar cable wrapping replaced much of the Mylar cable wrapping, and power Cases I and VIII were installed on June 29. Proof-test-model Cases V and VI were installed in preparation for System Test 2 conducted July 2 through 4. Inasmuch as the radio cases were held up in the subsystem area due to difficulties in flight-acceptance qualification, a decision was made to proceed with the

system test, utilizing the *Mariner C-1* radio system. This was done to ensure that the remainder of the spacecraft was operating normally so that time in the schedule would not be lost due to other problems.

System test 2 was performed in two parts: Part 1 on July 2 and 3 consisted primarily of engineering exercises. Part 2 on July 3 and 4 consisted of cruise science, radio checks, a normal encounter, playback of one picture and two-lines scan of all other pictures, and a cruise-science statistical data quiet test. The spacecraft was in a flight configuration except for: a nonflight Canopus tracker used in Part 1; the radio subsystem which was a *Mariner C-1* hybrid prototype; and a nonflight nonreal-time automation system. The over-all system test results were satisfactory. Some of the irregularities which occurred were resolved, and hardware which was delivered late was checked.

The TV subsystem camera head assembly was removed upon completion of the system test for inclusion of a new shutter mechanism. Cases V and VI were returned to the proof-test model, and the post-injection propulsion system was returned to the laboratory for substructure modification.

Flight radio cases V and VI were delivered and installed on the spacecraft. The traveling wave tube failed shortly after power was applied. While awaiting resolution of the problem, telemetry calibrations were performed on the receiver and cavity power amplifier. The defective tube was removed after it was found that the collector had a low impedance to frame.

A new TV subsystem shutter and filter combination was installed to eliminate the potential of cold weld, and a vertification test was performed. The new mechanism was found to be marginal, and a decision was made to replace the new shutter with one of the old types that had performed normally in the past.

On July 11 the *Mariner C-1* traveling wave tube was installed on *Mariner C-2*, and a bleeder resistor was incorporated to prevent charge buildup on the collector. The TV subsystem camera head assembly was reinstalled, and the spacecraft was finally delivered to the Space Simulator on July 11 to begin electrical testing.

The spacecraft was suspended in the chamber and all direct-access cables installed. On July 12, spacecraft power was turned on, and a system verification test was performed.

After all difficulties experienced during the system verification test were resolved, the chamber doors were closed and spacecraft power was turned on. The operation was satisfactory until July 15, when it was discovered that the Canopus tracker was not operating properly. Since it was believed that the high-voltage circuitry of the tracker had failed, atmospheric conditions were returned, and a test to verify the cause of the failure was performed. Upon verification the spacecraft power was turned off and the tracker removed. The type-approval tracker was installed, and the verification test was performed satisfactorily. The doors were then closed, a vacuum established, and RF power turned up.

The test sequence was resumed with the post-injection propulsion system maneuver on July 16 and 17; the CC&S MT-1 through MT-6 commands were checked out satisfactorily.

On July 17 the GM 10311 output was found to be erratic. Also, the radio exciters switched during turn-off of the gyros; this usually occurred during the CC&S MT-1 through MT-6 command exercise.

The magnetometer z-axis came out of saturation several times during the early part of the operation. The question is whether the magnitude of the Earth's field, as seen by the magnetometer z-axis sensor, went to a low value or whether the instrument partially failed during these periods. This problem is under investigation.

5. Mariner C-3

During this period the spacecraft assembly continued. Radio Cases V and VI were delivered and installed, and a subsystem test was performed. The gas system, the flight UV photometer, attitude control, post-injection propulsion system, cosmic ray telescope, and louver frames were installed. Attitude control, radio, and science UV photometer subsystem tests were performed. The spacecraft was then prepared for system testing.

System Test 1 was performed on June 5 and 6. Many problems were encountered during the test, whose main objective was to obtain a brief survey of the over-all spacecraft.

Between June 8 and 13 the spacecraft was prepared for matchmate testing. The formal matchmate test was performed with the spare adapter and shroud from June 13 to 15.

UNCLASSIFIED

By June 17 the spacecraft was mated with the flight adapter and shroud, and the spacecraft was prepared for a precountdown. The results of the matchmate tests were comparable to those obtained with *Mariner C-2*.

The formal precountdown test was started June 18. The following difficulties were experienced:

(1) The two coaxial connectors to the catenary were reversed and caused some time delay.

(2) The cosmic dust detector did not reset.

(3) The plasma data had higher values than usual.

(4) The science TV OSE ADCOM caused TV picture noise spots and was replaced by a spare.

(5) The TV lamps were not bright enough, and Direct Command (DC) 16, a narrow-angle acquisition command, had to be utilized.

On June 19 the simulated countdown was successfully performed. The only problem was the receipt of four events in the data encoder registers which were caused by some power transients; this did not cause any holds.

The test team went through the complete normal exercise, including some typical types of holds from the booster and range areas. The spacecraft would have been launched in a real countdown.

From June 20 to 24, problems experienced during System Test 1 were investigated. In addition, some hardware changes were incorporated, mainly in the science area.

Difficulties experienced with the science OSE (including the magnetometer, science isolation box, scan position indicator, and the TV) during System Test 1 were investigated and subsequently corrected.

System Test 2 was performed from June 25 to 27. All flight hardware was installed on the spacecraft except for the Canopus tracker, radio system (dual-cavity amplifiers), prototype magnetometer, prototype science cover, and prototype cosmic-dust detector. The only problems experienced during the test were as follows:

(1) Radio had a low power output, which was known prior to the test.

(2) The cosmic-dust detector was not evaluated since the instrument was a type-approval unit.

(3) The magnetometer operated normally except for z-axis dropout of null during quiet periods, and did not have capability of the 60-gamma nulling steps incorporated in the OSE.

(4) The TV could not be put into fast shutter with the cover lights, and five words were lost at the end of each picture line, in addition to two lines lost at the end of each picture. The *Mariner C-2* TV data also show the loss of the last two lines of each picture, but this is not considered a serious problem.

Note that, during this system test as well as during the *Mariner C-2* System Test 2, the spacecraft radiated off the high-gain antennas. A special piece of flexible coaxial cable was used instead of the normal rigid coaxial, since the latter cannot be easily disconnected from the radio case.

On June 29 the spacecraft equipment was released for completion of engineering change requirements, calibration, and all other outstanding work. The original schedule called for completion of the updating period by July 2, but it was not until July 16 that sufficient equipment was returned to start electrical testing. The gas system, released for modification of the convolutions, was returned July 13. On July 17 power was applied to the spacecraft and the power subsystem was calibrated. The checks indicated that the TV subsystem was not performing properly. The problem, which seems to be in the TV 10-v supply, is being investigated. On July 18 the electrical test continued, and all subsystems reported normal operation, including science and its OSE. The power subsystem completed its telemetry calibrations on July 18.

6. Mariner C Proof-Test Model

The proof-test model (PTM) was prepared for shake on June 2 and 3 and was then moved to the environmental facility. The spacecraft was vibrated in the x-y axis (Bay II, Bay VIII), and no visual damage was observed. On June 4 the spacecraft was vibrated in the z-axis, after which the spacecraft was returned to the Spacecraft Assembly Facility. The results of this vibration test showed that the Canopus tracker with the heavy-gage wire tube was able to survive the environment.

UNCLASSIFIED

Starting June 5, the spacecraft was updated, and all outstanding engineering change requirements were incorporated. The most significant changes incorporated were:

(1) Hybrid radio system.

(2) DC-22, DC-28, and DC-29 circuitry and the appropriate harness changes.

(3) Extensive changes in the power system, including the booster switchover circuitry modifications, which changed the time constant from 10 to 3 sec and the level of switching to 48 v.

(4) New absorptivity standard.

(5) New transformer in the on-board CC&S relay hold module, which has subsequently operated normally for the first time.

On June 12 a special noise investigation was started. The noise between various signal grounds and spacecraft ground was measured and documented. The data encoder susceptibility to half-phase resets and loss of sync in the lower decks was established when the power system was put into and out of boost mode. The known ground loops were interrupted to determine their effect on the data encoder behavior. However, the breaking of the ground loops did not eliminate the sync and half-phase resets. The half-phase resets will probably exist during flight, but are not considered a major problem. The power amplifiers and/or exciter switching with a power transient requires further investigation. The hybrid radio system switches power amplifiers every time the spacecraft boost-mode *on*, *off* commands are issued.

On June 13 one-half of the gas system, Serial No. 23, was removed from the spacecraft for repair of a leak that developed on the bellows. It is estimated that the flexible joint was actuated approximately 65 times. This system was not stress relieved, and the problem may also have been associated with handling.

On June 15 a series of investigations was conducted to determine if the effects of the noise due to high-voltage breakdown could be prevented from disturbing the spacecraft circuitry. The results of these tests indicated that, with appropriate filtering on all lines going to the UV experiment or by isolating the UV photometer cabling, the effects of high-voltage breakdown could be eliminated.

On June 16 the nonreal-time welded data automation system type-approval unit was installed, and the compatibility test between the Space Flight Operations Facility (SFOF) and the spacecraft was started. The first day of testing consisted of twice going through the launch plus the Sun and Canopus acquisition modes; no spacecraft failures occurred. On June 17 two midcourse maneuvers were performed. The first maneuver was aborted by Spacecraft Performance Analysis and Command group (SPAC) due to difficulty in updating their output data. At the end of this day's test, an inadvertent DC-25, an *encounter science on* command, was issued to the spacecraft. The SFOF test director chose to proceed with this nonstandard operation to exercise the SFOF Space Science Analysis and Command (SSAC) and SPAC and the data system. Full recovery was obtained within 1 hr.

On June 18 the spacecraft was exercised through two encounter modes and one playback mode. All spacecraft functions were normal. The SFOF–spacecraft compatibility test was concluded on June 19. The spacecraft was then placed in the cruise mode and the command matrix was tested for SFOF familiarization. The spacecraft operated normally.

A spacecraft logic circuit test was performed from June 23 to 25 to examine in detail the performance of the on-board spacecraft logic concerned with monitoring, switching, and inhibiting functions. Satisfactory results were obtained.

On June 25 the free-mode test procedure was performed while the spacecraft was connected to the system test complex with all direct-access cables. The purpose was to obtain a basis for a comparison of free-mode and cable-mode testing. The spacecraft was then prepared for the free-mode test. This preparation consisted mainly of installing the traveling wave tube which is used in the radio subsystem.

The results of the free-mode test established the compatibility of the solar panels and spacecraft, the ability of the spacecraft to give valid data even though connected to direct-access cables, and the adequacy of the on-board circuitry to operate in a sharing mode with the battery and on full solar power. The test was considered very successful and demonstrated that the transients that affected radio power amplifier and exciter switching, data encoder half-phase resets, and data encoder deck skipping were also present when there were no connections to the OSE.

On June 29 the free-mode configuration was again established to permit the magnetometer personnel an

opportunity of seeing the current-field changes in this configuration. A special Helmholtz coil was used to take the magnetometer sensor out of saturation; the initial results indicate that the current field was insignificant.

From June 30 through July 7 the transfer of radio power amplifiers and exciters, the data encoder half-phase resets, and the deck skipping phenonema which occurred with power transients were investigated. Prior to this investigation, the abnormal behavior of the radio and data encoder would occur in an unpredictable fashion. In certain spacecraft modes, the transient would occur at certain times, but could never be repeated consistently during investigation periods. The investigation during this period established a repeatable method of obtaining abnormal indications in the radio and data encoder subsystems: placing the spacecraft in a share mode between solar power and battery power at a very precise level and then releasing the boost-mode inhibit at the power OSE.

Having established the above control, the investigation was centered around observing the DC-7, change power amplifiers command, and DC-8, change exciters command lines. This investigation showed radio switching to originate in the command isolation pulse switch. Corrective action was taken to lower the resistance of the 10-v power-supply load resistor to the command circuitry from 220 to 1 K which, in turn, desensitized the response of the isolation pulse switch to transients.

The data encoder investigation showed the half-phase reset to originate in the spacecraft harness; the corrective action taken was the disabling of the OSE reset line at the data encoder module.

The deck skip phenonema could not be isolated to a single circuit and are probably the result of cumulative pickup in cable harnessing in general. The removal of any cable harness function from the data encoder causes the data encoder's susceptibility to deck skip to decrease, but no one line by itself showed the same effect. Major design changes would be required to remove this effect, and the problem is not considered serious enough to require such action.

Between July 8 and 10 the half-phase reset, radio system switching, and design changes to eliminate the problem were verified. The incorporated changes seemed to eliminate the problems associated with power transients.

The parameter variation test was started on July 10 after the completion of installation of 60-v zener diodes on the output of the booster regulator in the power subsystem. This test was a rerun of a test conducted on the PTM much earlier in the program. Its objective was to establish if the margins of operation increased as a result of the changes incorporated in the power subsystem. The test consisted of varying the DC input to the 2.4-kc inverters (normally furnished by the booster regulator) and varying the 38.4-kc synchronizer frequency (normally furnished by the CC&S). The spacecraft was operated through five modes of parameter variation, and, in all cases, above-normal spacecraft functions were observed up through but not including encounter. During encounter, the video storage data automation system and TV would not operate properly at the above limits.

The Canopus tracker in *Mariner C-1* operated normally in all of the above tests, as well as on the backup 38.4-kc isolator in the power subsystem and on the free running mode of the power subsystem.

Video storage and encounter science systems were run through a special test at $\pm 2\%$ frequency variations. Performance of all systems was normal. Video storage also worked well when recording at $+2\%$ and playing back at -2%.

C. Spacecraft Design

1. Introduction

The flight spacecraft testing program has proceeded with a minimum of difficulties in the electromechanical and structural areas. Vacuum life tests on the scan actuator, dampers, separation-initiated timer, and pyrotechnic arming switch have begun.

The flight spacecraft weights and centers of gravity have been experimentally determined, and the postinjection propulsion system (PIPS) support structures modified to position the PIPS thrust axis through the spacecraft center of gravity.

A detailed description of the circuit configuration of the *Mariner C* cabling is depicted in the cabling block diagram. The cabling block diagram shows the general arrangement of all spacecraft cables and their routing.

UNCLASSIFIED

The flexibility of the *Mariner C* packaging design and fabrication techniques has enabled late design changes to be incorporated with relative ease. Relatively simple rearrangements of the subassemblies have accommodated changes and additions to the power supplies for the power amplifier and the traveling wave tube (TWT).

The nonreal-time data automation subsystem logic has been redesigned. In the new design, the pellet components have been replaced with standard Hi-Rel components which are packaged in a modular technique. The design provides a relatively high density package which can be readily modified. The new design is 15% heavier and 38% larger in volume than the previous pellet design.

After several failures of the television camera head during vibration tests, an intensive investigation was conducted to determine the destructive frequencies of the vidicon tube when rigidly mounted to the shake table, the vibration environment of the tube when mounted in the camera, and how this environment could be improved. As a result of this work, the ruggedized tube passed the vibration environment when mounted by two compressed foam plastic supports and a spring system which seats the tube face on the focusing ring.

2. Mariner C Cabling

The proposed *Mariner C* cabling system was described in Ref. 1; subsequent issues of the *SPS* have illustrated some of the early hardware (Ref. 2) and described portions of the cabling with respect to packaging, propulsion and structures. This article summarizes the final circuit configuration, which is essentially the same as the proposed system.

In the master block diagram (Fig. 4), eight blocked-off areas, seven rectangular and one circular, are arranged horizontally across the drawing. The rectangular areas represent electronic cases which are located in the peripheral bays of the spacecraft. The circular area represents the postinjection propulsion system which occupies one of the bays. The cabling is represented by small semicircles for connectors and single lines for wire bundles. The cases are numbered and named below each rectangle in Fig. 4. Typically, Case IV, Data Encoder and Command, is shown in Fig. 5.

Two rectangular blocks at the left of Fig. 4 represent the spacecraft battery, inboard of Case VIII, and the coaxial components on Case VI. Four rectangles at the top of Fig. 4 represent the four solar panels, with the small rectangles indicating the electrical equipment mounted on the panels. Also shown is the cabling associated with the solar panel release squibs, gas bottles, and science experiments. At the bottom of the figure, the scan platform and Case V spacecraft receiver coaxial cabling are shown.

The cylindrical connectors from the various case harnesses connect into the upper ring trough (dotted rectangular area extending across Fig. 4) and interconnect the various cases and equipment. Cylindrical connectors are "pigtailed" off the lower ring harness (single line across cases in Fig. 4) and connect into hard-mounted connectors on the case harnesses to pick up leads going to outlying equipment, including the umbilical and inflight connectors, the attitude-control units on the tips of the solar panels, etc. The lower ring harness is attached to the inboard flange of the lower ring structures as shown on the periphery of Fig. 6. Fig. 6 shows the lower ring harness mounted but not yet connected to the bottom of the case harnesses. The upper ring trough is seen in the center background of Fig. 6.

All harness wires are insulated with 0.01-in. wrapped Teflon and use Bendix or Cannon Cinch Hi-Rel connectors. The harnesses have performed well during all tests to date.

3. Packaging

a. General packaging. The advantages of the inherent flexibility of the *Mariner C* packaging design were demonstrated recently by the speed and ease in which changes and additions were made to some of the electronics assemblies. This was especially true for the RF communications assembly (Assembly VI), which was modified to incorporate a traveling wave tube and associated equipment and also for the attitude control and CC&S Assembly (Assembly VII).

With the standard subchassis design, a relatively simple rearrangement of part of Assembly VI accommodated changes and additions to the power supplies for the power amplifier and the TWT (Fig. 7).

Having allowed spare room for contingencies, the traveling wave tube and the attenuator were added to Assembly VI and the relay hold subassembly to Assembly VII without resorting to a rearrangement of existing subassemblies.

UNCLASSIFIED

UNCLASSIFIED

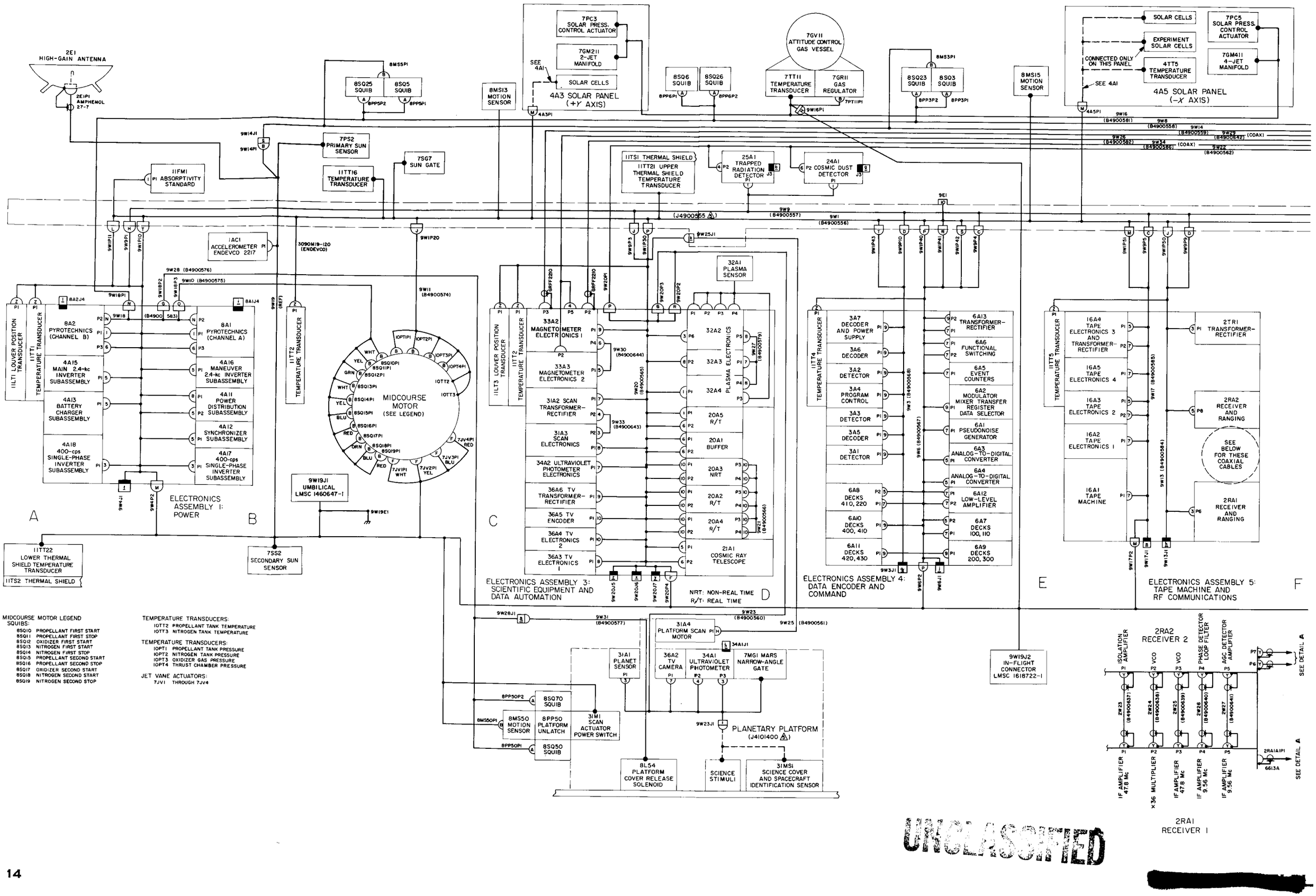

UNCLASSIFIED

[redacted]
UNCLASSIFIED

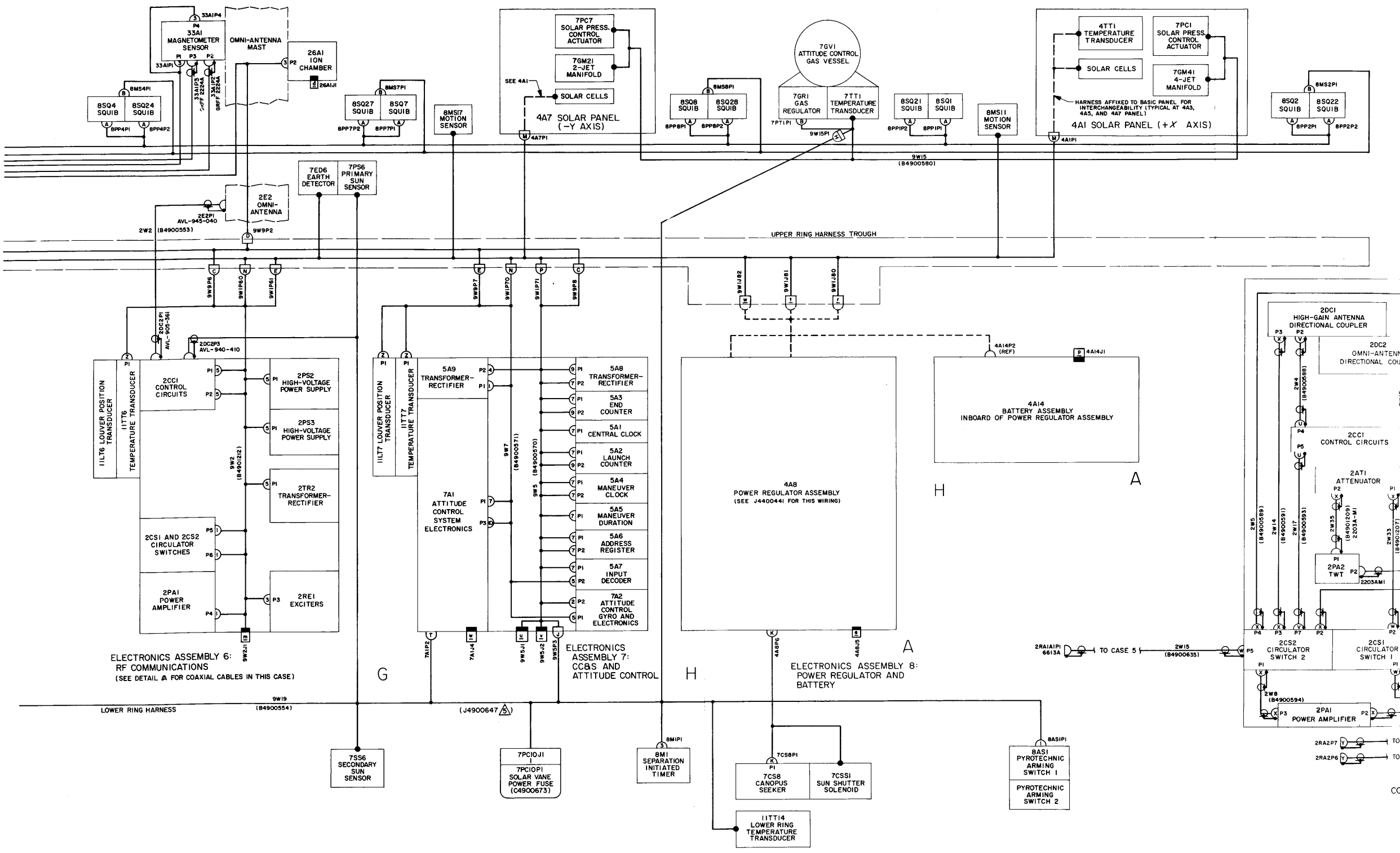

UNCLASSIFIED
[redacted]

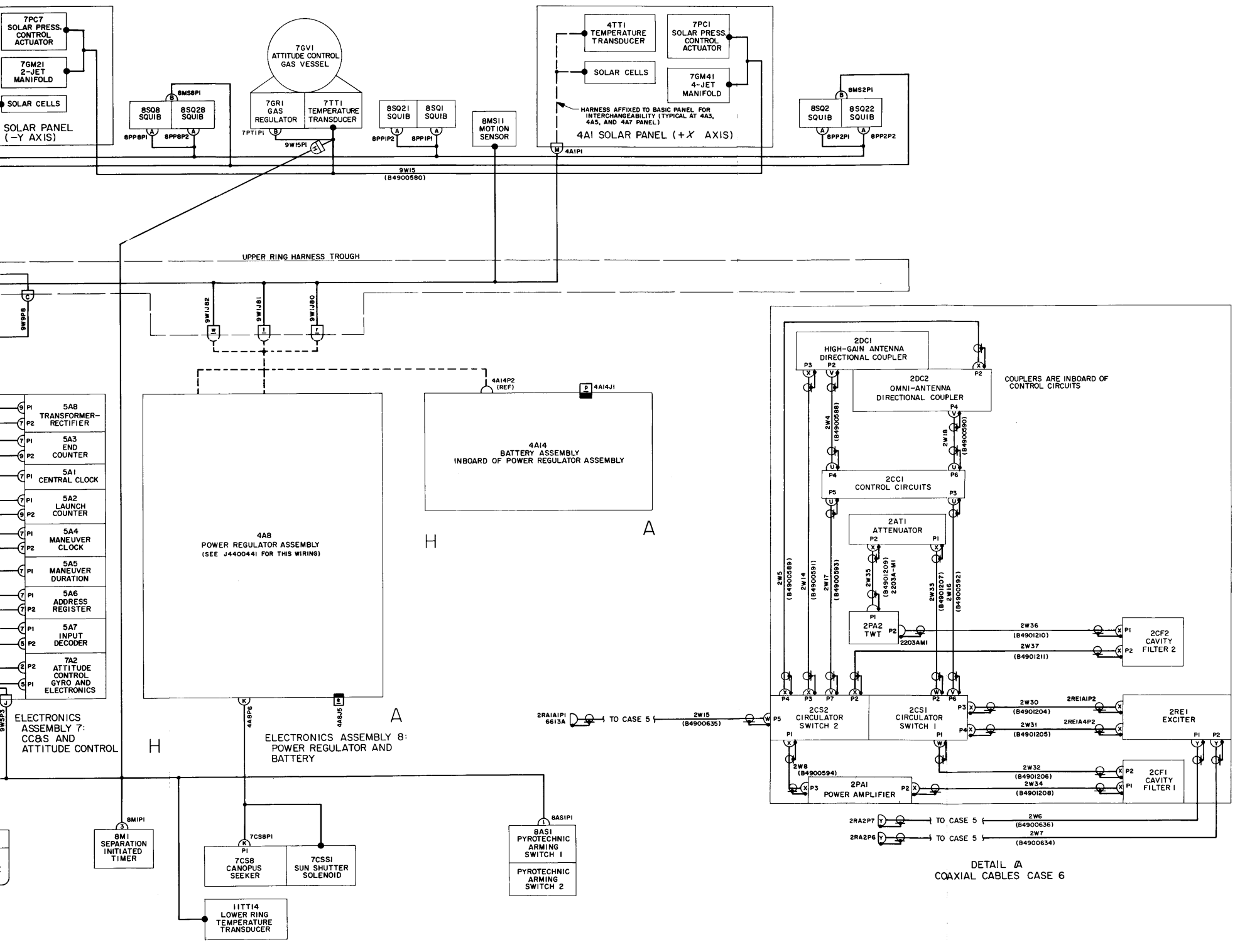

CONNECTOR CODE

"D" SERIES

- (1) DEM-9S-NM-10
- (2) DEM-9P-NM-10
- (3) DAM-15S-NM-10
- (4) DAM-15P-NM-10
- (5) DBM-25S-NM-10
- (6) DBM-25P-NM-10
- (7) DCM-37S-NM-10
- (8) DCM-37P-NM-10
- (9) DDM-50S-NM-10
- (10) DDM-50P-NM-10

"JC06" SERIES

- (A) JC06A-8-2S
- (B) JC06A-8-4S
- (C) JC06A-8-4P
- (D) JC06A-8-4PW
- (E) JC06A-10-6P
- (F) JC06A-12-10S
- (G) JC06A-12-10P
- (H) JC06A-14-19S
- (J) JC06A-14-19P
- (K) JC06A-16-26S
- (L) JC06A-18-32S
- (M) JC06A-18-32P
- (N) JC06A-20-41P
- (O) JC06A-20-41PY
- (P) JC06A-22-55P
- (R) JC06A-22-55PW
- (S) JC06A-22-55PX
- (T) JC06A-24-61P

"JC00" SERIES

- (a) JC00A-8-4S
- (b) JC00P-14-19SY
- (c) JC00A-8-4P
- (d) JC00P-12-10SX
- (e) JC00A-12-10S
- (f) JC00A-12-10SW
- (g) JC00P-14-19SX
- (h) JC00A-14-19S
- (j) JC00A-22-55SZ
- (k) JC00A-14-19SW
- (l) JC00A-14-19P
- (m) JC00A-18-32S
- (n) JC00A-18-32SW
- (p) JC00A-16-23S
- (q) JC00A-18-32SY
- (r) JC00A-18-32P
- (s) JC00A-18-32PW
- (u) JC00A-20-41S
- (v) JC00A-20-41SY
- (w) JC00A-22-55S
- (x) JC00A-22-55SW
- (y) JC00A-22-55SX
- (z) JC00A-22-55SY

OTHERS

- (Z) DUTRON 1207
- (Y) GREMAR 6636
- (X) GRFF 166B-MI
- (W) GRFF 2015A-MI
- (V) GRFF 2221A-MI
- (U) MICRODOT 52-370

1. IN GENERAL, ORIENTATION OF CONNECTORS, ETC., IS CORRECT AND TO BE VIEWED LOOKING OUTBOARD FROM CENTER OF SPACECRAFT
2. CASE LOUVER AND TEMPERATURE TRANSDUCER CONNECTORS ARE PHYSICALLY LOCATED ON CENTERLINE AND TOP OF CASE (SHOWN HERE ON THE SIDE BECAUSE OF SPACE LIMITATIONS)
3. FOLLOWING SYMBOLS ARE USED TO DENOTE DIFFERENCES IN TYPE OF CONNECTOR OR CONNECTION:
   - OSE DIRECT ACCESS JACK
   - "SOLDER IN" OR MECHANICAL CONNECTION (SHOWN AT INVOLVED UNITS ONLY)
   - PLUG (CABLE PLUG)
   - JACK ("HARD MOUNTED" RECEPTACLE)
   - COAXIAL PLUG
4. ALL *MARINER C* CABLING MUST CONFORM TO THIS MASTER CONTROL DOCUMENT

△5 NOTED DRAWINGS SHOW THE MECHANICAL INSTALLATION OF HARNESS (ES) IN THIS AREA
FOR REMAINING HARNESSES SEE CABLING INTEGRATION DRAWING J4900550

Fig. 4. Spacecraft cabling master block diagram

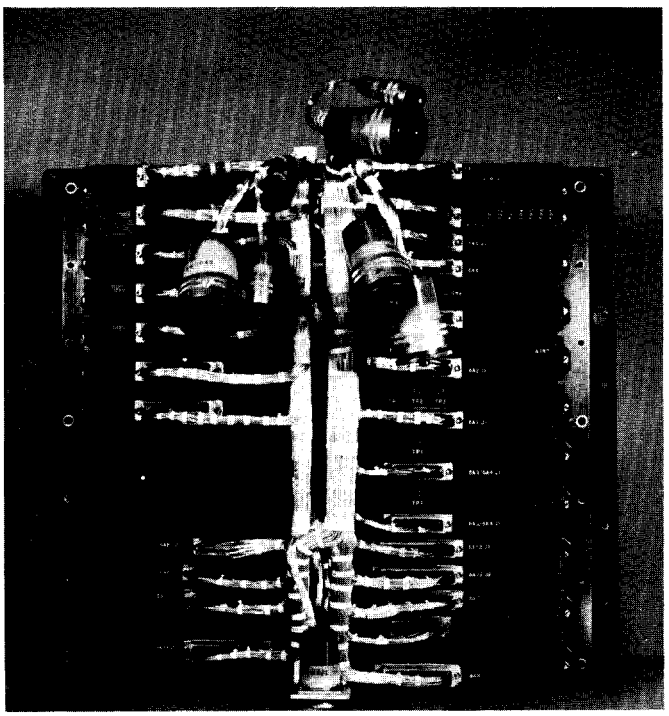

Fig. 5. Case IV data encoder and command

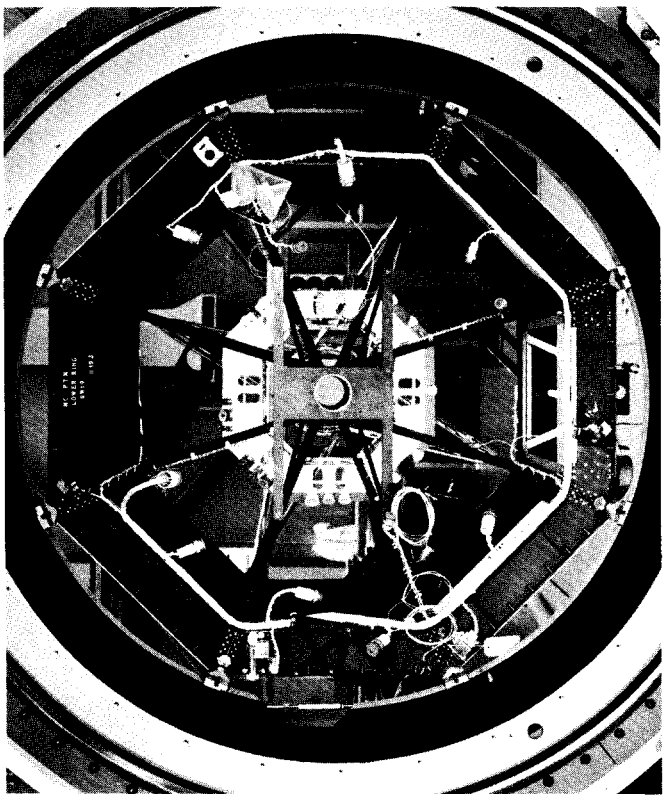

Fig. 6. Upper and lower ring harness

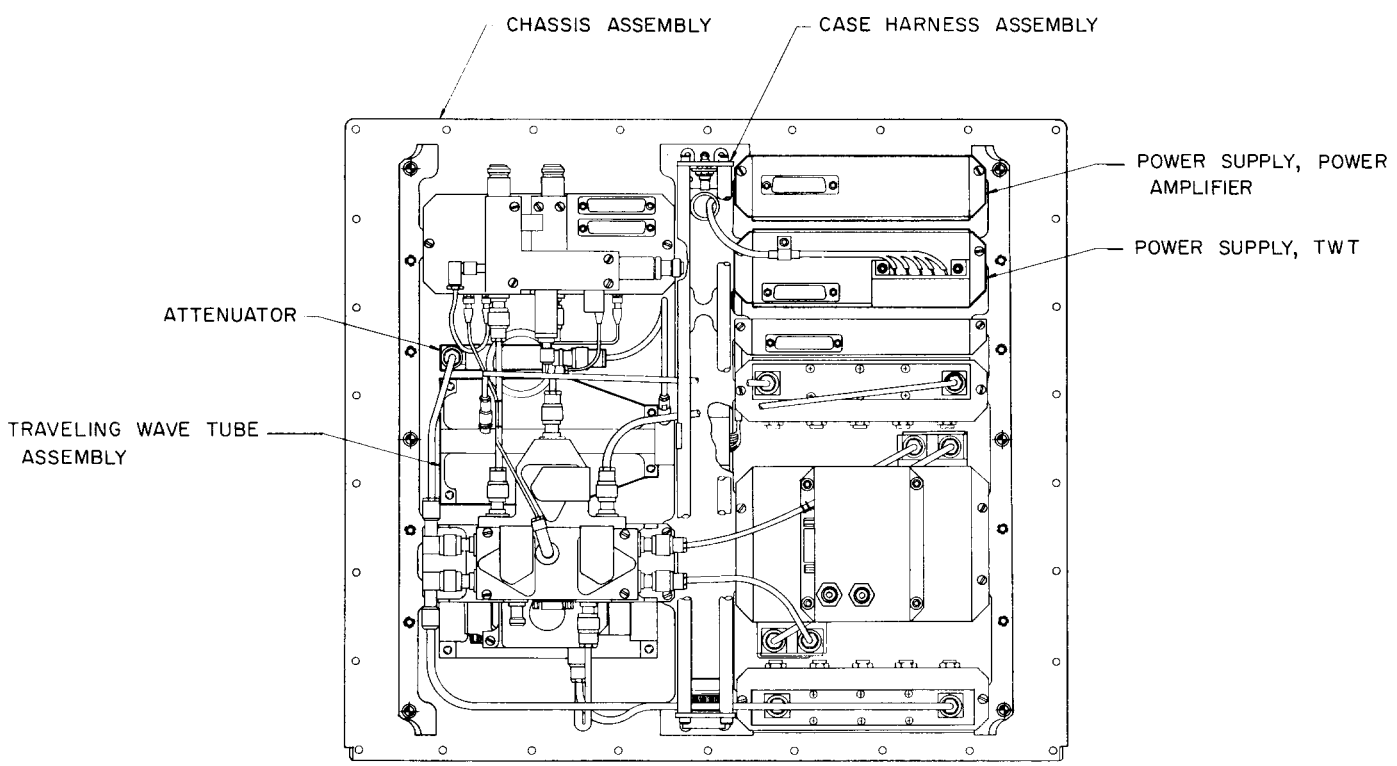

Fig. 7. RF communications assembly electronics Assembly VI

The chassis for six of the individual assemblies (I, III, IV, V, VI, VII) are also of a standard design—the major portion of the fabrication occurring on the standard, with mounting holes for subassemblies added later for the specific chassis. Thus, it was possible to rapidly provide new chassis from the stock of spare standards always held in reserve for just such urgent demand.

b. Electronic equipment handling, storing and shipping. During initial drop tests of the assembly shipping containers at JPL, the container corners cracked. Although no damage occurred to the equipment inside, it was felt necessary to reinforce the corners with caps of the same ABS plastic material. This was accomplished and subsequent tests have shown the reinforcing adequate to withstand the corner drop.

Tests conducted at JPL have shown that the containers do protect the equipment as anticipated from the results of the original vendor's tests outlined in Ref. 3:

(1) During a 30-in. drop test, the shock transmitted to the contents is limited to less than 27 g's.

(2) When subjected to the transportation vibration test of 1 to 3.5 g's RMS from 2–500 cps, the acceleration levels to the contents are limited to less than 4 g's RMS at a resonance of about 8 cps and to about 1 to 4 g's below resonance and less than 0.6 g's above resonance.

c. Welded NRT DAS packaging. The original nonreal-time data automation subsystem logic (NRT DAS) was designed to use pellet components. During fabrication, however, some difficulties were encountered with pellet components and with the processes used. A backup packaging effort using standard components was begun. The design objectives were as follows:

(1) Use standard Hi-Rel components.

(2) Use known fabrication techniques.

(3) Package in a minimum volume.

(4) Provide sufficient flexibility for changes.

The original pellet NRT DAS was packaged in a 6×7 in. subchassis, 1.5 in. wide with cables protruding beyond the subchassis edges. After a review of the available space in the scientific equipment assembly (Assembly III), it was determined that the subchassis width could be increased to 2.34 in. Thus, the packaging task was to replace approximately 2,400 pellet components which required a volume of 71 in.^{3} (considering cable protrusion), with standard components utilizing an available volume of 98 in.^{3}

At the beginning it was recognized that the component interconnection was the main problem to be solved. A geometrical investigation of components and the subchassis configuration showed that three levels of interconnection would be required:

(1) Intercomponent interconnection to form modules of components.

(2) Intermodular connection by interconnect sticks.

(3) Interstick and connector interconnection at the subassembly level by wiring harnesses.

The design that was developed contained the following:

Module design. Two dimensions were maintained constant: 0.5 in. wide and 0.8 in. high, while the length was a floating dimension which was determined by the number of components in the module circuit. The modules were designed for a minimum size while maintaining only one layer of interconnecting ribbon. To accomplish this, the output leads were positioned at random. Fig. 8 shows a typical module prior to embedment. Since both sides of the stick were needed for intermodule interconnection (to save space), it was decided to bring out each output lead on both sides of the modules to maintain design flexibility. The modules then could be designed independently of each other (minimum size 0.5 by 0.8 in. by suitable length, with module leads on both sides).

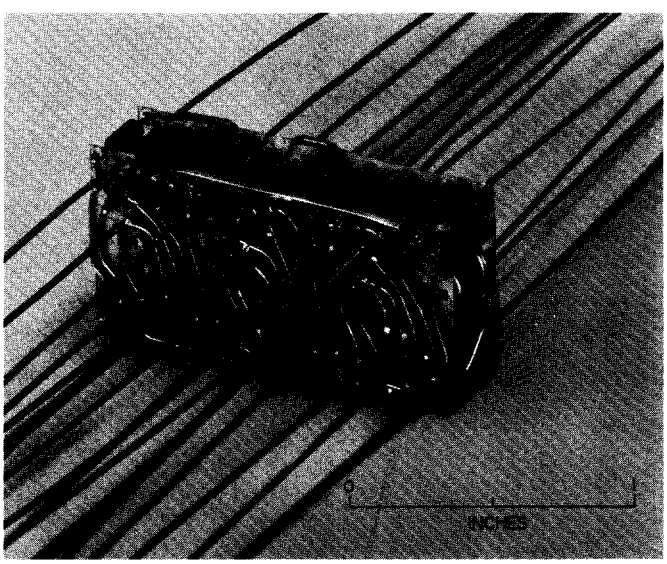

Fig. 8. Typical welded NRT DAS module

[redacted] UNCLASSIFIED

With up to 24 leads positioned at random on each side of the module, a difficult encapsulation problem had to be solved. It was assumed that feeding approximately 24 leads through each of the two mold sides would be difficult. To overcome this problem 0.015 in. thick, predrilled, epoxy glass headers were used which provided lead positioning and photographically etched lead identification, and also functioned as two sides for the mold by clamping the edges. The same mold was suitable for all lengths of modules by simple cutting off the excess length after encapsulation. Fig. 9 shows the mold which was used.

Stick design. Fig. 10 shows two typical stick assemblies. The intermodule interconnections were made by welded ribbon, while the outgoing paths were brought up to bifurcated terminals on the stick terminal board. This design featured soldered connections for connector wiring which allowed ease of modifications, and sufficient room to add components onto the terminal board when changes are introduced.

Subassembly design. Fig. 11 shows the subassembly side, and Fig. 12 shows a typical section through the subassembly. This design provided a relatively high density package which could be readily modified. Interconnecting changes were easy to make by substituting wire, additional components were mounted on bifurcated terminals, and modules could be replaced by the access from the back side.

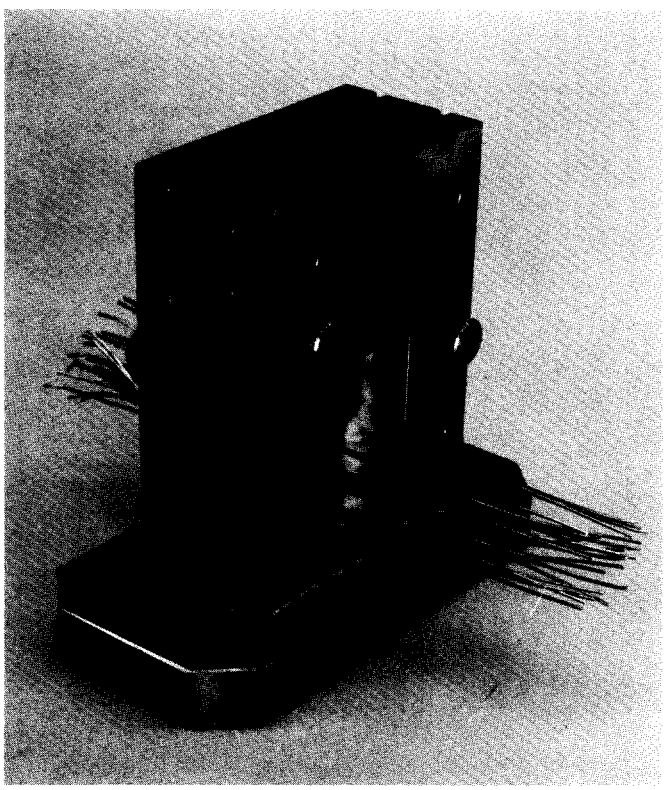

Fig. 9. Typical welded NRT DAS module mold

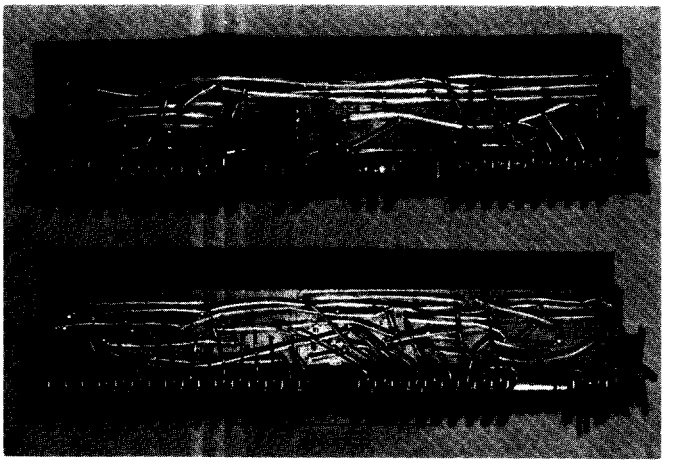

Fig. 10. Typical welded NRT DAS stick

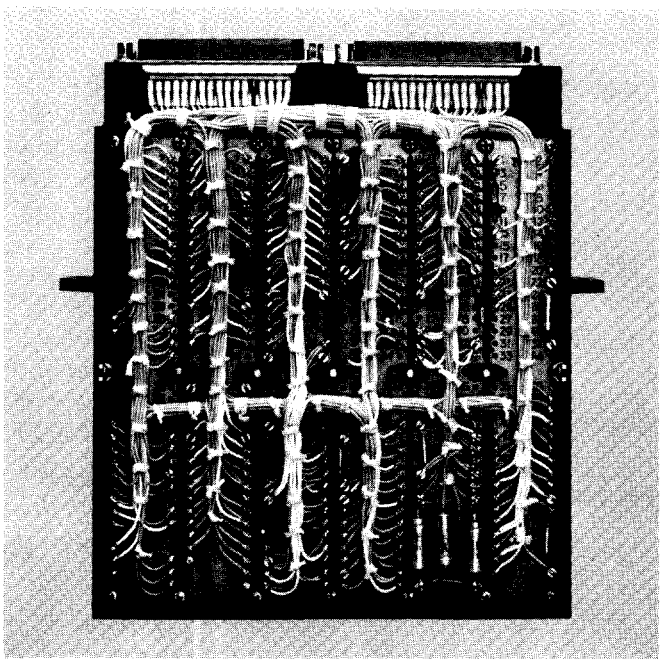

Fig. 11. Welded NRT DAS subassembly

In conclusion, some 2,400 pellet components were replaced with standard ones using known techniques, with only 15% increase in weight and 38% increase in volume.

[redacted] UNCLASSIFIED

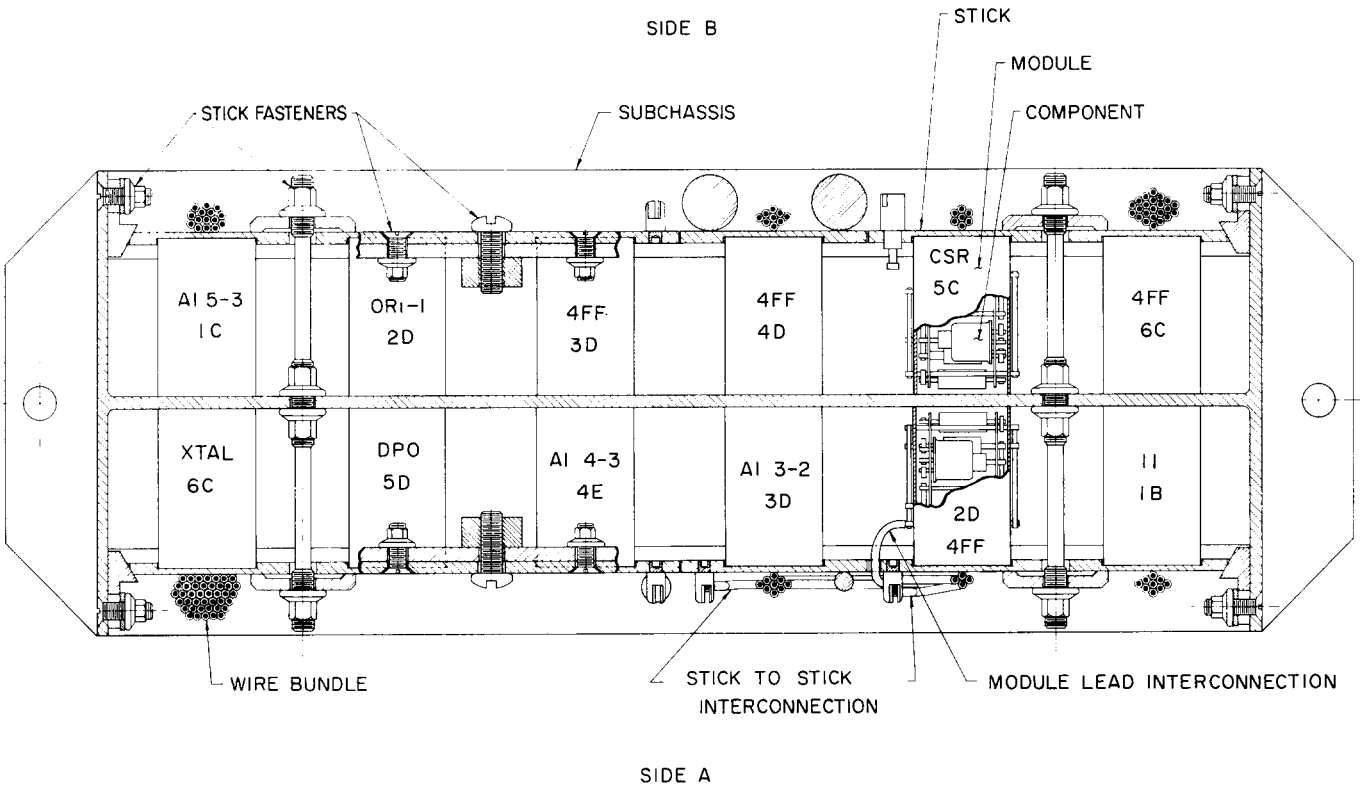

Fig. 12. Typical section through NRT DAS subassembly

d. TV camera head dynamic investigation. The initial hard-mount design for mounting the TV vidicon tube was based on past experiences with *Ranger* tubes and the expected environments. This packaging design was described in Ref. 3. When the TV camera failed to pass the type-approval (TA) test, a thorough investigation of the problem was pursued.

The investigation efforts were concentrated in two distinct areas: (1) to determine the destructive frequencies of the vidicon tube and how it failed, and (2) to determine the vibration environment of the tube in the camera and how this environment could be improved.

Tube failure investigation. A unity gain tube holding fixture was designed to grip the tube solidly but still allow photographic access as shown by Fig. 13.

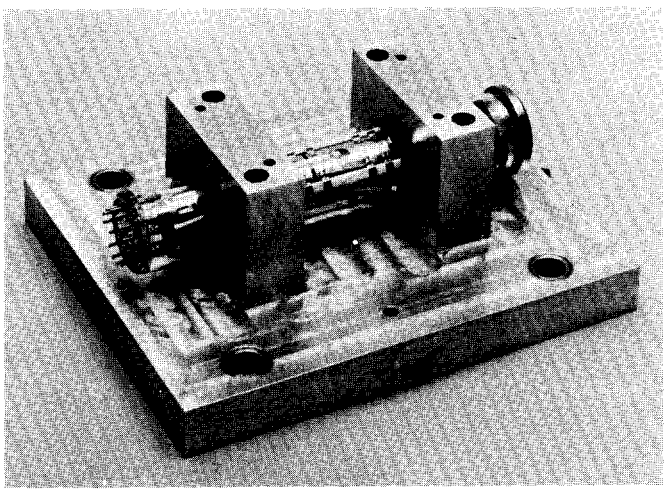

Fig. 13. TV-tube holding fixture

Initial vibration tests made on two *Ranger*-type and one ruggedized *Mariner* tube indicated that the *Mariner* tube was structurally superior to the *Ranger* type.

Tests were made with *Ranger* and ruggedized *Mariner* tubes to isolate the frequency range where failure occurred and to obtain motion pictures of any movements inside the tube. The technique used was to subject the tubes sequentially to elements of the TA vibration spectrum and perform a functional test after each element. The tubes were subjected to the following elements: (1) 16.4-*g* RMS random noise (3 min); and (2) 9-*g* sine sweep at frequencies of 40–500–40 cps for 5 min, 500–1000–500 cps for 1.75 min, and 1000–2000–1000 cps for 1.25 min.

The results indicated: (1) There is a wide variation in the vibration response characteristics in both *Ranger*- and *Mariner*-type tubes from tube to tube, (2) the ruggedized *Mariner*-type tube construction was mechanically superior to the *Ranger* type, and (3) the resonant frequency range of the ruggedized *Mariner* tube was 400–700 cps.

Tube environment and mounting investigation. Concurrently with the tube failure investigation efforts, the hard mounting of the tube and several softer tube mounting designs were analyzed and tested. To obtain the best possible test results, an accurate structural mockup of the vidicon camera chassis was built from flight-type hardware. Accelerometers in three planes were attached to the tube face, the tube socket, and chassis.

Three types of tube mountings were analyzed: the hard mount, the O-ring, and an experimental soft mount.

In the hard-mounted tube the vidicon tube face is firmly fastened to the focusing mount by use of a ring which is bonded to the glass envelope, close to the face, and a compression band to hold the face against the focusing mount. After attaching the face, the socket end of the tube is carefully fastened to the chassis to avoid stresses on the face.

For the O-ring tube mounting design the tube is supported at each end in two Teflon O-rings by two collet-type clamps. Grooves in the collets form an interference fit with the O-rings, and metal clamps supply additional grip. A diaphragm spring pushes on the tube socket to supply an axial force which seats the tube face against the focusing mount.

An experimental soft-mount design had the tube suspended in the center of a metal cylinder by 0.06-in. thick resilient potting of a metal cylinder by 0.06-in. thick resilient potting material. The cylinder is clamped onto the existing focusing mount and at the socket end to the chassis so that there are no metal-to-glass contacts.

Although these initial tests of the tube-to-chassis mounting methods showed that the experimental soft mount protected the tube best (Fig. 14), it was felt that the complexities of this design would make it very difficult to prove out and incorporate within the program schedule.

It was suspected that the damaging 400–500 cps resonance experienced by the hard mount was actually introduced by the test fixture. A hard-mounted tube had successfully passed a TA vibration test when installed on a spacecraft.

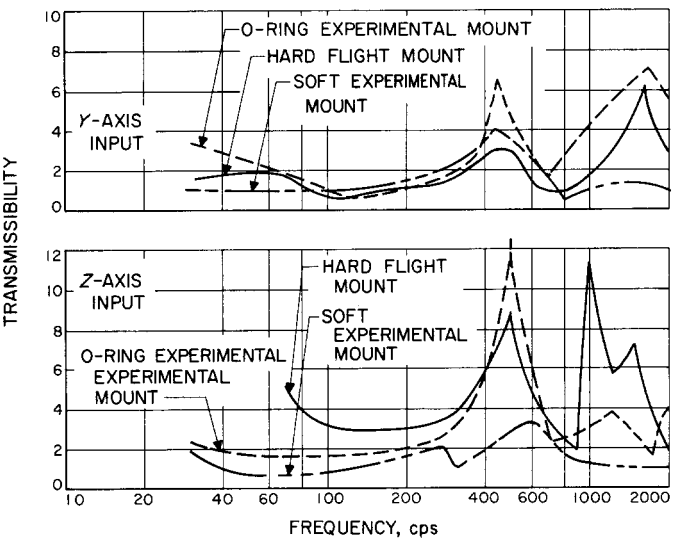

Fig. 14. Comparison of tube mounts tested on hard fixture *Mariner C* vidicon camera

All this prompted the decision to emphasize testing the available hard mount to realistic spacecraft levels to prove the adequacy of the design.

Test fixtures and test methods. The original TA block test fixture is shown in Fig. 15. A similar, but vertical block test fixture reduced the cross-coupling introduced by the 60-deg angle of the TA block test fixture. Each of these fixtures were used to evaluate the hard-tube mount and the O-ring and experimental soft mounts.

A comparison of data from tube mount and spacecraft science platform vibration tests showed that the platform

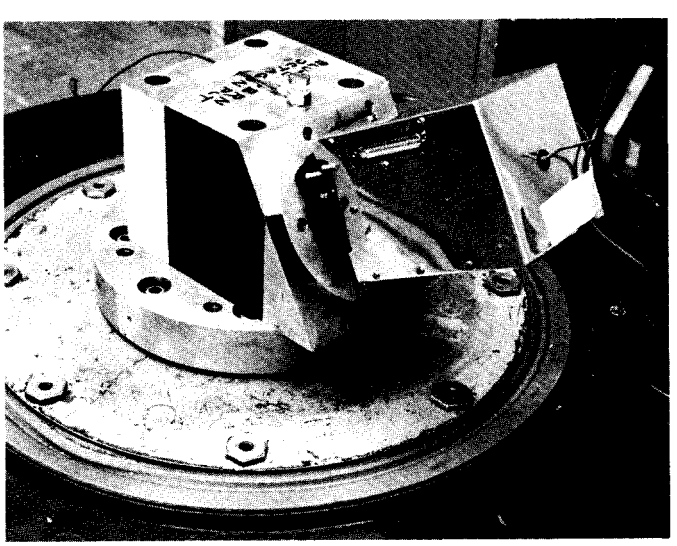

Fig. 15. TV camera head TA test fixture

apparently isolated the TV camera at its resonance of 400–500 cps. Thus, the TA block test fixture was producing transmissibilities higher than could be expected on the spacecraft and the need for a more realistic test fixture was evident.

The first attempt was to use an actual science platform as shown in Fig. 16. Initial low level exploratory sine sweeps indicated that bearing clearance, torsional retention clearance, fixture tie down and cg location all contributed to unrealistic simulation of platform response.

A special fixture was built to hold the science platform firmly (Fig. 17). The stability of this fixture preserved the science platform vibration isolation features and allowed control of the vibration input to be successfully moved from the table to the platform itself which then allowed vibrating the platform, in the plane of shake, in a manner closely simulating the actual spacecraft performance.

It became necessary, however, to limit excessive cross-coupling. A special peak control circuit was used to force either of the cross axis accelerometers on the platform to take over the control whenever the TA level was exceeded. These techniques provided a more realistic sinusoidal vibration simulation and resulted in drastic reduction of response at the tube socket. Typical z-axis response is shown in Fig. 18.

Control of noise levels in a similar manner was attempted but was unsuccessful due to the inability to control cross-coupling.

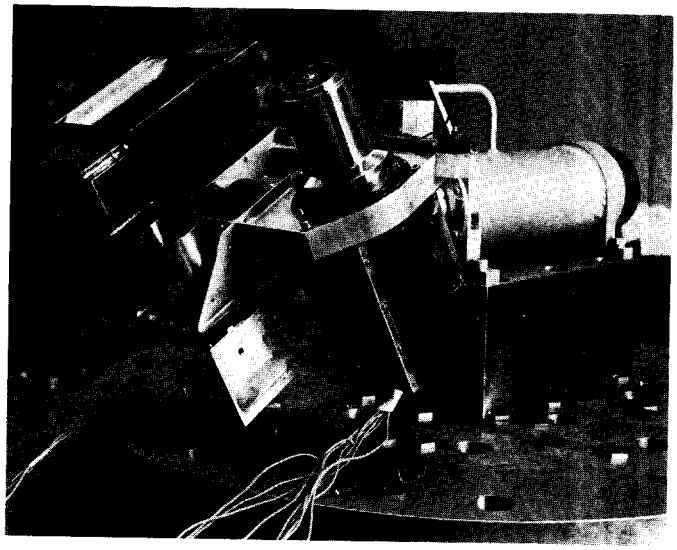

Fig. 16. Vidicon assembly on science platform

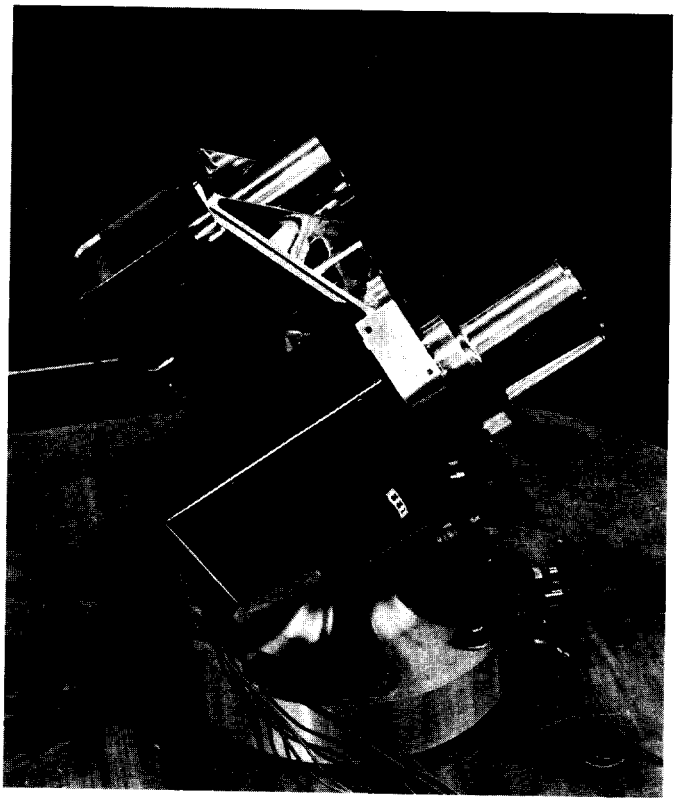

Fig. 17. Vidicon assembly modified test mount

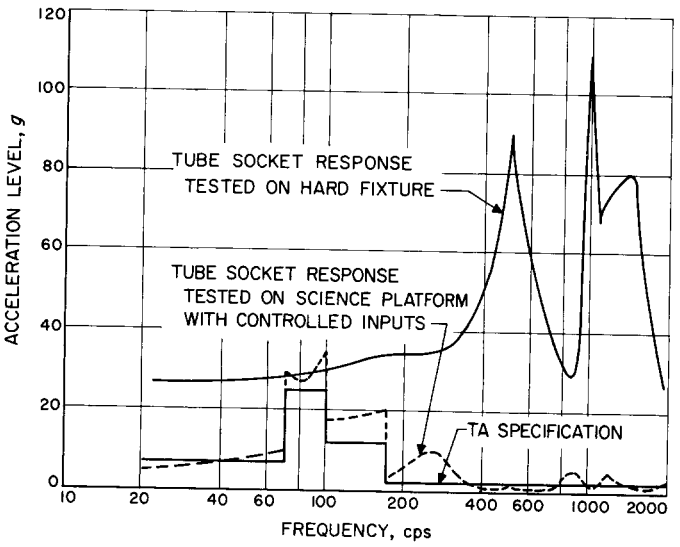

Fig. 18. Z-axis vibration tests, acceleration versus frequency, *Mariner* C vidicon camera

To prove out the hard-tube mounting, a ruggedized *Mariner* tube was subjected successfully to the TA sinusoidal environment. However, during noise testing, the cross-coupling overstressed the tube. Subsequent detail

analysis of failure showed that the tube tester socket was faulty, and the tube was still operable although damaged.

At this time a ruggedized tube in a new soft mount successfully passed the TA sinusoidal and noise tests in the more severe environment of the block test fixture. The mounting method was developed through a parallel effort and consisted of two compressed foam plastic supports and a spring system which seated the tube face on the focusing ring. The configuration is shown in Fig. 19.

The new soft-mount design provided an extra margin of safety and was the first TV camera configuration which passed all the vibration tests. The project schedule did not permit further investigations, and so this success was immediately applied to flight hardware. In summary, the investigation led to the following conclusions:

(1) Block-style vibration test fixtures are easy to use, but at times they introduce very high gains into the system which are not representative of flight environment.

(2) The ruggedized *Mariner* tube was found to be superior to the original tube and was, therefore, adopted for flight.

(3) The original hard-mounted tube design was satisfactory but required very difficult testing procedures.

(4) The new soft mount provided better over-all safety margins.

D. Guidance and Control

1. Spacecraft Power System

a. Hardware status. All anticipated Engineering Change Requirements (ECR's) have been written and incorporated into the flight hardware. All flight units and all spares—except the flight batteries which will be delivered directly to AFETR—are in the Spacecraft Assembly Facility.

b. System testing. Type-approval (TA) testing of the power conversion subsystem again after incorporation of several ECR's has been successfully completed. The TA Cases I and VIII have now started life tests. For the conversion equipment, life testing consists of operating the system under conditions of vacuum and temperature extremes. In order to accelerate failure modes, the temperature profile shown in Fig. 20 is followed.

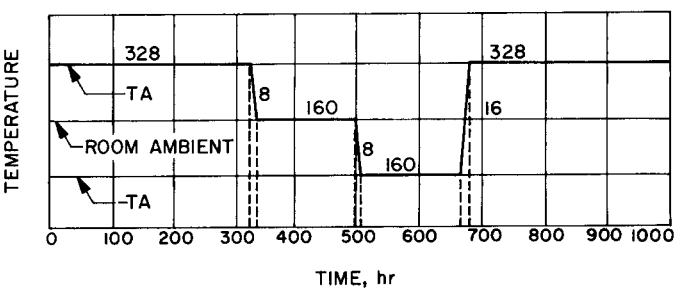

Fig. 20. Temperature profile followed during accelerated power system life test program

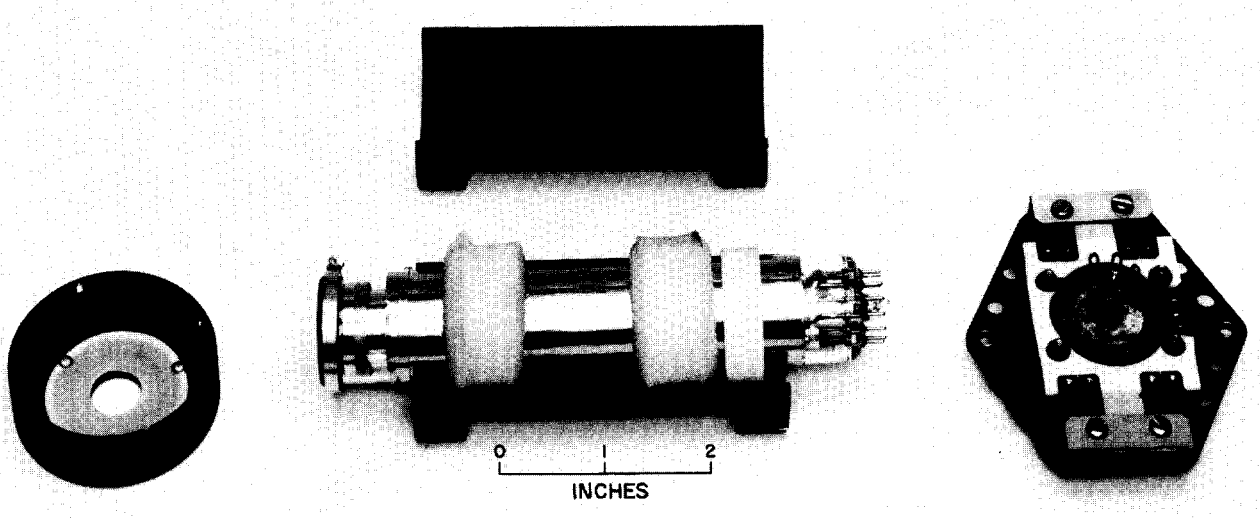

Fig. 19. TV-tube soft mount

Life testing of two TA batteries was started on February 11. One battery was maintained at 100°F and one at 50°F. At the beginning of the battery life test program no vacuum chambers were available and all tests were at atmospheric pressure. On March 24, the battery at 100°F had a cell failure which was later traced to a broken plate lead—a manufacturing error. As a result of the failure, the flight acceptance (FA) test specification was changed to include a high discharge current test. Another TA battery was placed in test at 100°F to replace the failed unit. Three vacuum chambers became available on August 20, and the two TA batteries were placed under vacuum. In addition, a third TA battery that was to follow the expected flight temperature profile was placed in the remaining chamber. All tests are continuing without problem.

2. *Life Test of Narrow Angle Mars Gate*

The Narrow Angle Mars Gate (NAMG) is located on the planetary scan platform of the *Mariner C* spacecraft. It provides an acquisition signal to the Data Acquisition System when Mars enters its field of view. This signal causes initiation of the science planetary encounter sequence.

On May 12, 1964 an accelerated life test was begun to determine the long-term operating behavior of the *Mariner C* NAMG. After an initial increase in light sensitivity, the unit has operated some 2000 hr in a stable and consistent manner. The present acquisition and dropout levels are within the normal limits of operation, and the unit would perform all functions required by the *Mariner C* mission.

a. Test conditions. The life test is being run at a temperature of 167°F. All previous testing has indicated that high temperature would be the worst condition. Since the expected cruise temperature range is 10 to 40°F with a possible maximum of 140°F during midcourse, this 167°F test temperature should provide a considerable acceleration factor to any degradation. The unit under test has completed all the type-approval qualification tests satisfactorily.

The unit has normal power, 20 vdc and 20 mw, applied at all times. At intervals of 100 to 200 hr, the planet encounter is simulated and the sensitivity of the unit is measured.

b. Test results. The test unit had a previous history of about 350 hr of 167°F operation during the type-approval tests. During this time, the sensitivity increased from 0.0054 ft-c trigger and 0.0026 ft-c dropout to 0.0020 ft-c trigger and 0.0012 ft-c dropout.

During the first 200 hr of the life test, a further increase in sensitivity to 0.0015 ft-c trigger and 0.0010 ft-c dropout was observed. The test unit then stabilized at this sensitivity and has remained there to date (>2000 hr).

At no time has the unit failed to give the correct acquisition signal. It should also be noted that even with the greatly increased sensitivity, there is still a margin of at least 100:1 between the present trigger level and the dark level. There are no objects other than Mars or the two moons of Mars which would exceed the dark level.

In addition, some tests have been performed on photoconductive cells at elevated temperatures as previous experiences have indicated these cells might be a problem area in the NAMG.

c. Cell tests. High-temperature tests of the Clairex CL-705L photoconductive cell (used on the NAMG), as well as other cells, have been conducted to investigate the sensitivity changes noted. Some typical results are plotted in Fig. 21 along with the performance of the life test unit. The large anomaly in the NAMG curve was caused by exposing the unit to a light source of sufficient intensity to trigger it for about 24 hr. All cells to some extent exhibit this light fatigue effect. The cells retain the increased sensitivity when cooled, and it would appear that a high temperature burn-in of the cells before use would reduce the drift noted. The dark resistance in all cases remained above 100 MΩ which for the NAMG is equivalent to 0.00001 ft-c.

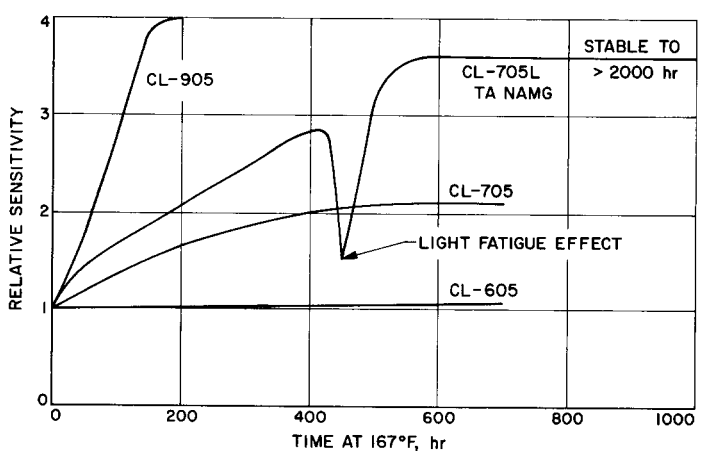

Fig. 21. Light sensitivity versus time at high temperatures for CdS photoconductive cells

The CL-605 cell is in a glass envelope and is not affected by high temperature. There appears to be a definite correlation between the metal housings and the increased sensitivity noted on the other cells, though the mechanism is not presently understood.

3. Magnetic Shielding for Canopus Tracker

a. Test procedure. Several test shields were constructed from Conetic AA, 0.014 in. thick (Perlmuth Electron Association), the same material now used in the Canopus tracker shield tubes. Some tubes had different lengths, others had slightly different radii so that they could be nested together.

Magnetic shielding tests were made in order to determine the (1) effect of cylinder length, (2) effect of additional thicknesses of shielding material, (3) effectiveness of the annealing process presently used, (4) effect of the gold plating and polishing process, and (5) end effects. These tests were conducted in the shield room at the laboratory. A uniform transverse field B of 0.1 gauss (10,000 γ) was used for all tests. The attenuation (B_{out}/B_{in}) of the transverse field was used as the measure of the shielding effectiveness.

b. Test results. The attenuation factor increased approximately linearly with additional thicknesses of shielding material. A graph of the attenuation as a function of shield thicknesses for annealed shields appears in Fig. 22.

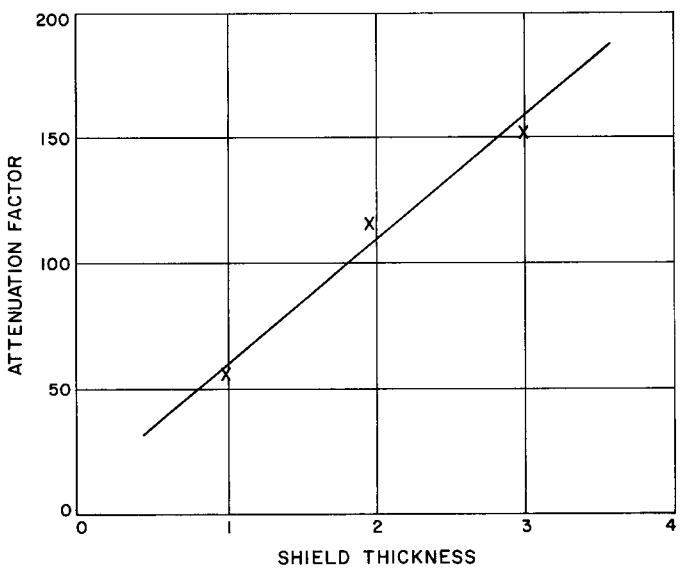

Fig. 22. Attenuation of a magnetic field as a function of the number of concentric cylinders in the shield

The annealing process improved the attenuation by a factor of about 9 in each case. The gold plating and polishing process reduced the attenuation factor by about 15 to 20%.

Axial plots of the transverse field were made for several shields. In each case, the field was reduced only 50 to 75% at the mouth of the cylinder, and the field began to level off to its minimum value about 1 in. inside (1.14 radii). The graph for two concentric annealed shields is shown in Fig. 23.

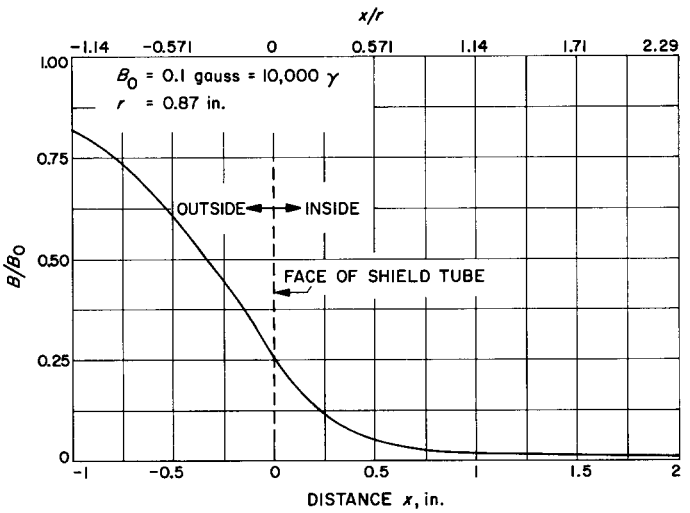

Fig. 23. Transverse magnetic field along the tube axis as a function of the distance from the mouth of two concentric cylindrical annealed shields

c. Sensitivity of image dissector to internal field. The null shift of the image dissector (Fig. 24) to an internal uniform magnetic field is about 7.8 deg/gauss, corresponding to an electron image shift of approximately $7.8 \times 0.014 = 0.109$ in./gauss (extrapolated to the photocathode). The method of deriving this value is described later. In Fig. 24, at a time $t = 0$, the electron leaves the cathode with zero velocity; at $t = t_1$, the electron has been accelerated through the voltage V and reaches X_1; at $t = t_2$, the electron enters the aperture at X_2 to the photomultiplier tube; Y_1 is the vertical displacement in Region 1; Y_2 is the vertical displacement in Region 2; and $Y_{total} = Y_1 + Y_2$. For a maximum allowable error of 0.05 deg, the attenuated field must be about 6.4×10^{-3} gauss. Assuming a maximum external field of 0.675 gauss (150% of Earth's field), an attenuation factor of 105 would then be necessary. This means that two annealed concentric cylinders of the conetic material presently used should be employed and the shield should extend out about 1¼ in. in front of the photocathode.

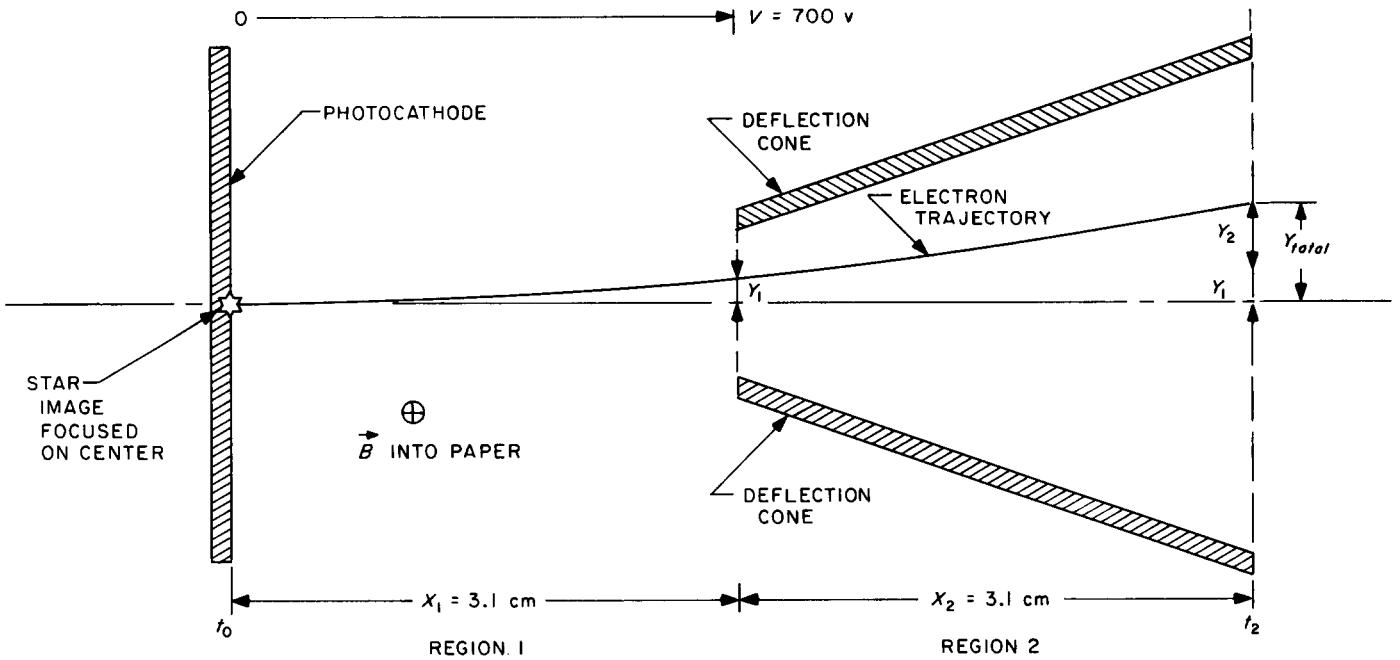

Fig. 24. Effect of internal field on an electron trajectory in the image dissector

d. Computation. Assume a uniform B field (Fig. 24) pointing into the paper, a the acceleration, v the velocity, E the electric field, q the electron charge, m the electron mass, and F the force.

Find Y_1:

$$Y_1 = \int_0^{t_1} v_{Y1}\, dt$$

$$\vec{F} = q\vec{v} \times \vec{B} + q\vec{E} \Rightarrow a_{X1} = \frac{q}{m} E_X, \quad a_{Y1} = \frac{q}{m} v_{X1} B$$

$$v_{X1} = \int_0^t a_{X1}\, dt = \frac{q}{m} E_X t$$

$$\Rightarrow v_{Y1} = \int_0^t \left(\frac{q}{m}\right)^2 E_X B t\, dt = \left(\frac{q}{m}\right)^2 E_X B \frac{t^2}{2}$$

$$\therefore Y_1 = \int_0^{t_1} \left(\frac{q}{m}\right)^2 E_X B \frac{t^2}{2}\, dt = \frac{1}{6}\left(\frac{q}{m}\right)^2 E_X B t_1^3$$

Find t_1:

$$X_1 = \frac{1}{2} a_{X1} t_1^2 \qquad \Rightarrow t_1^2 = \frac{2X_1}{a_{X1}} = \frac{2X_1}{\frac{q}{m} E_X}$$

(For $V = 700$ v, $t_1 \approx 4.8 \times 10^{-9}$ sec). Inserting the expression for t_1 into the expression of Y_1:

$$Y_1 = \frac{1}{6}\left(\frac{q}{m}\right)^2 E_X B\, 2^{3/2} X_1^{3/2} \left(\frac{q}{m}\right)^{-3/2} E_X^{-3/2}$$

$$\Rightarrow Y_1 = \left(\frac{qX_1}{2mE_X}\right)^{1/2} B \frac{2X_1}{3}$$

Now find Y_2: (There is no more X acceleration.)

$$Y_2 = \int_{t_1}^{t_2} v_{Y2}\, dt$$

where

$$v_{Y2} = \int_0^t a_Y\, dt = \int_0^{t_1} a_{Y1}\, dt + \int_{t_1}^t a_{Y2}\, dt$$

$$\int_0^{t_1} a_{Y1}\, dt = v_{Y1}\Big|_{t=t_1};$$

$$\int_{t_1}^t a_{Y2}\, dt = \int_{t_1}^t \frac{q}{m} v_{X2} B\, dt = \frac{q}{m} v_{X2} B (t - t_1)$$

$$Y_2 = \int_{t_1}^{t_2} \left[v_{Y1}\Big|_{t=t_1} + \frac{q}{m} v_{X2} B (t - t_1) \right] dt$$

$$\therefore Y_2 = v_{Y1}\Big|_{t=t_1} (t_2 - t_1) + \frac{1}{2}\left(\frac{q}{m}\right) v_{X2} B (t_2 - t_1)^2$$

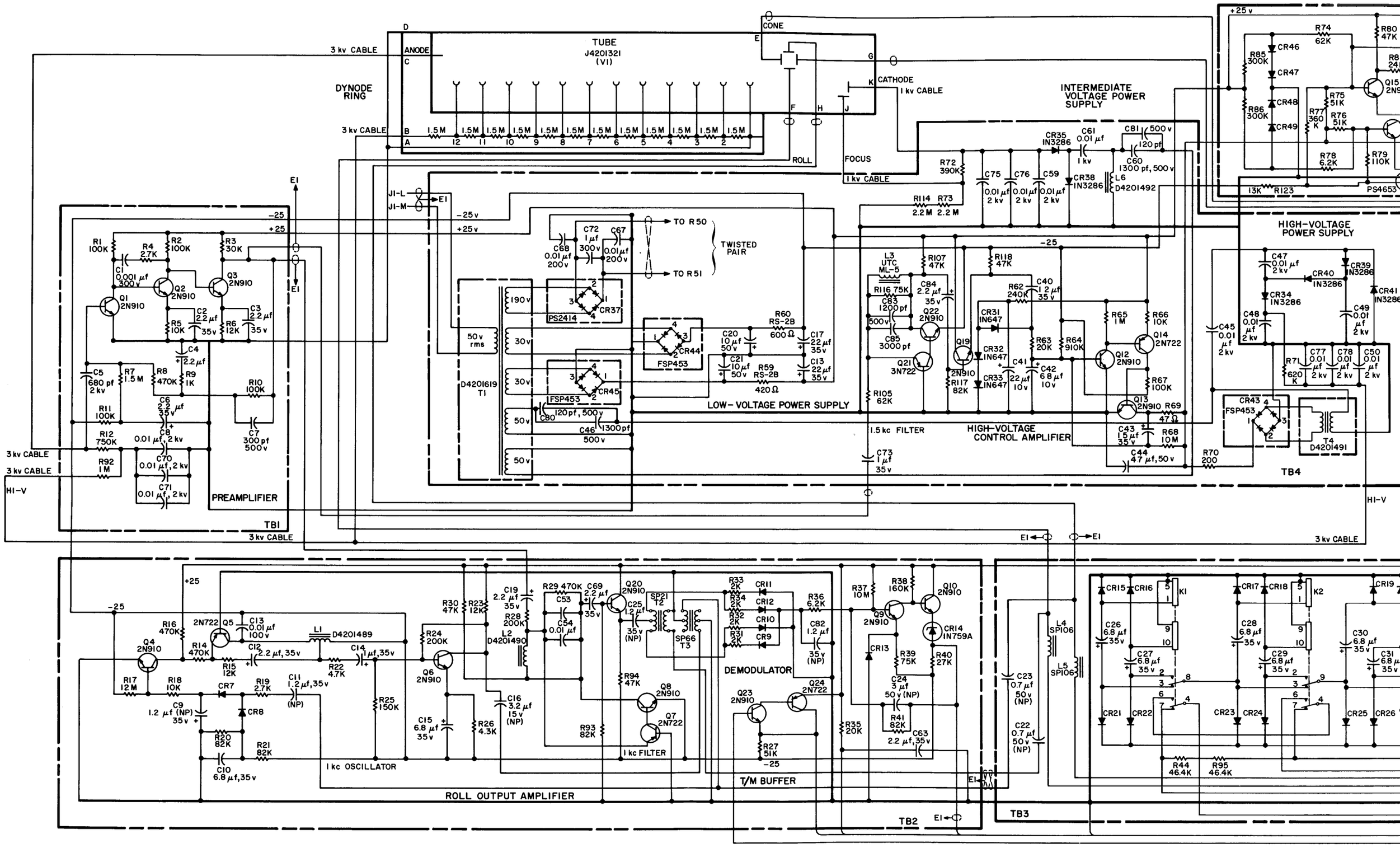
TUBE
J4201321
(V1)
DYNODE RING
CONE
ANODE
CATHODE
3 kv CABLE
1 kv CABLE
ROLL
FOCUS
INTERMEDIATE VOLTAGE POWER SUPPLY
HIGH-VOLTAGE POWER SUPPLY
LOW-VOLTAGE POWER SUPPLY
HIGH-VOLTAGE CONTROL AMPLIFIER
1.5 kc FILTER
PREAMPLIFIER
TB1
TB4
TB2
TB3
TWISTED PAIR
TO R50
TO R51
D4201619 T1
D4201489
D4201490
D4201491
D4201492
PS2414
PS4653
FSP453
DEMODULATOR
T/M BUFFER
1 kc OSCILLATOR
1 kc FILTER
ROLL OUTPUT AMPLIFIER
HI-V
+25 v
-25 v
-25
+25
EI

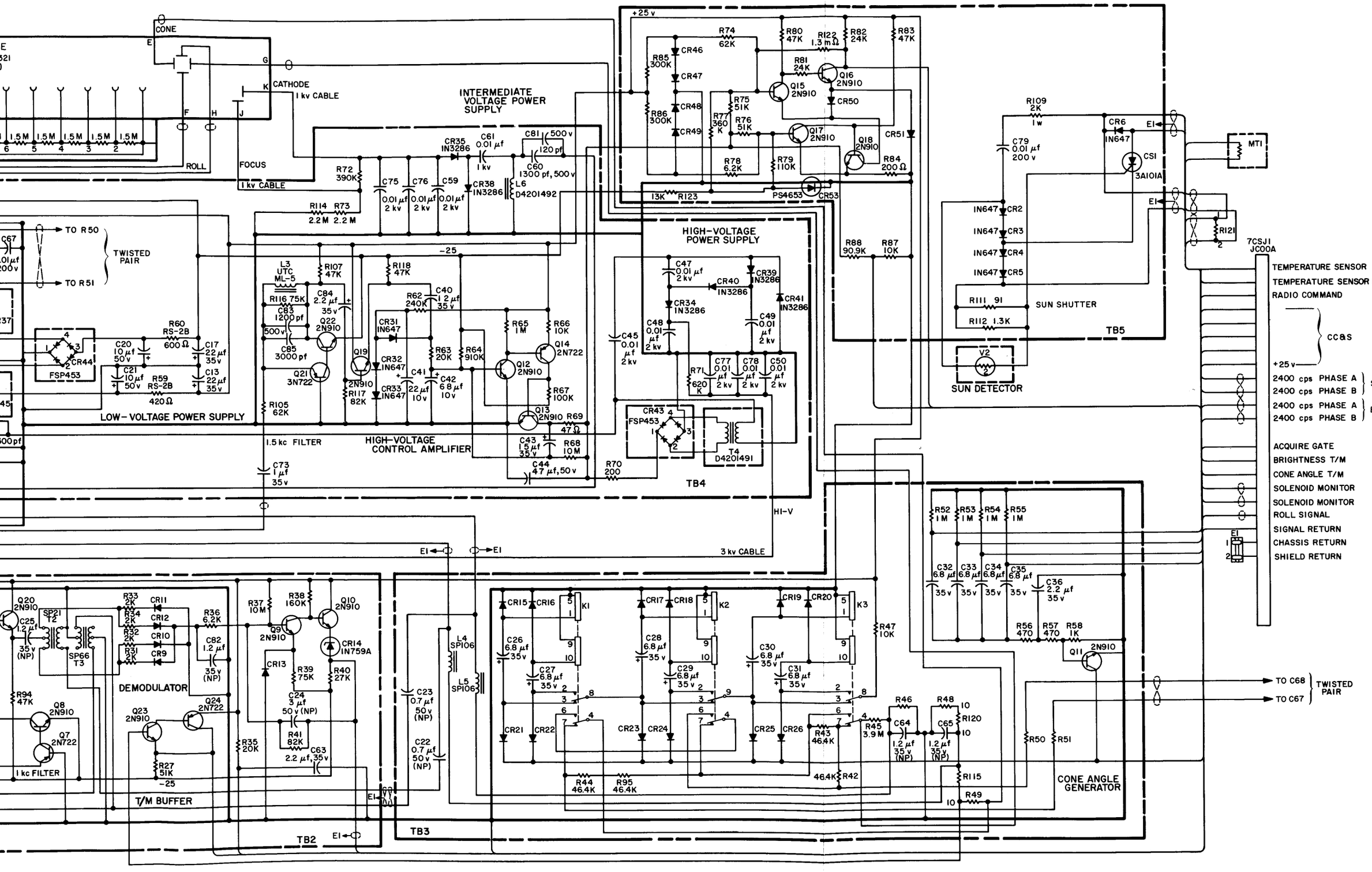

Fig. 25. Canopus tracker schematic diagram

V_{Y1} has already been given as a function of time, all we have to do is insert t_1:

$$\Rightarrow v_{Y1}\Big|_{t=t_1} = \frac{1}{2}\left(\frac{q}{m}\right)^2 E_X B t_1^2 = \frac{\frac{1}{2}\left(\frac{q}{m}\right)^2 E_X B\, 2X_1}{\frac{q}{m} E_X}$$

$$v_{Y1}\Big|_{t=t_1} = \left(\frac{q}{m}\right) B_{X1}$$

$t_2 - t_1$ is given simply by

$$\frac{X_2}{v_{X2}} = \frac{X_2}{a_{X1}\, t_1}$$

$$\Rightarrow t_2 - t_1 = \frac{X_2\left(\frac{q}{m} E_X\right)^{1/2}}{\frac{q}{m} E_X (2X_1)^{1/2}} = \frac{X_2}{\left(2\frac{q}{m} E_X X_1\right)^{1/2}}$$

(For $V = 700$ v, $t_2 - t_1 \approx 2.4 \times 10^{-9}$ sec.) The expression for Y_2 then becomes:

$$Y_2 = \left(\frac{q}{m}\right) B_{X1} \frac{X_2}{\left(2\frac{q}{m} E_X X_1\right)^{1/2}} + \frac{1}{2}\left(\frac{q}{m}\right) \frac{B X_2^2}{\left(2\frac{q}{m} E_X X_1\right)^{1/2}}$$

$$\Rightarrow Y_2 = \left(\frac{q X_1}{2mE_X}\right)^{1/2} B\left(X_2 + \frac{X_2^2}{2X_1}\right)$$

Now adding the expressions for Y_1 and Y_2:

$$Y_{total} = \left(\frac{q X_1}{2mE_X}\right)^{1/2} B\left(X_2 + \frac{X_2^2}{2X_1} + \frac{2X_1}{3}\right)$$

Since $X_1 = X_2 = X$, and $E_X = V/X$ this reduces to

$$Y_{total} = \left(\frac{q}{2mV}\right)^{1/2} \frac{13BX^2}{6}$$

The sensitivity S in meters/gauss is given by

$$S = \frac{Y_{total}}{B} \times 10^{-4} = \left(\frac{q}{2mV}\right)^{1/2} \frac{13X^2}{6} \times 10^{-4}$$

$$\therefore S = 2.3 \times 10^{-3}\ \text{m/gauss}$$

where $Q = 1.6 \times 10^{-19}$ coulomb, $m = 0.91 \times 10^{-30}$ kg, $V = 7 \times 10^2$ volts, $X = 3.1 \times 10^{-2}$ meters. However, there is a magnification factor in the electron optics of 0.84, so that 2.3×10^{-3} m/gauss at the plane of the photo multiplier tube aperture corresponds to $(2.3 \times 10^{-3})/0.84$ m/gauss at the cathode $= 2.7 \times 10^{-3}$ m/gauss. The apparent null shift in degrees/gauss, S = (2.7×10^{-3} m/gauss) × (10^2 cm/m) × (1 in./2.54 cm) × (1 deg/14 × 10^{-3} in.) = 7.8 deg/gauss.

4. Canopus Tracker

a. Introduction. The Canopus tracker development program is now in its final stages. The design is frozen and has been environmentally qualified. The design is for the most part unchanged from that recorded in Ref. 4. However, considerable effort has been expended in the development of an environmentally qualified design. This report includes a review of the final design and performance parameters and an outline of the areas in which development effort was concentrated. The final circuit diagram is presented in Fig. 25, and photographs of a finished flight unit are depicted in Fig. 26. In the view with covers removed, the packaging techniques and the accessibility and inspectability of the finished unit are clearly evident.

b. Final performance parameters. The general characteristics of the Canopus tracker are listed in Table 2. The structural fraction of the weight is 38.4%, which includes the chassis and the dust covers and all aluminum parts. Low weight has been achieved for a chassis resonance of 350 cycle/sec. Low power consumption can be attributed to (1) the use of an all-electrostatic image dissector and (2) the use of high-efficiency, series-resonant, intermediate and high voltage power supplies.

Table 3 outlines the performance of the roll error channel. The roll error signal can be expected to perform within the quoted specifications over the temperature extremes of 0 to 100°F, supply voltage variations of ±3%, and power supply frequency variations of ±1%. Degraded performance from the roll error channel can be expected over the temperature extremes of −50 to +150°F, supply

Table 2. Characteristics of Canopus tracker

Weight	4.95 lb
Power	1.5 v-amp
Field of view	
Instantaneous	0.9 × 11 deg
Scanned	5 × 11 deg
Total gimbaled	5 × 32 deg
Field of view positions	
Programmed by CC&S	5
Optional by radio command	1

UNCLASSIFIED

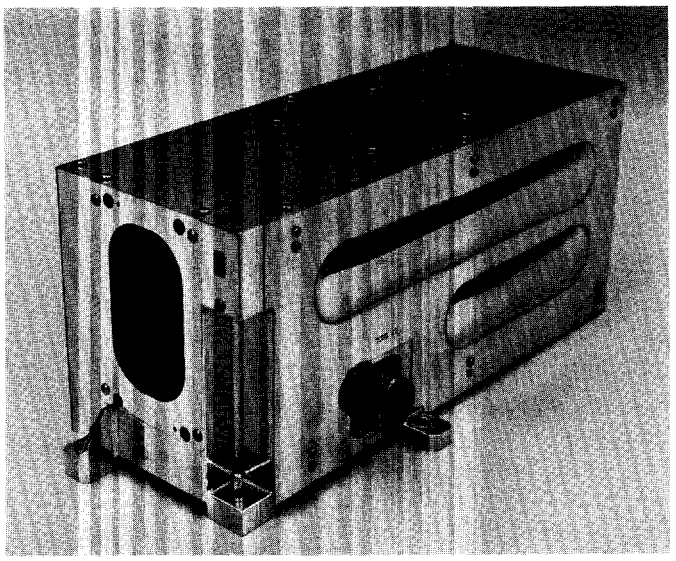

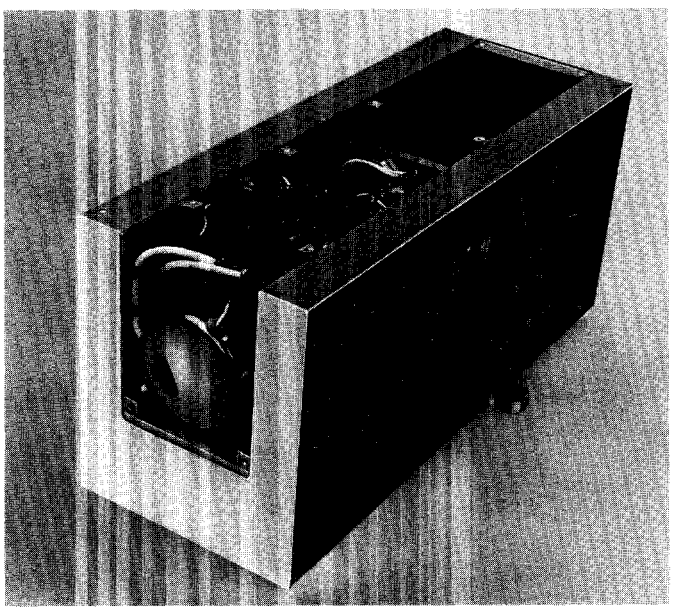

Fig. 26. Canopus tracker flight unit with and without cover

voltage variations of −10 to +40%, and supply frequency variations of −5 to +2.5%. The null stability includes the effects of supply voltage variation, supply frequency variation time, star intensity, and cone angle. The largest single source of null instability is the star cone angle update. Null instability with cone angle can be attributed to (1) deflection nonlinearity in the image dissector, (2) mechanical alignment of the tube to the mounting feet of the tracker, and (3) the network which compensates for misalignment between the deflection plates and the aperture of the tube.

Table 3. Roll error signal characteristics

Scale factor	8 v/deg
Stability	±20%
Typical roll error noise	
1 × Canopus star	0.015 deg P-P
0.25 × Canopus star	0.025 deg P-P
Time constant	0.5 sec
Null stability	±0.125 deg

Table 4. Acquisition gate parameters

High gate intensity	8 × Canopus ±20%
Low gate pull-in	0.5 × Canopus ±10%
Low gate drop-out	0.33 × Canopus ±10%

The acquisition gate parameters are given in Table 4. The voltage level for setting the low gate is based on an intensity calibration of the tracker at the cone angle of minimum over-all sensitivity. This procedure gives each tracker the greatest margin to background noise. The high intensity gate has been moved from 4 times Canopus to 8 times Canopus because there are no acquirable objects in this intensity band. The gates are stable to 25% with normal variations of supply voltage, power supply frequency, and temperature.

The tracker generates an analog dc voltage which is proportional to the intensity of the star in the field of view. This signal drives the acquisition gate and is telemetered back to Earth for use in identifying the star which has been acquired. Although the intensity signal is not the primary function of the tracker, it has been the most difficult to produce satisfactorily. Some of the important characteristics of the intensity signal are tabulated in

Table 5. Intensity voltage output

Dynamic range	3 to 4 decades
Faintest detectable star (no background)	0.02 to 0.04 × Canopus
Signal: Peak noise (no background)	
Star intensity = 1 × Canopus	16:1
Star intensity = 0.25 × Canopus	8:1
Background rejection	
Apparent intensity on 2 × 10^{-5} ft-lamberts (background around Canopus)	0.08 to 0.16 × Canopus
Apparent intensity on 1 × 10^{-4} ft-lamberts (approx. peak Milky Way)	0.2 to 0.4 × Canopus
Stray light rejection	
Illumination from 35 deg off axis to reach 0.25 × Canopus	5 to 10 ft-c of sunlight
Illumination from 35 deg off axis to reach 0.04 × Canopus	0.2 to 0.5 ft-c of sunlight

UNCLASSIFIED

Table 5. Large dynamic range of the telemetered intensity is obtained by utilizing the magnitude of the high voltage on the electron multiplier as the intensity signal. This voltage is a function of star intensity since the star signal is servo-controlled to a constant output by adjusting the voltage on the electron multiplier. The faintest detectable star has been limited to 0.02 times Canopus by adjusting the maximum voltage capability of the high voltage power supply. The high voltage has been limited to minimize the stress on the components. Since the signal-to-peak noise on the intensity voltage is proportional to the square root of star intensity (Table 5), we know that the noise on the intensity signal is caused by shot noise in the signal at the photocathode. Shot noise due to dark current, thermal noise, and circuit noise are negligible.

Fig. 27 is a typical sample of the output of the three-tracker function versus roll angle for three different intensities. Fig. 28 is a typical calibration of the intensity

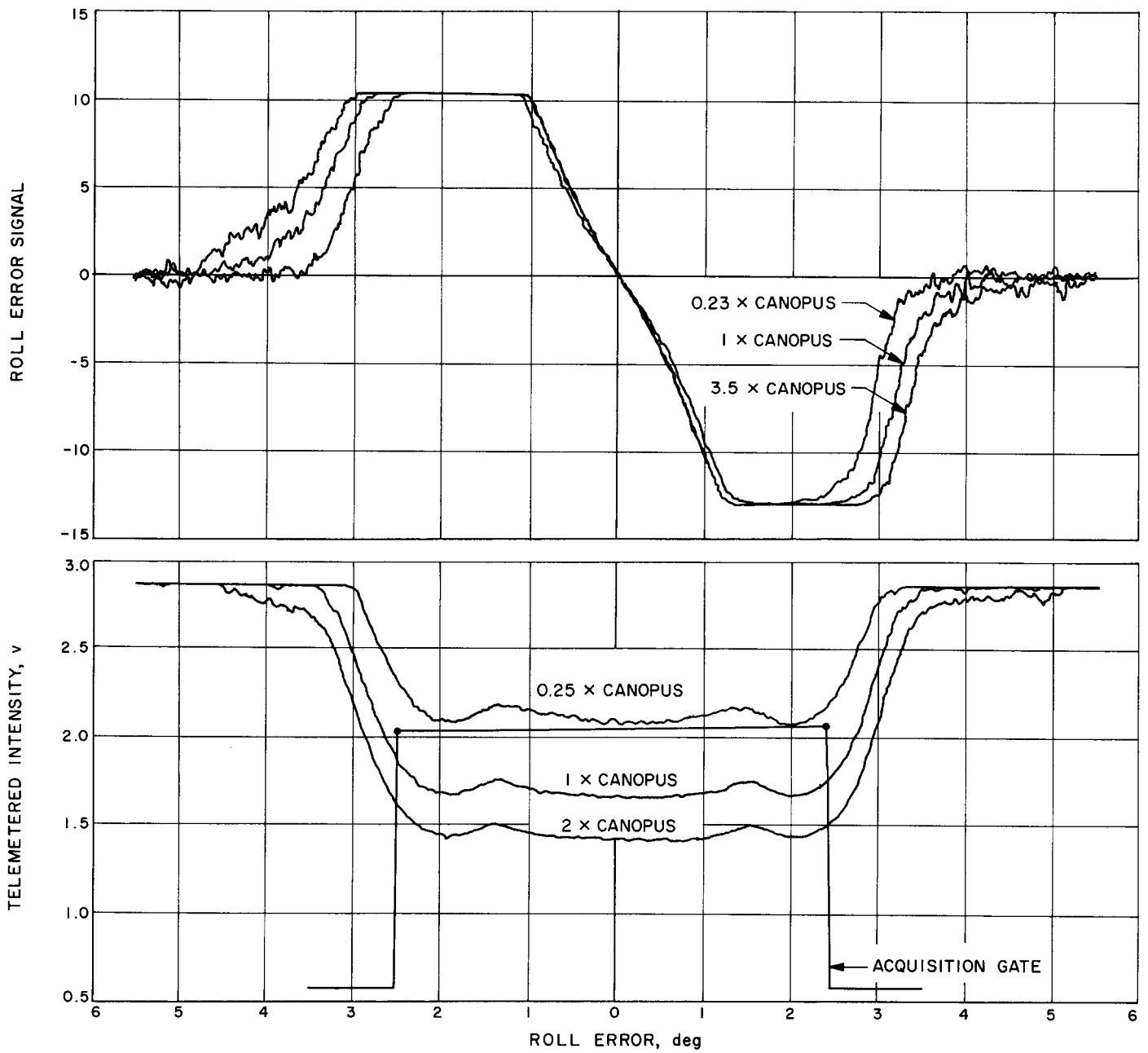

Fig. 27. Telemetered roll error signal of three-tracker function versus roll angle

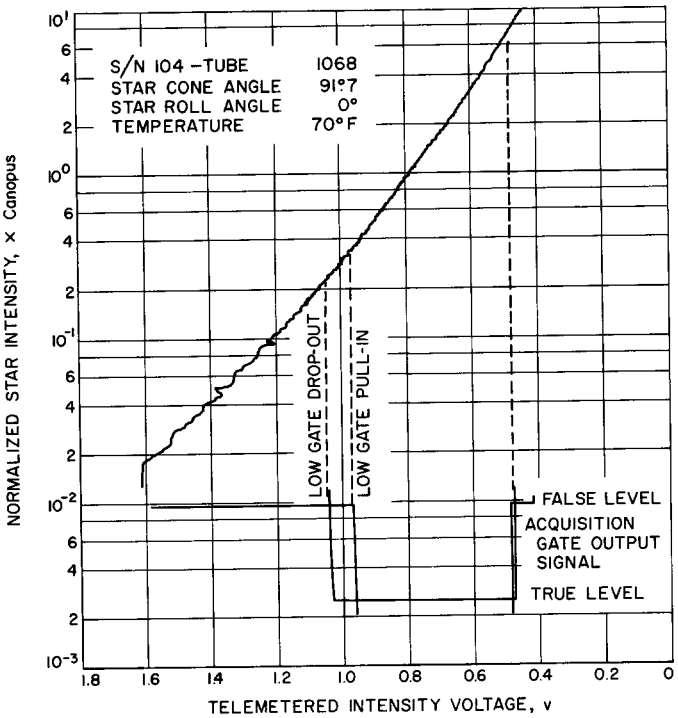

Fig. 28. Telemetered calibration curve of intensity channel

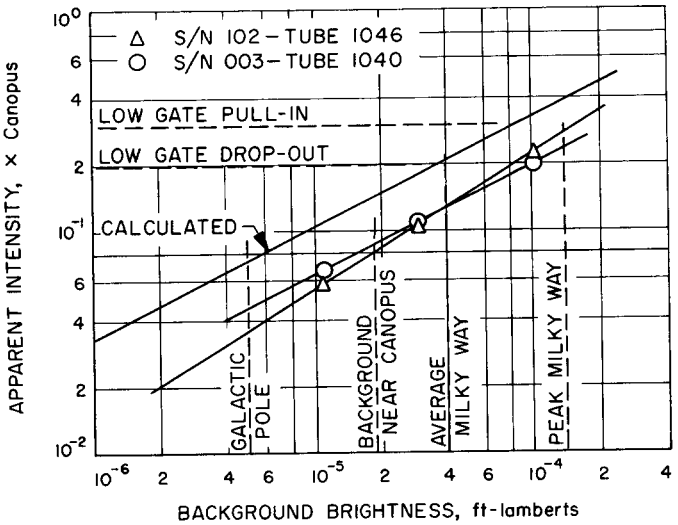

Fig. 29. Response of two flight trackers compared with estimated response to shot noise

channel showing the pull-in and drop-out levels of the gates.

The ability of the Canopus tracker to reject the stellar background is limited by (1) the uniformity of the over-all sensitivity within the scanned field of view, and (2) the shot noise inherent in the photocurrent caused by the background. The degree to which a particular unit is limited by shot noise or uniformity can be determined by inspection of a graph of apparent intensity versus background brightness. If the apparent intensity increases as the square root of the background, shot noise is controlling the response of the tracker. If the apparent intensity increases linearly with the background, nonuniformity of sensitivity is controlling the response of the tracker. Fig. 29 compares the response of two of the flight trackers with an estimate of the response of the tracker to a flat background assuming the sensitivity is perfectly uniform and that the response is caused by shot noise. The reason that the flight trackers appear to be less sensitive to flat backgrounds than to the calculated theoretical limit is because of uncertainties in the assumption upon which the estimate was made. The largest uncertainty being response of the intensity channel to noise. It is significant to notice that S/N 003 is free from nonuniformities in sensitivity since the apparent intensity goes as the square root of the background brightness. This demonstrates that the optical system is free from vignetting within the scanned field of view.

Superimposed on the flat background calibration (Fig. 29) is the brightness of the background of several areas of the sky. Also shown on the plot are the minimum pull-in and drop-out intensities of the flight trackers. Since the absolute brightness of the sky plotted on Fig. 29 is uncertain by a factor of two, the margin between the low gate and the background makes the probability of automatic Canopus acquisition substantially less than one. A fix which would have lowered the apparent intensity of a given background by a factor of 8 was taken through the breadboard stages but was not incorporated because of the time schedule and also the results of an investigation into the ability to handle the situation with the present mechanization of the attitude-control system. The attitude-control system required both an intensity gate signal and a properly phased error signal of -4 v to recognize a celestial object as acquirable (see Ref. 4 for requirements of this mechanization).

Tests have been made on a model of the Milky Way which simulates the brightness and brightness gradients of the Milky Way near Canopus. The model was constructed from data presented in Ref. 5. The data used has a resolution of 2.5×2.5 deg and includes all stars of 7.0 visual magnitude and dimmer. Fig. 30 is a photograph of the brightness model which was constructed using paints with calibrated reflectance. Since the triangular pattern cannot be resolved by the tracker, they appear as a smooth gradient of brightness.

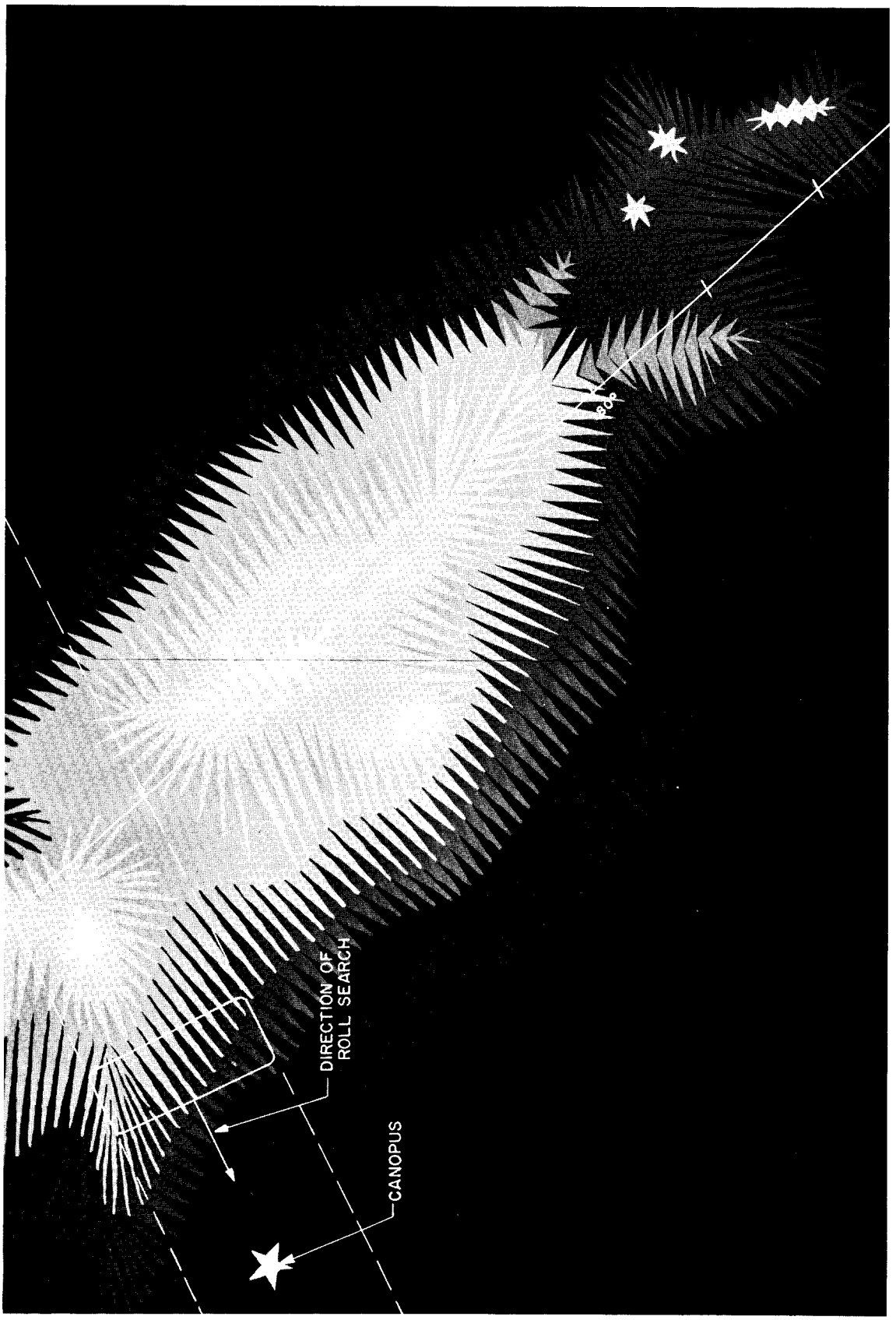

Fig. 30. Brightness model of the Milky Way near Canopus

The results of scans through the model Milky Way have shown that the largest roll error signal is less than 4 v so that there is little chance of acquiring the Milky Way and going into a broader than normal limit cycle. However, it is possible to have a faint star plus a Milky Way background and to be within the gate and give the proper error signal for acquisition. If this occurs, a roll override radio command may be sent from the Earth to continue search. Models are currently under construction which will simulate both the Milky Way gradients and the discrete stars which are found on that background. Through these models, we hope to learn how the tracker will respond during the roll search.

c. Environmental test history. The history of mechanical environmental tests is presented in Table 6. A review of this summary reveals the biggest problem—environmental qualification of the CBS image dissector tube. The shake record of the (evaluation engineering model) EEM tracker testifies to the general ruggedness of the design. It is significant that the thick wire tubes and the improved tubes failed at roughly the same input level. The tests on June 3 and June 6, 1964 are considered to have qualified both the improved tube and the thick wire tube. However, further testing of both tubes to increased levels on June 13 resulted in failures. These test results imply that the type-approval (TA) test is close to the fatigue limit of the nonruggedized tube.

The EEM has performed satisfactorily through the TA vacuum temperature test with the temperature extremes modified to 0 and 100°F. The tracker has been analyzed to insure that it is adequately vented. S/N 002 has been instrumented with vacuum gages, and adequate venting of the most remote cavity has been demonstrated. S/N 002 operated in vacuum from March 6 to June 13 when the temperature controller on the test chamber failed, and the vacuum was accidentally turned off without turning off the tracker. High-voltage arcing occurred when the pressure came up above 50 μ. Arcing must have been sustained for several hours because the damage was extensive. A total of 2300 hr of vacuum operation were logged and continuously monitored. No unexplained anomalies in the primary functions of the tracker were observed. However, the intensity signal for no-star input increased by a factor of 26 during the first 3 weeks of operation. To eliminate the possibility of a vacuum associated problem, the pressure was increased to atmospheric

Table 6. Vibration and shock test history of Canopus trackers

Date	Test	Tracker	Tube number	Type	Result	Failure mode
6/26/63	3 g's sine 2 planes 30 cps to 2kc 24 min total	EEM	1095	Regular	Passed chassis resonance $>$ 400 cps and Q $<$ 4	—
11/13/63	FA to JPL 30251	EEM	1095	Regular	Failed during 3rd plane (z-axis)	—
12/16/63	FA to JPL 30251	101	2678	Regular	Passed	—
12/27/63	TA low frequency JPL 30250	EEM	2493	Regular	Passed	—
12/28/63	TA complex wave JPL 30250	EEM	2493	Regular	Failed during 1 plane of shake z-axis	Dynode 12 open at butt weld
1/16/64	TA complex wave JPL 30250	EEM	2493	Regular with D11 as anode	Failed during 3 planes of shake	Open roll deflection plate—sticky relay
1/22/64	TA shock JPL 30250	EEM	Degraded 2493	Regular	Performance erratic	Focus electrode had broken loose
5/16/64	Modified TA test by environmental requirement group dated 5/18	103	1013	Improved	Failed during second plane T-axis	Anode open at the stem
6/ 3/64	Vibration test on PTM spacecraft	EEM	1026	Improved	Passed	—
6/ 6/64	Modified TA test based on PTM response data	103	1038	Thick wire	Passed	—
6/13/64	Vibration test on STM spacecraft	EEM	1026	Improved	Failed	Anode open at the stem
6/13/64	1 Plane of 12 g's noise	103	1038	Thick wire	Failed	Anode and dynode 12 open at bucket weld
6/13/64	FA test modified to be consistent with TA conducted on 6/6/64	003	1022	Improved	Passed	—
6/20/64	TA test to 30251 plus 25 g's at 150 cps	103	1045	Rugged	Failed (relay)	Sticky relay (tube passed)

for a few days. No change due to pressure was noticed, so the bell jar was evacuated and the test continued. The no-star input stabilized at the high level for several weeks and slowly went back to the initial level. Day-to-day instabilities in the dark voltage (not the star voltage) of a factor of 2 were noticed throughout the test. At its maximum, the dark voltage was less than 0.1 times Canopus, which does not interfere with the prime functions of the tracker. Since electron multiplier dark current is known to be an unstable quantity, especially in fresh tubes, the observed performance was not unexpected.

The EEM has been intentionally operated in the corona region (50 to 2000 μ) to see if it could survive. It cannot. The input transistor to the preamplifier is the first component to fail. Trackers on the PTM and the long-term vacuum test both failed when they were accidentally operated at corona pressures.

The EEM has been irradiated with X-rays from an X-ray machine operated at the maximum anode potential (300 kv). The beam was hardened by passing it through a 1-in. aluminum plate. The results of the tests are summarized in Table 7. The internal ionization rates expected in the Van Allen and Starfish belts have been estimated at 2 rad/hr and 30 rad/hr, respectively. No permanent damage due to radiation is expected; however, the tracker turn-on time has been delayed to $L + 16$ hr so that initial acquisition will not be disturbed by radiation. Large solar flares have been estimated to produce internal ionization rates of 100 rad/hr, so a large solar flare could cause temporary loss of acquisition.

d. Image dissector development. CBS Laboratories has responded well to the need for higher quality tubes. There have been many problems both electrical and mechanical, but the tubes have continually improved. Problems with luminous sensitivity, gain, and deflection plate alignment to the electron aperture have been solved by CBS. The solution to the first dynode uniformity problem may be near. The minimum first dynode sensitivity is specified at 70% of the maximum sensitivity. Production yield of tubes has been low, and those tubes which have been delivered have been barely within specifications. Two tubes have recently been received with first dynode uniformity better than 94%, indicating that CBS now has better control on this parameter. To help stabilize tube parameters, tubes are burned-in at CBS with about the same photocurrent density as the Canopus image, the same anode current, and the maximum operating voltage on the last two dynodes. The gain of the intermediate stages is adjusted to meet the stated objectives.

Table 7. Effect of X-rays on Canopus tracker

Ionization rate internal to the image dissector	Test results		
	Intensity signal	Roll signal	Comments
4.5 rad/hr	0.25 × Canopus	< 1 v	Attitude control would not acquire since roll signal < 4 v
31 rad/hr	0.01 × Canopus immediately after radiation stopped	< 1 v during test	Took 15 min to return to normal after radiation stopped
72 rad/hr	1 × Canopus star in field of view	Saturation signal less than 4 v	Roll control would probably be lost
216 rad/hr for 25 min, with tracker off	0.1 × immediately after and 0.01 × Canopus 2 hr after	Normal after 16 hr	—

The early failures in the EEM indicated that it would be difficult to pass the environmental TA test with what has come to be called a "regular" tube. All failures could be attributed to lack of quality control in the assembly area, poor welding, and high stress on the dynode wires where they pass through the glass stem. A nickel-to-Kovar butt weld at this point failed consistently. Four of eight "regular" tubes for flight trackers were delivered by mid-January. At this point tube production was halted. Strict quality control was estabilshed with a full-time JPL resident inspector stationed at CBS. With consulting help from JPL, CBS developed the 42 weld schedules required to assemble a tube. Two programs were initiated at this time to obtain flightworthy tubes.

Table 8 summarizes the features of the three types of tube that evolved from these two programs. Because of the time schedule, the improved tube program was made the prime plan of attack, and the "rugged" tube program was made the back-up. The "T" tube was evolved to

Table 8. Features of image dissector tubes

Features	Regular	Improved	"T"	Rugged
Tweezer welds	X	—	—	—
Nickel-to-Kovar butt-weld at the stem	X	—	—	—
Shortened and kinked dynode leads	Some	X	X	X
Quality control	—	X	X	X
Weld schedules	—	X	X	X
Welding tabs on concentric parts	—	X	X	X
Necked Kovar stem lead	—	—	X	X
Two-part focus electrode	—	—	—	X
Snubbers on the multiplier	—	—	—	X

improve the schedule after the failure of the improved tube in a special TA test. The "T" tube proved to be no better than the improved tube. (See Table 5 for the test history.)

The "rugged" tube program involved an attack on the fundamental engineering problems, the high stress on the wires at the stem and the weldability of the assembly. Fig. 31 shows the two primary changes in the design—the snubbers that constrain the multiplier in the glass envelope, and the necked stem lead to make it more weldable while retaining the required flexibility in the external leads.

The rugged tube has proved to be worthy of the name. Having passed a full-level component-level TA test, its use will be emphasized where the schedule permits.

e. Optics development. Because of tracker susceptibility to spacecraft stray light and bright objects, like the Earth, 10 to 25 deg outside the field of view, considerable effort has been expended to minimize the intensity of stray light reaching the image plane. The aluminizing patterns on the catadioptric lens were modified by JPL, and an edging technique was developed to minimize the light reflected off the edges of the lens. The edges are first polished and then painted with Cat-a-lac black paint. Choice of Cat-a-lac paint is a compromise between vacuum stability and optical properties. Lenses have been refabricated using the highest grades of synthetic quartz and light flint glass. The flight lenses are image-plane quality, having exceptional polish and being free of bubbles and other defects. The front element has been tested for radiation susceptibility, and no degradation is expected. Since the geometric speed is $f/0.6$, centering and mounting are critical; however, no problems have been encountered. The critical operations have been done in-house with excellent results. An assembled set of optics and a baffle assembly are shown in Fig. 32.

f. Baffle development. The ability of the tracker to operate without being disturbed by stray light is strongly affected by the effectiveness of the baffles to attenuate light coming from outside the field of view. The effectiveness of a baffle is a complicated function of geometry, surface finish, reflectance, and knife edge quality. Some aspects of the geometry for internal baffling of the single stage baffle used on the Canopus tracker have been discussed in the past (Ref. 4). The baffles used in the Canopus tracker are made of aluminum and have knife edges milled on them with the greatest possible care. The stock is first polished, then carefully clamped and climb-milled with a finely honed cutter. After machining, the baffle is black-anodized. The resultant knife edge is sharp (approximately 0.0001 in. radius) fairly durable, and black. The "as anodized" surface is quite specular and its diffuse reflectance is about 0.6%. The specular finish was compared to a surface painted with 3M Black Velvet paint, both by visual inspection and by testing stray light sensitivity in a flight type tracker. The use of 3M Black Velvet paint on the baffles improved the sensitivity to stray light by a factor of 2 and is, therefore, used on all flight trackers. A typical baffle prior to painting is shown in Fig. 32.

g. High-voltage magnetics. The original high-voltage magnetics designed for the tracker utilized random-

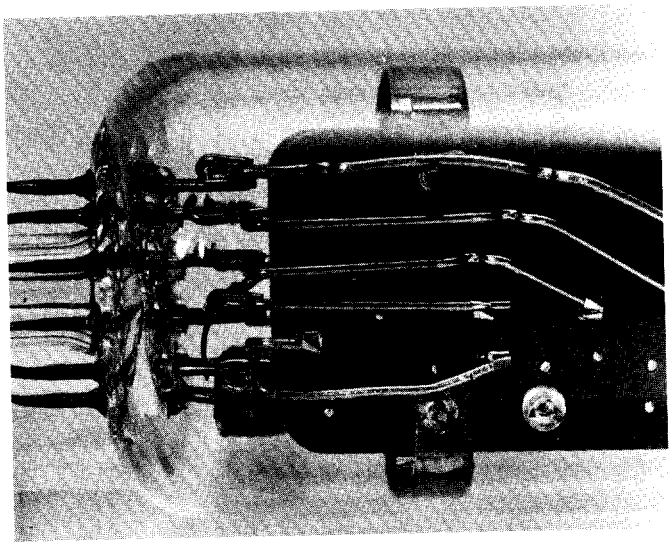

Fig. 31. Structure of rugged image dissector tube

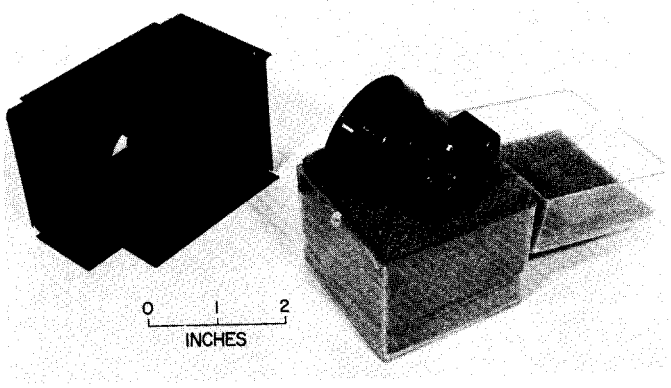

Fig. 32. Baffle and assembled optics of Canopus tracker

wound toroidal cores to obtain a compact, low-field device. During the testing program, failures occurred in a high-voltage transformer and a high-voltage inductor due to shorting of the insulation between adjacent turns. The usual cause of this condition is induced stress by high potential gradients between windings. To correct this situation, both parts were redesigned. The random-winding was replaced by a progressive bank-wind in which the highest voltage turn and the lowest voltage turn are separate, separated by a physical barrier, and the winding is controlled to assure the minimum gradient between all adjacent turns. This type of winding has a less efficient packaging factor, requiring the selection of a higher permeability core material for identical performance and over-all size. The new units were manufactured under continuous JPL quality control inspection and tested to JPL and MIL-202 screening requirements. Tracker tests confirm that the new units have identical performance characteristics, and special destructive tests indicate that the voltage breakdown level has been increased by a factor of 10.

E. Telecommunications

1. Flight Command Subsystem

The *Mariner C* flight command subsystem design is similar to that of the *Mariner R* command subsystem described in Ref. 6. A detailed account of the development of the *Mariner* command detection techniques is presented in Ref. 7. Therefore, except for brief description of the general command subsystem function, only the significant changes from the *Mariner R* design will be enumerated.

a. Command subsystem operation. The command subsystem consists of two major functional units: The command detector and the command decoder. Also included is a transformer rectifier unit which converts the spacecraft 2.4-kc voltage into the ac and dc voltages required by the subsystem.

Command detector description. A simplified block diagram of the detector is given in Fig. 33. The detector receives the composite command signal subcarrier from the radio system. The subcarrier contains the command word information (a sequence of binary digits) in the form of a biphase modulated sinusoidal signal added to a synchronization (sync) signal. The sync signal is composed of a pseudonoise (PN) sequence Modulo 2 added to a square-wave signal at a clock frequency defined as the $2f_s$ frequency. The sinusoidal signal is also at $2f_s$ frequency. A mathematical representation of the command signal is $[\pm\cos(2\pi f_s t)] + [\mathrm{PN} \oplus 2f_s.]$ The sign of the cosine wave remains constant over a bit time.

As indicated in the detector block diagram, the detector consists of two major channels where synchronization and command word detector functions are accomplished. The detector sync channel effectively correlates the incoming sync signal with a detector generated PN sequence Modulo 2 added to a square-wave signal at f_s frequency. The correlation of the two PN signals results in the error signal in the detector phase lock loop (PLL) which drives the indicated voltage controlled oscillator (VCO) (Fig. 33). To accomplish phase lock, a frequency offset is set between the transmitted and the detector $2f_s$ frequencies causing a continually changing phase shift between the two PN signals until correlation occurs. When the transmitted and the detector-generated PN sequences are in correlation, the null point of the error curve is achieved and the output of the VCO is in phase and frequency coherence with the transmitted signals. Any reasonable phase transient will now be tracked by the PLL which is in lock with the command signal. The PLL is a second-order closed loop servo with an effective closed-loop transfer function

$$H(s) = \frac{1 + \frac{2^{1/2}}{B_0} s}{1 + \frac{2^{1/2}}{B_0} s + \frac{s^2}{B_0^2}}$$

where B_0 is the loop natural frequency at the threshold input signal to noise ratio. The loop noise bandwidth $2B_{LO} = 1.06\ B_0$ is 2 cps at the threshold input signal to noise ratio.

The detector command channel filters the command word information signal from the composite command signal and recovers the command word bits by multiplying the signal with a phase reference from the detector sync channel. The multiplied signal is then applied to a matched filter (an effective integrator over the bit time) which optimally detects the transmitted bit level. The command signal is corrupted by noise assumed to be gaussian with a flat spectral density over the noise bandwidth of the matched filter. Threshold for the detector is defined at a bit error rate of 1×10^{-5}, and occurs at a composite command signal to noise ratio of 19.5 ± 1 db in a 1-cycle noise bandwidth. The reconstructed bits and

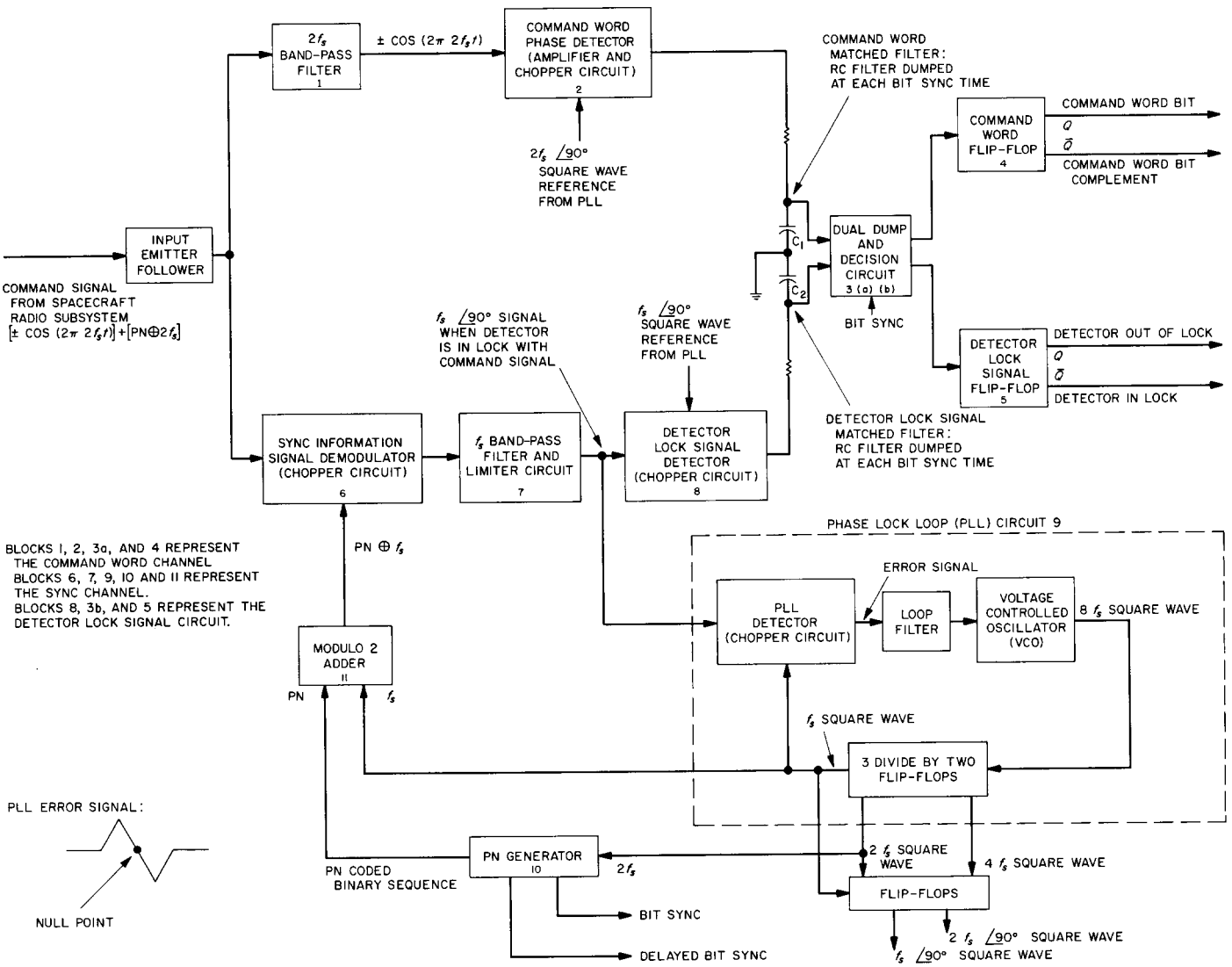
2fs BAND-PASS FILTER 1
± COS (2π 2fs t)
COMMAND WORD PHASE DETECTOR (AMPLIFIER AND CHOPPER CIRCUIT) 2
2fs /90° SQUARE WAVE REFERENCE FROM PLL
COMMAND WORD MATCHED FILTER: RC FILTER DUMPED AT EACH BIT SYNC TIME
COMMAND WORD FLIP-FLOP 4
COMMAND WORD BIT
Q
Q̄
COMMAND WORD BIT COMPLEMENT
INPUT EMITTER FOLLOWER
COMMAND SIGNAL FROM SPACECRAFT RADIO SUBSYSTEM [± COS (2π 2fs t)] + [PN⊕2fs]
C1
C2
DUAL DUMP AND DECISION CIRCUIT 3 (a) (b)
BIT SYNC
fs /90° SIGNAL WHEN DETECTOR IS IN LOCK WITH COMMAND SIGNAL
fs /90° SQUARE WAVE REFERENCE FROM PLL
DETECTOR LOCK SIGNAL FLIP-FLOP 5
DETECTOR OUT OF LOCK
DETECTOR IN LOCK
DETECTOR LOCK SIGNAL MATCHED FILTER: RC FILTER DUMPED AT EACH BIT SYNC TIME
SYNC INFORMATION SIGNAL DEMODULATOR (CHOPPER CIRCUIT) 6
fs BAND-PASS FILTER AND LIMITER CIRCUIT 7
DETECTOR LOCK SIGNAL DETECTOR (CHOPPER CIRCUIT) 8
PHASE LOCK LOOP (PLL) CIRCUIT 9
BLOCKS 1, 2, 3a, AND 4 REPRESENT THE COMMAND WORD CHANNEL
BLOCKS 6, 7, 9, 10 AND 11 REPRESENT THE SYNC CHANNEL.
BLOCKS 8, 3b, AND 5 REPRESENT THE DETECTOR LOCK SIGNAL CIRCUIT.
PN ⊕ fs
ERROR SIGNAL
PLL DETECTOR (CHOPPER CIRCUIT)
LOOP FILTER
VOLTAGE CONTROLLED OSCILLATOR (VCO)
8 fs SQUARE WAVE
MODULO 2 ADDER 11
PN
fs
fs SQUARE WAVE
3 DIVIDE BY TWO FLIP-FLOPS
PLL ERROR SIGNAL:
NULL POINT
PN GENERATOR 10
PN CODED BINARY SEQUENCE
2fs
2 fs SQUARE WAVE
4 fs SQUARE WAVE
FLIP-FLOPS
BIT SYNC
DELAYED BIT SYNC
2 fs /90° SQUARE WAVE
fs /90° SQUARE WAVE

Fig. 33. Command detector simplified block diagram

bit sync pulses (emanating from the detector PN generator each cyle of the PN sequence) are directed to the command decoder.

A lock signal is generated by the detector which effectively measures at each bit sync time the correlation between the transmitted and detector generated PN sequences, compares the correlation output to a threshold bias signal, and makes a decision as to whether or not the subsystem was in lock over the preceding bit time interval. The detector lock signal is directed to the decoder and inhibits its function when an out-of-lock indication occurs.

Command word description. The command word is comprised of 26 bits, as shown in Fig. 34. The first three bits of a command word (always 110) begin the command decoder function. Bits 4 through 9 are the command address bits. They completely identify which command word has been sent. The remaining bits constitute quantitative information bits. The *Mariner C* command subsystem has the capability of processing and executing thirty-two command words. Twenty-nine of the command words are direct command (DC) which cause a momentary switch closure in the recipient subsystem or subsystems circuitry. DC commands make use of only the decoder start and address bits of the command word. The remaining command words are quantitative commands (QC) which direct to the central computer and sequencer (CC&S) subsystem bits 9 through 26 representing either roll, pitch, or velocity information necessary for the two possible midcourse maneuvers.

MARINER C COMMAND WORD FORMAT

COMMAND BIT NO.	1	2	3	4	5	6	7	8	9	10	11	12	13	14	15	16	17	18	19	20	21	22	23	24	25	26
COMMAND BIT IDENTIFICATION	COM-MAND DECODER START			COMMAND ADDRESS						ADDRESS PARITY See Note 1		BITS 12–26 HAVE NO SIGNIFICANCE IN DC'S. IN QC'S THEY FORM PART OF THE CC&S COMMAND. REFER TO QUANTITATIVE COMMAND FORMAT														
COMMAND BIT VALUE	1	1	0	VARIABLE								ZERO FOR DC'S; VARIABLE FOR QC'S														

QUANTITATIVE COMMAND (QC) FORMAT

COMMAND BIT NO.		1	2	3	4	5	6	7	8	9	10	11	12	13	14	15	16	17	18	19	20	21	22	23	24	25	26
CC&S COMMAND BIT NO.										1	2	3	4	5	6	7	8	9	10	11	12	13	14	15	16	17	18
CC&S COMMAND BIT IDENTIFICATION										CC&S ADDRESS See Note 2			Register Selector		ODD PARITY See Note 3	TIME VALUE See Note 5											POLARITY See Note 4
QC COMMAND BIT VALUES	PITCH TURN	1	1	0	0	1	1	0	0	0	1	1	1	0		VARIABLE											
	ROLL TURN	1	1	0	0	1	1	0	0	0	0	0	0	1		VARIABLE											
	MOTOR BURN	1	1	0	0	1	1	0	0	0	1	0	1	1		VARIABLE											

1. COMMAND BIT NOS. 10 AND 11 ARE ADJUSTED TO ENSURE AGAINST SINGLE BIT ERRORS CAUSING AN INCORRECT COMMAND WORD OUTPUT.
2. COMMAND BIT NOS. 9–11 (CC&S COMMAND BIT NOS. 1–3) ARE NOT USED QUANTITATIVELY BY CC&S BUT ARE USED TO REMAIN COMPATIBLE WITH PREVIOUSLY DESIGNED HARDWARE *(MARINER R)*
3. COMMAND BIT NO. 14 (CC&S COMMAND BIT NO. 6) IS ADJUSTED IN QC'S TO GIVE AN ODD NUMBER OF *ONE* BITS IN COMMAND BIT NOS. 9–26 (CC&S BIT NOS. 1–18).
4. COMMAND BIT NO. 26 (CC&S COMMAND BIT NO. 18) MUST BE A *ONE* TO PRODUCE A CW (POSITIVE) SPACECRAFT ROTATION ABOUT THE SPECIFIED SPACECRAFT AXIS. A *ZERO* IN THIS BIT POSITION WILL RESULT IN A CCW (NEGATIVE) SPACECRAFT ROTATION ABOUT THE SPECIFIED SPACECRAFT AXIS. POLARITY BIT FOR MOTOR BURN COMMAND IS ALWAYS *ONE*.
5. COMMAND BIT NOS. 15–25 (CC&S COMMAND BIT NOS. 7–17) ARE A PSEUDO-BINARY CODE REPRESENTATION OF THE TURN OR MOTOR BURN DURATION.

Fig. 34. Command word format

Command decoder description. A simplified block diagram of the command decoder is given in Fig. 35. Upon recognition of the decoder start bits, the decoder sequences a binary counter with the detector bit sync pulses. At the correct bit sync pulse, the decoder matrix is interrogated. Depending on the address bits stored in the decoder address storage flipflops, one of the *nand* gates is gated to close an output isolation switch (or switches) in the case of a DC command. For a QC command, the interrogation permits the QC command bits to be directed to the spacecraft CC&S subsystem along with QC bit sync pulses. When no QC bits are transmitted to CC&S, alert pulses are directed, one per second, to the subsystem to clear the QC command storage registers.

If an out-of-lock indication occurs during decoder function, the decoder generates an inhibit signal which immediately stops the decoder command word processing and allows no further decoder functioning until twenty-six consecutive command zero bits are directed to the decoder after the lock signal indicates in lock once again.

b. Command telemetry. Three command signals are directed to the spacecraft telemetry subsystem to be telemetered to Earth. The signals time share the telemetry transmission channel and are sampled at a rate determined by the telemetry mode. A listing of the signals and a description of their information content follow:

(1) Detector bit sync pulses are sent to the telemetry subsystem to be conditioned into information concerning the detector VCO frequency. Between telemetry data sample times, reference pulses at the spacecraft 2.4-kc frequency are counted in the interval between two consecutive bit sync pulses. The number counted is indirectly proportional to

UNCLASSIFIED

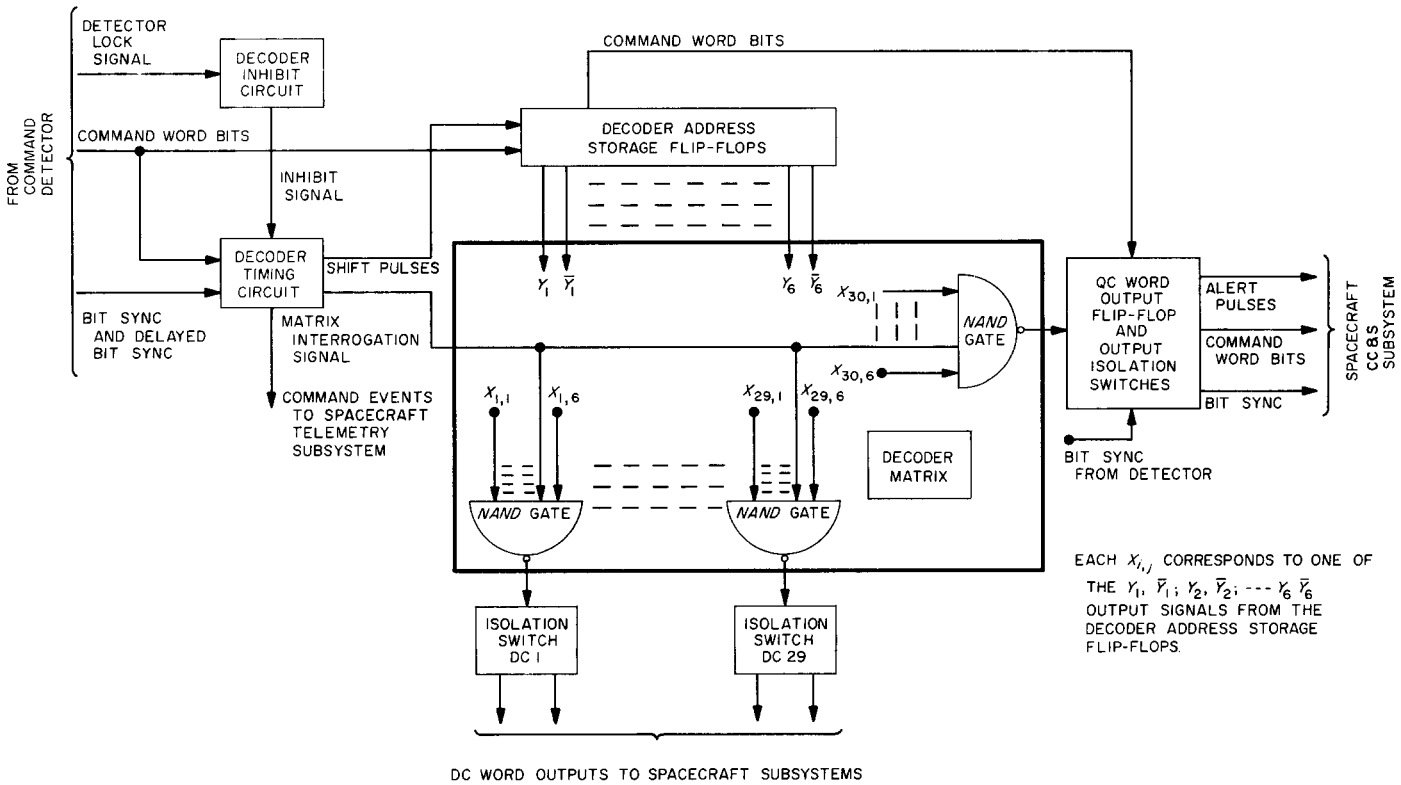

Fig. 35. Command decoder simplified block diagram

the VCO frequency. Thus, an average of the VCO frequency (over an approximate 1-sec interval) is telemetered each telemetry-data sample time. The VCO frequency data is required to determine the proper ground command signal frequency that will minimize command lock acquisition time.

(2) The detector lock signal is directed to the telemetry subsystem to be converted into one bit of information regarding the detector lock condition. If the lock signal indicates "out of lock" for at least 1 sec in the interval between telemetry sampling times, the detector lock telemetry data will be at the binary state indicating out of lock at the next sampling time. If no out-of-lock indications occur, the binary state indicating in lock will result. The detector lock data indicates when the command subsystem is capable of detecting and processing the command signal.

(3) Command event pulses are telemetered approximately 10 sec after the command decoder has recognized the decoder start bits of a command word. The event pulse indicates normal decoding timing function upon reception of the start bits. It is also normally coincident with a command address recognition and a DC command execution by the decoder. In the case of a QC command, a second event pulse will be telemetered, immediately after the last QC bit is directed to the CC&S subsystem.

Modifications to the Mariner R command design.

Command Work Format. For the *Mariner R* command subsystem a binary *one*, generated inadvertently and transmitted to the subsystem, could begin the command decoder operation. This did not necessarily generate an incorrect command execution but caused command event pulses to be telemetered which could be confusing and a nuisance. Moreover, although the *Mariner R* addresses were coded to detect single bit errors, single bit errors in the *zero* bits preceding the command word bits transmitted to the detector could conceivably cause an incorrect command output. For the *Mariner C* word subsystem, the decoder will only begin functioning with the reception of the bits 110, thus making spurious decoder operation more unlikely. The *Mariner C* command word format (Fig. 34) is also arranged so that no single bit error anywhere before, or in the command word bits, can cause an incorrect command word execution.

Command Signal. The command word information signal for *Mariner C* has been shifted 90 deg with respect

UNCLASSIFIED

to the pulse of the basic (PN) clock signal at $2f_s$ frequency. This was done to eliminate an interference of the command word information signal upon the sync signal. This interference results in a distorted PLL error curve and consequently in problems in locking up the detector.

In order to obtain a sharply defined square-wave reference signal in the detector at $2f_s\angle 90°$ to detect the command word information signal, the detector VCO frequency was changed from $4f_s$ to $8f_s$. This allows generation of the phase reference signal with ordinary command logic circuits.

Command VCO Design. Initial procurements of VCO's for the *Mariner C* program had proved unsatisfactory both in the manufacturing techniques used and in the resulting electrical performance. As a consequence, Motorola, the prime contractor for the command flight subsystem, was instructed to develop a VCO that would employ only JPL preferred components and would be packaged in a module, construction meeting with the high-quality control standards set for the other *Mariner C* command modules. As a result of an extensive three-month VCO design program, a VCO circuit was completed which incorporated a field effect transistor as the input buffer stage and a conventional multivibrator as the oscillator stage. Voltage regulation for the transistor's bias is accomplished with zener diodes. One dc supply voltage (+28 vdc) is required to operate the VCO. A schematic of the VCO with nodal voltage waveforms is given in Figs. 36 and 37.

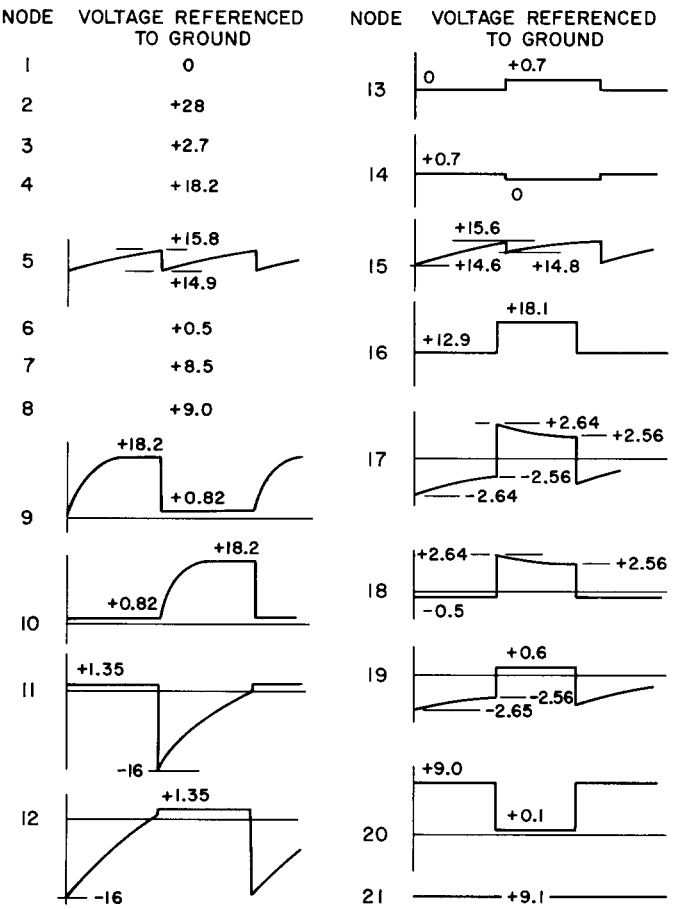

Fig. 37. Nodal voltage waveforms for command detector VCO

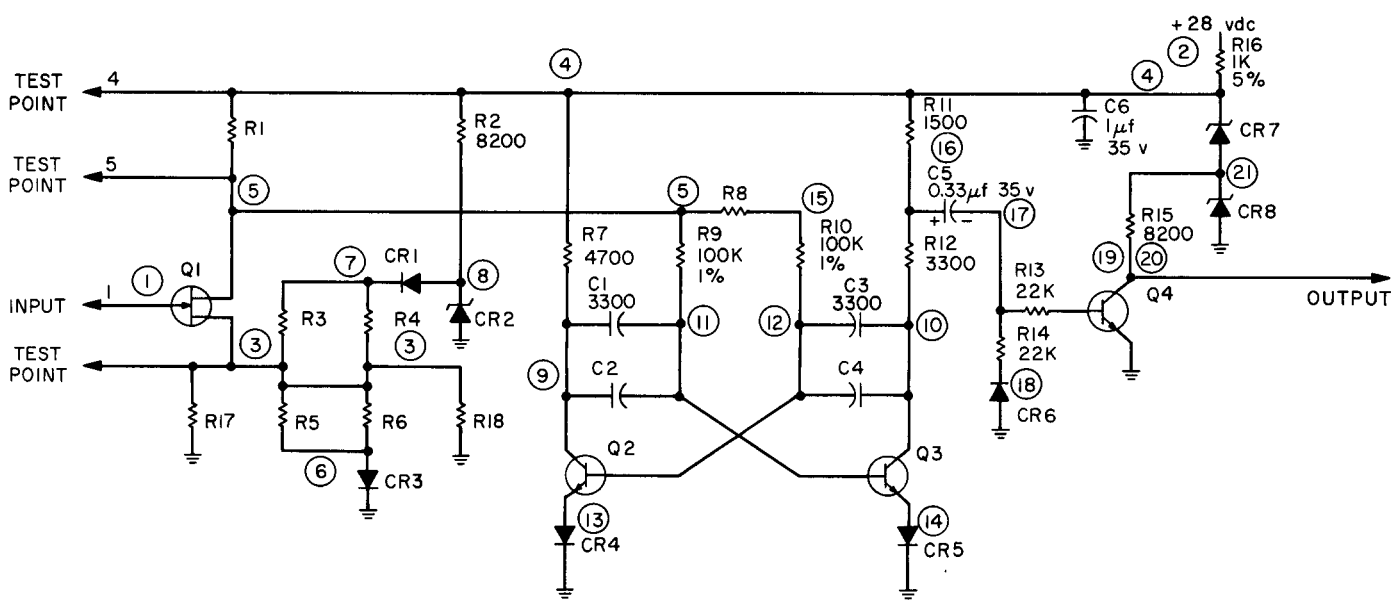

Fig. 36. Command detector VCO schematic

UNCLASSIFIED [redacted]

During the design program, one significant factor that hampered VCO frequency stability was isolated to a voltage offset drift at the input of the VCO. The voltage offset was due to input leakage current dropped across a high source impedance. To combat the situation, a field effect transistor is employed at the input which offers a very high VCO input impedance (on the order of 100 to 1000 MΩ) and consequently reduces the input drain current to a very small value. Further, there exists a bias point for the field effect transistor that allows the input drain current to be essentially independent of temperature change. The correct biasing is accomplished through selection of certain resistors during construction. The specification of frequency drift is ±0.2% over a temperature range from −10 to 75°C and with input voltage range of 28 ± 10%. The frequency stability is expected to be within 0.35% after 10,000 hr of operation. Circuit analysis and initial life test data show these specifications to be realistic for the VCO design.

Command Package Design. The *Mariner C* command packaging is basically that used in *Mariner R*. However, one "sandwich" is contained in a frame (Fig. 38) as opposed to two per frame in the *Mariner R* subsystem. The reasons for the change were to make both sides of a "sandwich" easily accessible to inspection and to reduce handling and disturbance of sections of the subsystem not affected by modification or repair being accomplished on other sections. However, the first reason was partially invalidated when a requirement was made to place a web across the frame to give greater package rigidity.

Welded Module Construction. Initially the *Mariner C* command modules were to be soldered cordwood modules as in the *Mariner R* command subsystem. However, it was determined that solder joints inside the modules could be raised to the melting point when soldering the modules to the "motherboards" during subsystem assembly. Since the joints inside the module could not be inspected for correct soldering once they have been potted, the possible degradation of the module construction during motherboard assembly was thought to be a serious problem. To alleviate this problem a complete modification of the module manufacturing technique was incorporated and the modules were redesigned for welded cordwood construction. A typical command welded module is shown in Fig. 39.

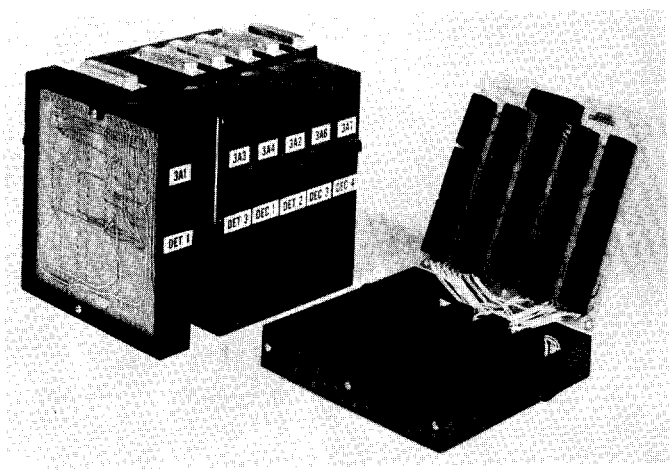

Fig. 38. Command subassembly

All welded module layouts and the required weld schedules were checked and approved by JPL before incorporation into the module manufacturing program. Similarly, the actual module manufacturing was closely monitored by JPL and controlled by strict JPL welding specifications. As a result very few problems were encountered during module manufacture.

Only one module has experienced a weld failure. After dissection of the module it was revealed that a weld joint had not been made. The module passed the initial qualitative tests because of sufficient pressure contact at the unwelded joint. However during the final module assurance tests, before soldering into a subassembly, the module indicated abnormal conditions at high temperature.

2. Telemetry Demodulator

The ground equipment which reconstructs telemetered binary data from the noisy audio output of the S-band ground receiver has been designed and constructed. This telemetry demodulator is almost fully automated. System design considerations are covered in this report.

a. Telemetry system. The *Mariner C* telemetry system is very similar to the *Mariner R* system used successfully in 1962. The main difference is the allocation of more power to synchronization for *Mariner C* and the use of a square-wave subcarrier where a sine wave was used for *Mariner R*.

Basically, both telemetry modulation systems are PCM/PSK/PM—that is, continuous information is quantized (pulse coded) into binary bits, which control the phase (phase shift key) of a subcarrier, which phase modulates the main RF carrier. Further, both systems are coherent, with power being allocated to a separate synchronizing subcarrier which is used to produce bit and word timing

UNCLASSIFIED [redacted]

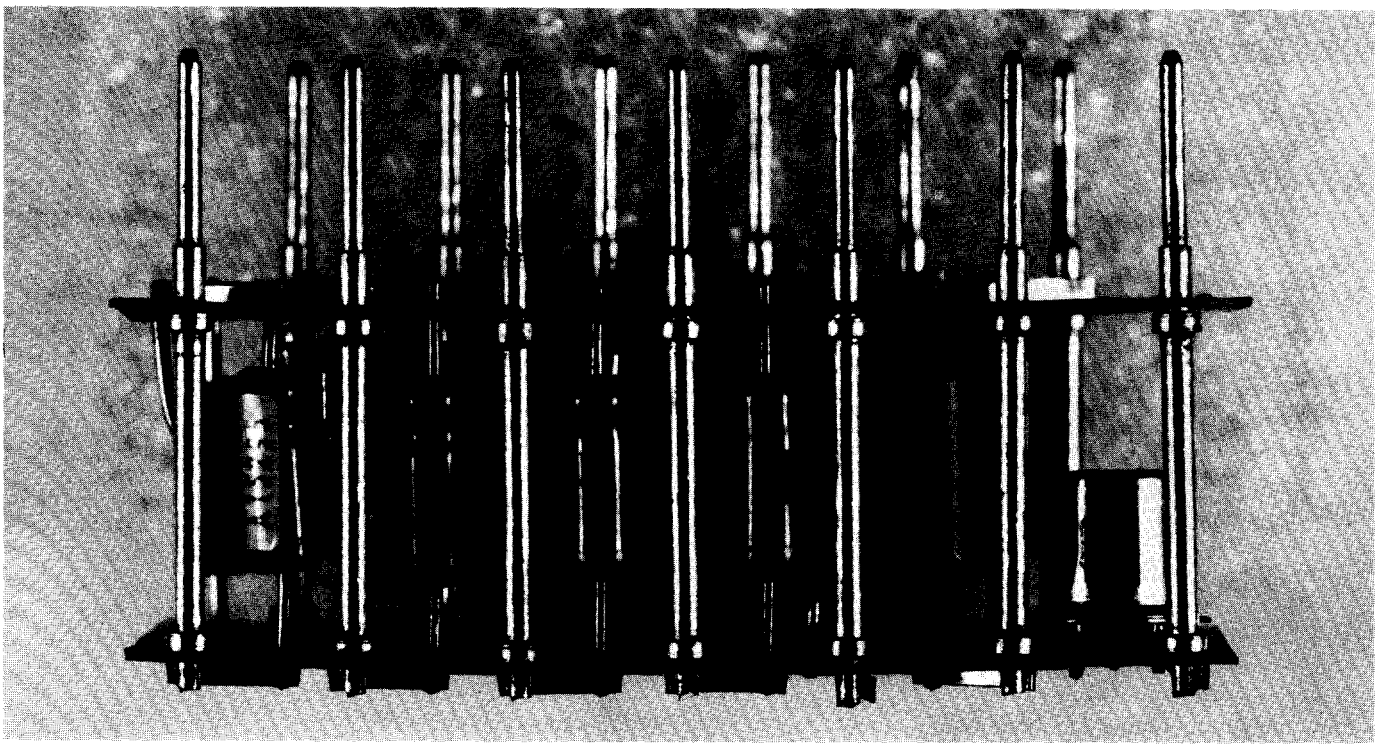

Fig. 39. Typical welded module

pulses in the ground demodulator. This synchronizing information is continuously transmitted down the channel, in parallel with the data subcarrier. It should be noted that both systems are uncoded in the sense that no error detection capability is inherent in the encoding into channel words.

A pseudonoise (PN) code is used as a "pilot tone" for synchronization. The characteristics of PN codes are well known and have been extensively discussed; hence, it will not be necessary to cover them in detail here.

Fig. 40 is a block diagram of the basic *Mariner R/ Mariner C* synchronization system. Two identical PN generators (shift registers with identical feedback taps) are used, one in the spacecraft data encoder and the other in the ground demodulator. These generators are clocked at the frequency $2f_s$ (this clock is established in the demodulator by a method to be discussed later). Synchronism between the two generators may be established because the cross-correlation function of the received code-plus-noise and the local replica code is a two-level function of the phase difference between the codes. This function is plotted in Fig. 41. The unique peak in this function may be detected from the averaged product of the received code with the replica code. Once the two code generators are in synchronism, specific states of the

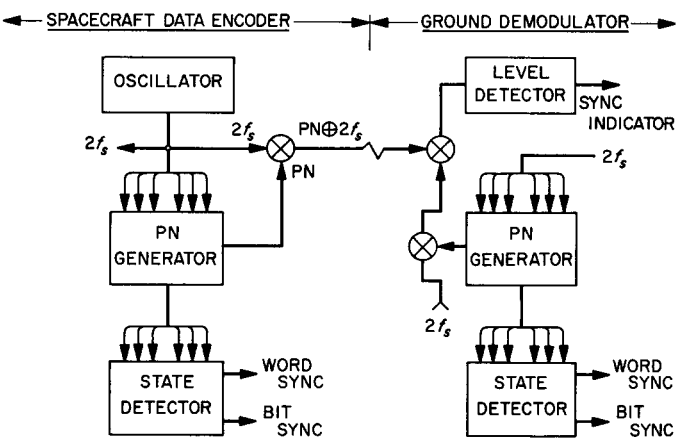

Fig. 40. Telemetry synchronization system

generators may be decoded to obtain timing information to be used for clocking data in the spacecraft encoder, and for resetting integrators (these will be shown to be matched filters) in the ground demodulator.

The power spectrum of the synchronizing code PN⊕$2f_s$[1] can be readily derived; alternative ways are to Fourier-transform the correlation function of Fig. 41, or using a result of Titsworth and Welch (Ref. 8), to square the

[1]⊕ means addition modulo 2.

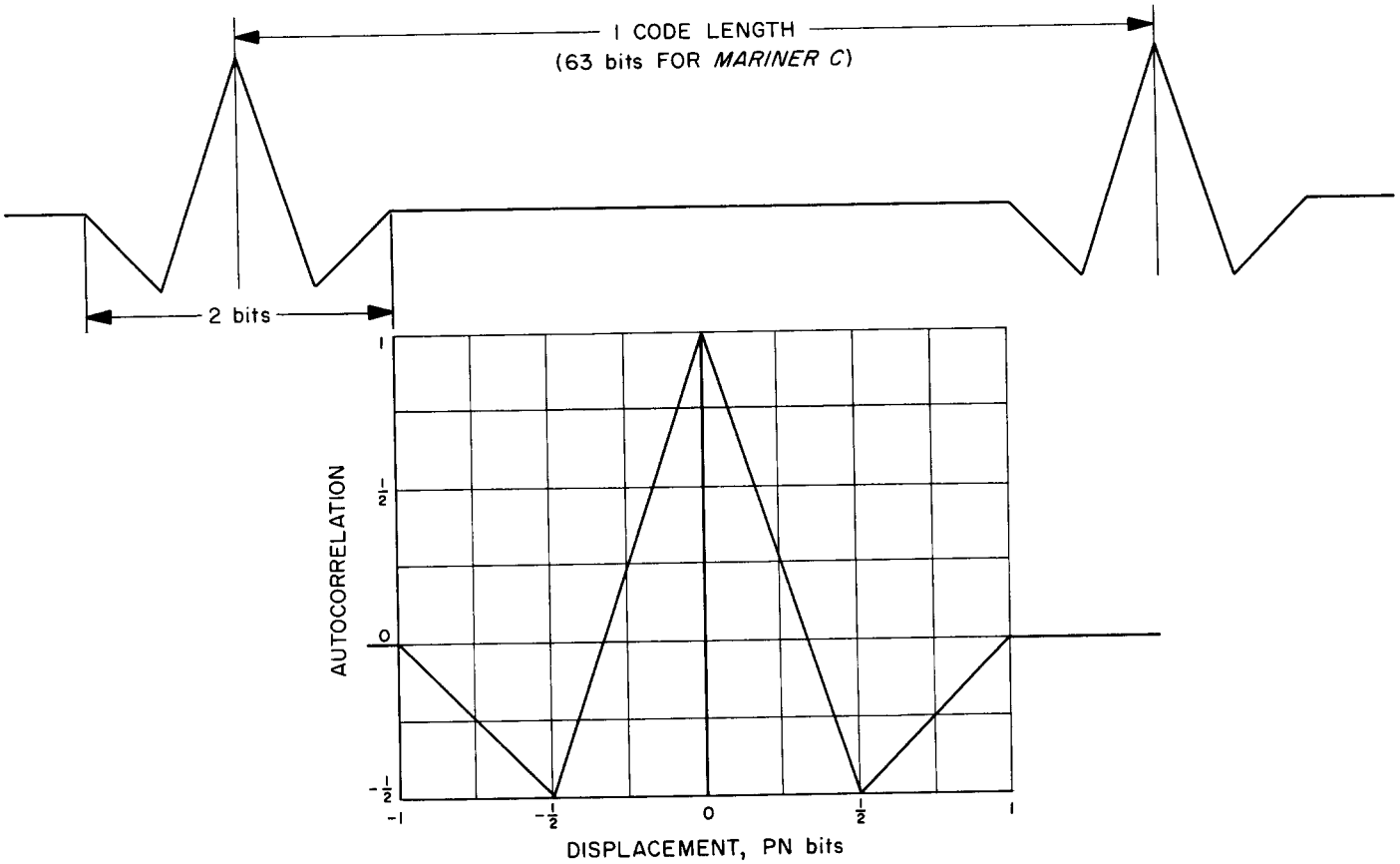

Fig. 41. Autocorrelation function of PN $\oplus$ $2f_s$, a PN code half-added to its clock

Fourier transform of a "basic switching interval" of PN $\oplus$ $2f_s$. Either method results in a power spectrum whose envelope is

$$S(f) = \frac{\sin^4\left(\frac{\pi f}{4f_s}\right)}{\left(\frac{\pi f}{4f_s}\right)^2}.$$

One side of this spectrum is plotted in Fig. 42.

The broad null at $4f_s$ in the spectrum of PN $\oplus$ $2f_s$ suggests that $4f_s$ is a logical location for the information subcarrier. For this reason, the data subcarrier was placed at $4f_s$.

The spectrum of PN $\oplus$ $2f_s$ also shows the absence of a dc component of this code, and the small amplitude of those components near dc. This is precisely why the "chopped" code PN $\oplus$ $2f_s$ is used instead of the PN code alone. PN codes are of odd $(2^n - 1)$ length, and therefore have spectra which decrease from a maximum at dc. In the case of a carrier modulated by these waveforms, components near dc in the code spectrum would be near the carrier in the composite (modulated carrier) spectrum. Since a phase-lock RF receiver "tracks out" modulation components near the carrier (more about this later), it is undesirable to use modulating signals with spectral components near dc.

The information subcarrier at $4f_s$ is phase-shift-keyed with data bits, i.e., $4f_s$ in-phase is transmitted for a data *one*, $4f_s \angle 180° = \overline{4f_s}$ for a data "0." It is desirable from the standpoint of communication efficiency to use a sine wave for the $4f_s$ subcarrier, so *Mariner R* used a phase-shift-keyed sine wave $4f_s$. However, the only means of generating an in-phase sine wave $4f_s$ in the spacecraft is to bandpass filter a square wave $4f_s$ from a flipflop divider chain. The bandpass filters (there is more than one bit rate) are a serious design problem because of the critical need for phase stability over the temperature operating range; moreover, the bandpass filters are a series element in the spacecraft data encoder, and a significant improvement in reliability may be realized if they are removed.

UNCLASSIFIED [redacted]

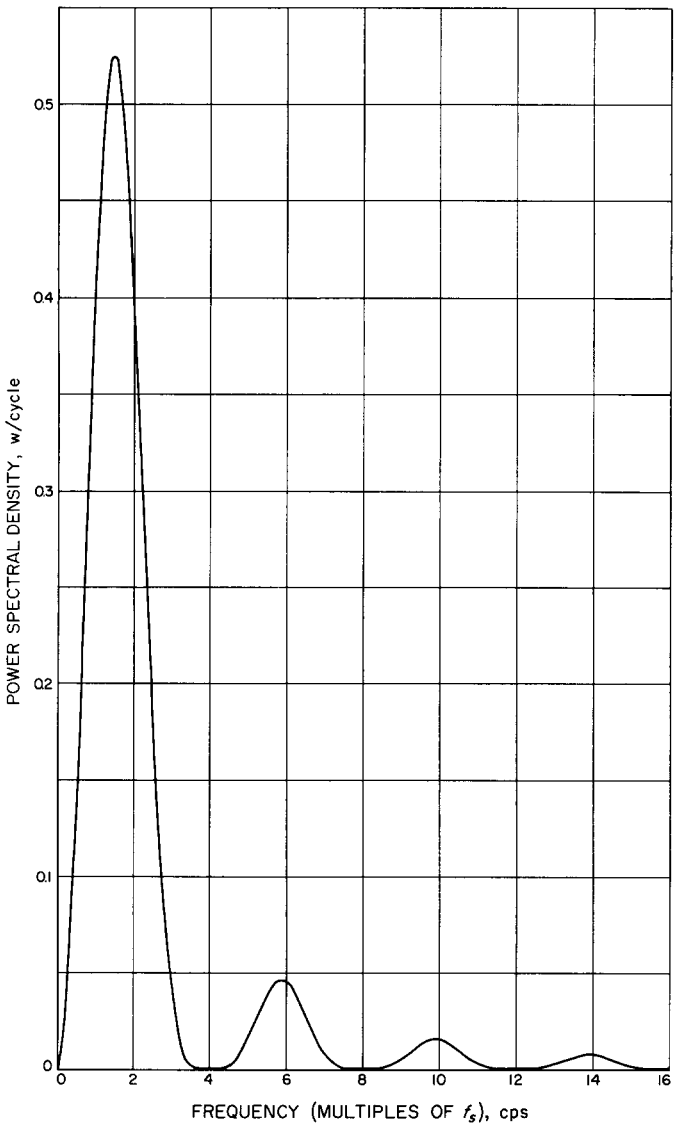

Fig. 42. Power spectrum of telemetry synchronizing code PN ⊕ $2f_s$

Furthermore, G. Fultz has shown (Ref. 9) that the use of a square-wave subcarrier with recovery of only the fundamental results in a loss of only 0.5 db compared to the sine-wave case. It would seem that the 0.9 db in the 3rd, 5th, etc., harmonics of the square wave would be lost, but Fultz has shown analytically and experimentally that the loss is actually only about 0.5 db. Briefly, the reason is that if the same power is allocated to a square subcarrier as to a sine subcarrier (in the modulator), the net loss in usable power is partially offset by a gain in transmitted power for the square-wave case.

Early in the design of the *Mariner C* telemetry system, it was decided that the gain in reliability obtained by

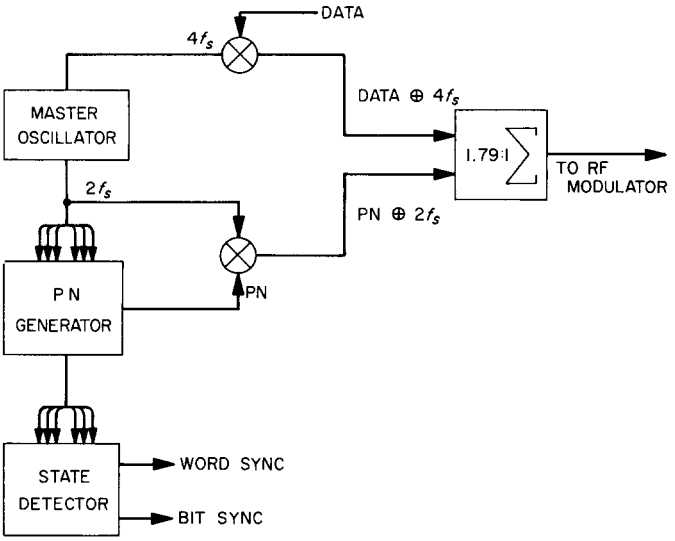

Fig. 43. Data encoder basic subcarrier/synchronizing circuits

removing the sine-wave filters was worth more than the 0.5-db performance degradation that the removal caused. Consequently, the *Mariner C* system uses a square-wave $4f_s$ data subcarrier.

A block diagram of the *Mariner C* spacecraft data encoder output circuits is shown in Fig. 43. The data ⊕ $4f_s$ subcarrier and PN ⊕ $2f_s$ subcarrier are linearly added in a ratio selected so that both subcarriers reach threshold at the same carrier level. This ratio is 1.79:1, data voltage to sync voltage, for a ratio of data power to sync power P_d/P_s, of +5.06 db; that is, approximately 24% of the total subcarrier power is allocated to the synchronizing subcarrier.

Fig. 44 is an experimentally measured power spectrum of the output voltage of the *Mariner C* data encoder. It is easy to see the $\sin^4 x/x^2$ PN ⊕ $2f_s$ spectrum with the $\sin^2 y/y^2$ data ⊕ $4f_s$ spectrum inserted in the first null of the former.

b. Receiver/demodulator interface. Fig. 45 is a partial diagram of the *Mariner C* S-band telemetry receiver. The telemetry output is derived in the receiver by multiplication of the modulated carrier at an IF by a reference derived from the carrier-tracking loop. The multiplier (carrier demodulator) input is taken from the receiver IF after the limiter which precedes the loop. Consequently, there are no large voltage excursions at the telemetry output.

UNCLASSIFIED

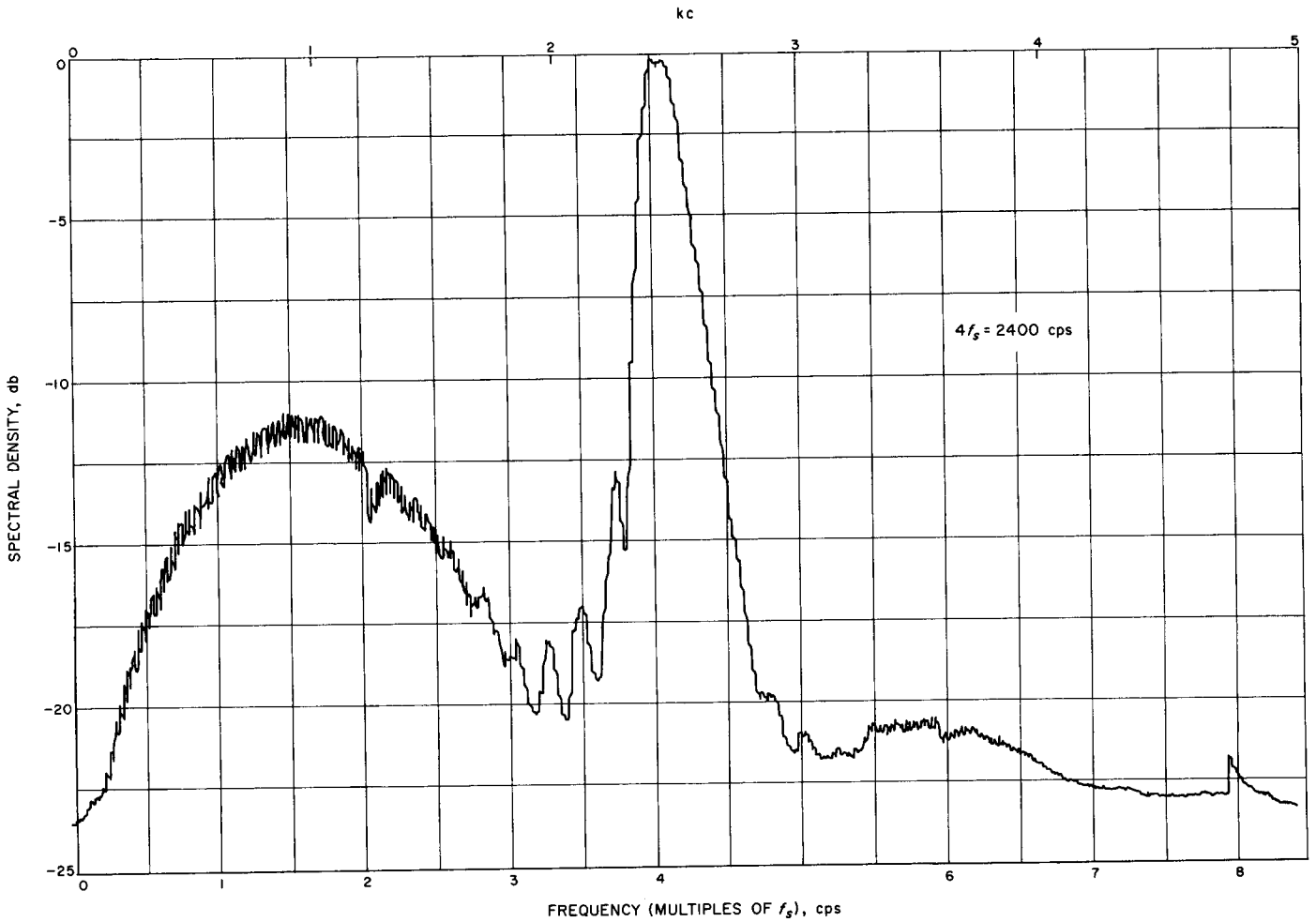

Fig. 44. Measured power spectrum of composite telemetry signal, Data $\oplus 4f_s$ and PN $\oplus 2f_s$

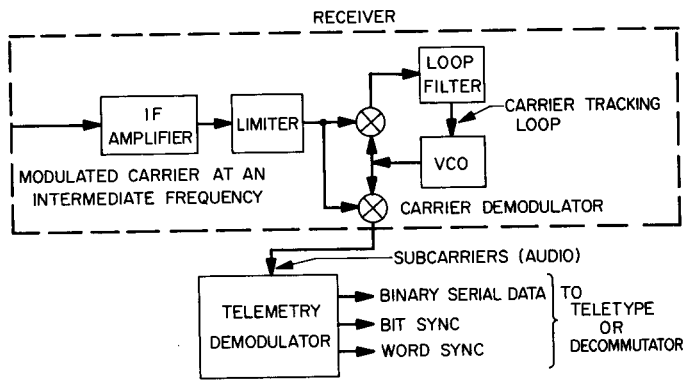

Fig. 45. Receiver-demodulator interface

The pertinent parameters of the *Mariner C* telemetry receiver are: IF bandwidth, 4.5 kc; two-sided loop bandwidth at threshold ($2B_{Lo}$), 12 cps; limiter suppression factor at threshold, (α_0) 0.075.

It was seen in Figs. 42 and 43 that there are significant components of the PN $\oplus 2f_s$ synchronizing code as close as about $0.2f_s$ to the carrier. Consequently, the fidelity of the receiver telemetry output channel close to dc is important. The requirement imposed on the receiver was that the telemetry channel low-frequency response be affected only by the carrier-tracking loop, not by any output amplifier, etc. Similarly, it was required that the high-frequency response be affected only by the receiver IF stages.

The fact that a phase-lock loop is a high-pass filter when viewed from its input terminal to the phase error (modulation output) terminal is easily seen as follows: if the loop input and output phases are $\theta_i(t)$ and $\theta_o(t)$, respectively, and its instantaneous error voltage $e(t)$, then (denoting the Laplace transform by capital letters) the conventional transfer function is $H(s) = \Theta_o(s)/\Theta_i(s)$. Also, the loop phase detector is essentially a subtractor

UNCLASSIFIED

so that $E(s) = \Theta_i(s) - \Theta_o(s)$. Consequently, the input-to-error-point transfer function is

$$E(s)/\Theta_i(s) = [\Theta_i(s) - \Theta_o(s)]/\Theta_i(s) = 1 - H(s).$$

$H(s)$ is low-pass, so that $1 - H(s)$ is high-pass.

Fig. 46 is a plot of $1 - H(s)$ for the *Mariner C* telemetry receiver. Four response curves are shown, one for each of four particular signal-to-noise ratios in the receiver IF.

It has been shown by Gilchriest (Ref. 10) that high-pass filtering of a PN sequence will distort the code autocorrelation function. The distortion would be manifested in false indications of synchronism between the local replica code and the received (filtered) code-plus-noise. In order to prevent these false lock points, a network to compensate for the $1 - H(s)$ receiver high-pass characteristic was incorporated into the *Mariner C* telemetry demodulator.

c. The telemetry demodulator; details. A block diagram of the telemetry demodulator is shown in Fig. 47. Its input is the audio signal plus noise from the receiver, and its outputs are serial (logic-level) binary data, and bit

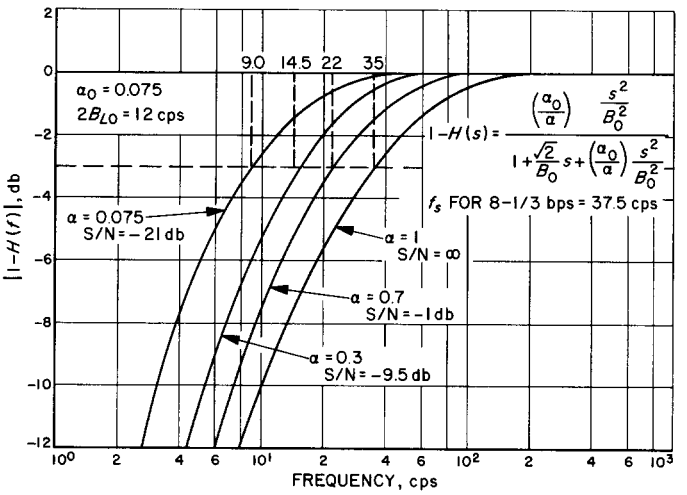
9.0 14.5 22 35
$\alpha_0 = 0.075$
$2B_{LO} = 12$ cps
$1-H(s) = \frac{\left(\frac{\alpha_0}{\alpha}\right)\frac{s^2}{B_0^2}}{1+\frac{\sqrt{2}}{B_0}s+\left(\frac{\alpha_0}{\alpha}\right)\frac{s^2}{B_0^2}}$
f_s FOR 8-1/3 bps = 37.5 cps
α = 0.075 S/N = −21 db
α = 1 S/N = ∞
α = 0.7 S/N = −1 db
α = 0.3 S/N = −9.5 db
$|1-H(f)|$, db
FREQUENCY, cps

Fig. 46. S-band receiver telemetry output characteristic

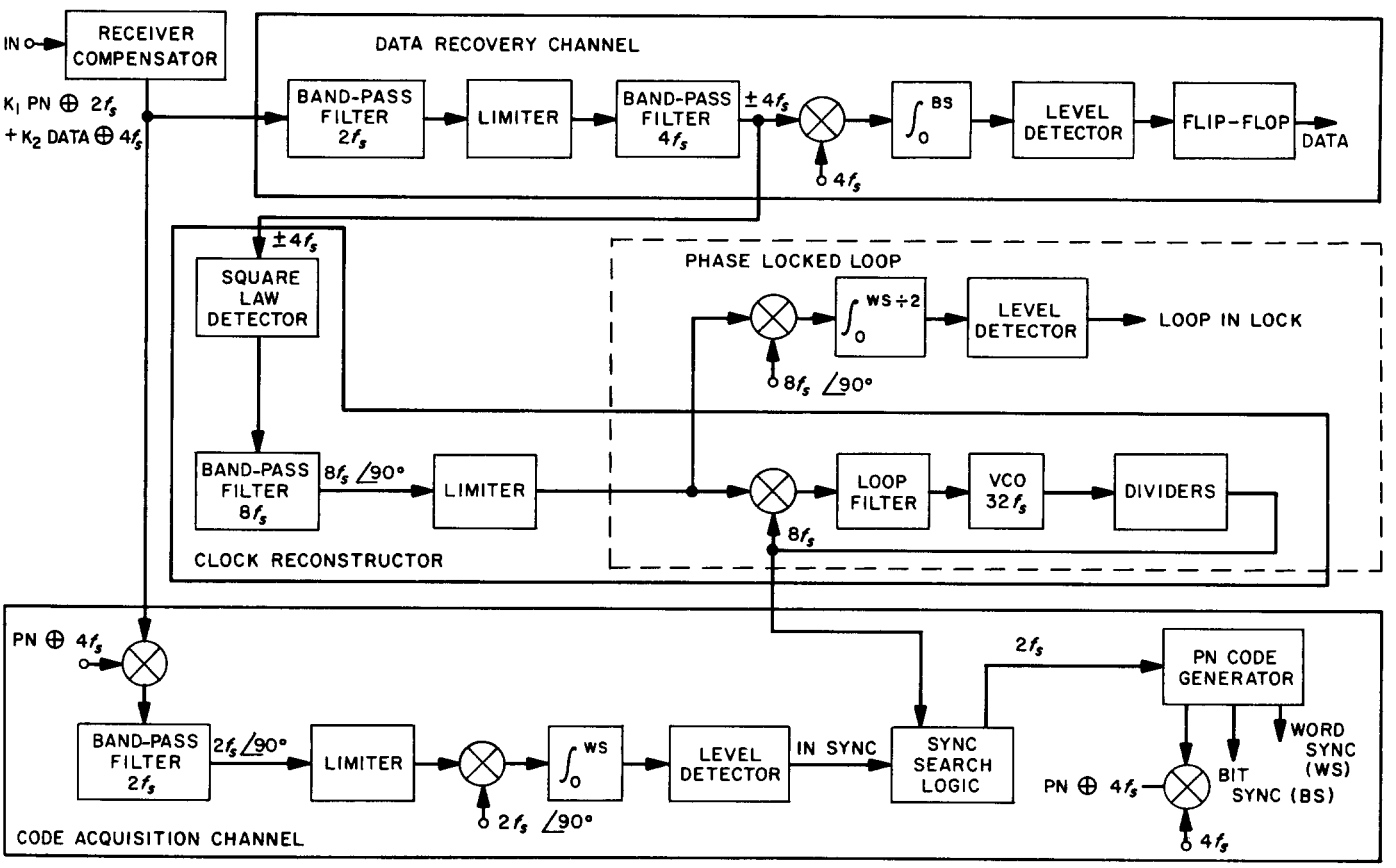

Fig. 47. PCM/PSK telemetry demodulator

and word timing pulses to a teletype encoder, decommutator, or computer.

The necessity of compensation for the receiver high-pass characteristic has been mentioned. The first element of the demodulator is an approximation to the inverse of the receiver telemetry transformer function $1 - H(s)$. It is an approximation because $1/[1 - H(s)]$ contains second order *zeros* at the origin. The approximation is quite good above about 10 cps, resulting in an over-all receiver/compensator phase shift of less than 4 deg at these frequencies. 10 cps is about $0.27f_s$ at 8⅓ bps; only about 0.8% of the total PN $\oplus$ $2f_s$ power is below 10 cps.

It will be remembered from Fig. 46 that $1 - H(s)$ is an explicit function of the limiter suppression factor, hence, its "inverse," the compensator, must vary with the signal-to-noise ratio in the IF. It was decided to provide five discrete steps of compensation, to accommodate limiter suppression factors of 1.0, 0.9, 0.7, 0.4, and 0.075. These steps correspond to signal-to-noise ratios in the receiver IF of $>+15$, $+5$, -1, -7, and -21 db, respectively.

Fig. 48 shows the distortion of the autocorrelation function of PN $\oplus$ $2f_s$ due to $1 - H(s)$ and the same function after compensation.

The remainder of the demodulator may be grouped into three major functional elements: the data recovery channel, the code acquisition channel, and the clock reconstructor. This delineation is made on Fig. 47.

The data recovery channel. The data recovery channel consists of a bandpass limiter at $4f_s$ (the location of the data subcarrier), a phase detector, an integrator reset with "bit sync," a level detector, and an output flipflop.

The Q of the bandpass limiter was chosen so that the transient response to a phase step results in 50% recovery in the duration of one PN bit. Fig. 49 will clarify this point. The delay should be one (or an integral number of) PN bit(s) because of the ease of timing generation: the delayed sync pulse may be easily generated from the PN generator No one-shot timing devices are necessary.

A chopper (i.e., multiplier by plus or minus one) is used as a phase detector, having as inputs[2] $\pm\sin 2\pi \cdot 4f_s t$ from the bandpass limiter, and sgn $(\sin 2\pi \cdot 4f_s t)$ from the local reference $4f_s$. Thus, its output is $\pm|\sin 2\pi \cdot 4f_s t|$.

A well-known result in the theory of filtering is that in the presence of gaussian noise, the filter providing the maximum ratio of output S/N to input S/N for a particular signal, called a matched filter, is characterized by an impulse response which is the time negative of the signal to which it is matched. Thus it would seem that the filter at the output of the data phase detector should have impulse response $h(t) = |\cos 2\pi \cdot 4f_s t|$. However, this impulse response is very difficult to mechanize in operational equipment. Hence, a reset integrator, with square-wave impulse response, was used in the *Mariner C* demodulator.

[2]sgn is the signum function; sgn $x = (+1, x > 0); (-1, x < 0)$; thus, sgn $(\sin \omega t)$ is a square wave at frequency ω.

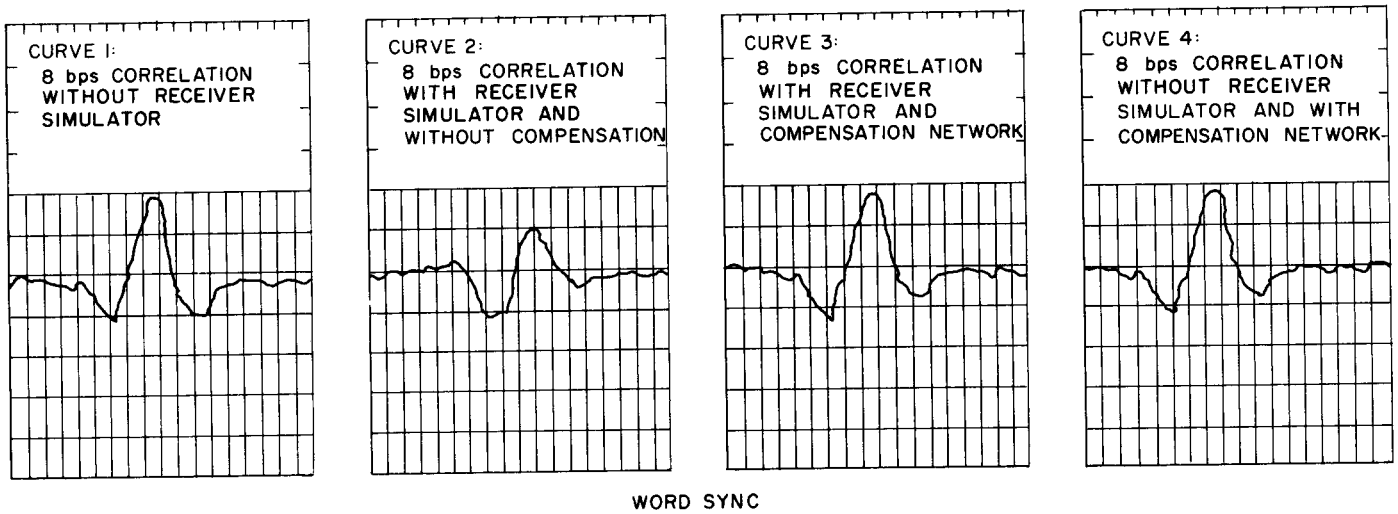
CURVE 1:
8 bps CORRELATION WITHOUT RECEIVER SIMULATOR
CURVE 2:
8 bps CORRELATION WITH RECEIVER SIMULATOR AND WITHOUT COMPENSATION
CURVE 3:
8 bps CORRELATION WITH RECEIVER SIMULATOR AND COMPENSATION NETWORK
CURVE 4:
8 bps CORRELATION WITHOUT RECEIVER SIMULATOR AND WITH COMPENSATION NETWORK
WORD SYNC

Fig. 48. Measured correlation curves of PN $\oplus$ $2f_s$ passed through a simulation of 1-*H(s)*, the receiver transfer function

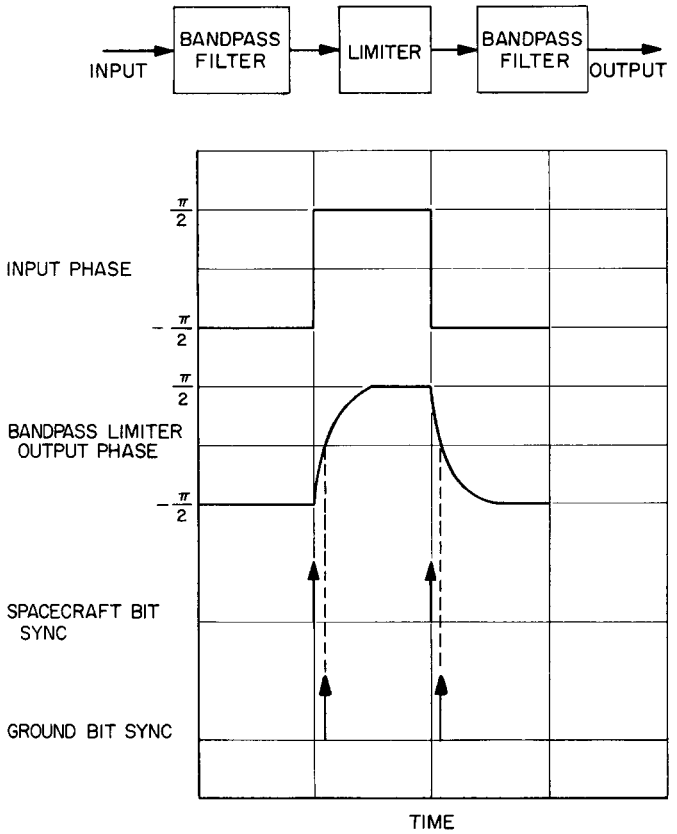

Fig. 49. Bandpass limiter transient response

The remainder of the data recovery channel is a polarity detector and output storage flipflop which is reset at the end of each integration period (bit sync).

The clock reconstructor. The clock reconstructor generates an in-phase $8f_s$ clock which is divided down to provide $4f_s$ for data detection and $2f_s$ for the PN generator clock. Ambiguities in these frequencies are automatically resolved by a method to be discussed later.

The clock reconstructor uses $\pm 4f_s$ from the bandpass limiter as an input. Its first element is a square-law detector which removes the phase reversals of $4f_s$ due to data:

$$(\pm\cos 2\pi \cdot 4f_s t)^2 = +\tfrac{1}{2} + \tfrac{1}{2}\sin 2\pi \cdot 8f_s t$$

It would seem that the large degradation in S/N to be expected through a square-law device would preclude its use. Davenport and Root (Ref. 11) show that the output S/N of a square-law device (unmodulated input, gaussian noise) is

$$(S/N)_{out} = \frac{(S/N)_{in}^2}{1 + 2(S/N)_{in}}$$

which predicts an output S/N of −9.4 db for an input S/N of −3 db. Fortunately, it is possible to use very narrow filters after the square-law detector, resulting in tolerable signal-to-noise ratios.

The bandpass filter following the square-law detector passes the $+8f_s\angle 90°$ components of the square-law output. A limiter follows the filter to take care of the expectable amplitude variation of $8f_s$ due to noise and to the bandpass limiter transient response to data changes.

A second-order phase locked loop tracks the $8f_s\angle 90°$ output of this limiter. This loop has a noise bandwidth ($2B_{Lo}$) of ¼ cps at 8⅓ bps, satisfying the requirement for a very narrow filter imposed by the square-law detector. A 2-cps bandwidth is provided for initial loop acquisition.

A conventional loop-in-lock indicator decides whether or not the loop is locked, making a decision every 14 data bits.

The code acquisition channel. The code acquisition channel accomplishes the initial synchronization of the local replica PN code with the received code, resolves all ambiguous frequencies, generates bit and word timing, and continually verifies the in-sync condition once it is attained. All of these processes are automatically controlled by logic.

The central function of the code acquisition channel is to measure the cross-correlation between the local replica code and the received code. This measurement is accomplished by multiplication of the received code by a local PN $\oplus$ $2f_s$. Thus, the autocorrelation function of Fig. 41 is traced out as a function of the phase of the local PN code.

The multiplication is performed in two steps in order to remove data channel/sync channel interaction, and to allow the inclusion of a limiter in the sync channel, so that the demodulator will be relatively independent of input signal level. This last feature is desirable from an operational standpoint.

The two-step multiplication may be seen from Fig. 47 to be (PN $\oplus$ $2f_s$) $\oplus$ (PN $\oplus$ $4f_s$) = $2f_s\angle 90°$, followed by a bandpass filter at $2f_s$ and a limiter, followed by $2f_s\angle 90° \oplus 2f_s\angle 90° = 1$. The Q of the bandpass filter was chosen so that a high enough S/N is maintained into the limiter so that its suppression factor does not fall below 0.8. This Q turned out to be 28. The necessity of a high

UNCLASSIFIED [redacted]

limiter suppression factor has to do with the use of a fixed decision threshold for rejection of false lock points, which will be discussed shortly.

The fact that this two-step multiplication scheme results in a minimum interference by $\pm 4f_s$ in the code recovery channel may be seen by consideration of the power spectrum at the output of the first chopper, which multiplies the input signal

$$\text{data} \oplus 4f_s + PN \oplus 2f_s$$

(power division has been neglected for simplicity) by the local PN $\oplus 4f_s$. The resultant signal is easily seen to be date $\oplus$ PN + $2f_s \oplus 4f_s$ = data $\oplus$ PN + $2f_s \angle 90°$. The data $\oplus$ PN term is clearly an interference term, since $2f_s \angle 90°$ is the signal of interest in this channel.

The power spectrum of data $\oplus$ PN is

$$\frac{1}{f_s} \frac{\sin^2\left(\frac{\pi f}{2f_s}\right)}{\left(\frac{\pi f}{2f_s}\right)^2}$$

which clearly has a null at $2f_s$. Thus, filtering at $2f_s$ will recover $2f_s \angle 90°$ but reject most of the data $\oplus$ PN components. This prediction has been well borne out by experiment. A different two-step multiplication scheme was used for *Mariner R* which resulted in a large incidental AM on the first multiplier output. This *Mariner C* scheme reduces this incidental AM to a negligible value, providing measurably better sync-channel performance.

The output of the second multiplier is operated upon by a reset integrator, which is a true matched filter, because its input is a corrupted dc level whose amplitude is proportional to the cross-correlation.

Close inspection will reveal that throughout the discussion the local code has been assumed to be aligned in phase with the received code. Of course, the reason for existence of the code acquisition channel is that this assumption is not true until the peak in the autocorrelation function (Fig. 41) is detected. The process of tracing out the autocorrelation function and detecting its peak is accomplished by periodically interrupting the local PN generator clock to effectively step the phase of the local code with respect to the received code. The correlation at each step is compared to a threshold, and if it exceeds the threshold it is taken to represent the proper (in-lock) local code phase.[3]

It is clear that the increment which the local code is stepped per decision (in terms of fractions of a code bit), and the time taken to make a decision as to whether the correlation is above or below the threshold, determine the parameters of the random variable which is the time taken to lockup. The step increments should be as large as possible to minimize lockup time. The decision time, determined by the integration time in the reset integrator, is designable. A larger integration time results in a lower false-alarm rate because the ratio of signal energy to noise spectral density increases with integration time, for a fixed signal power.

The maximum step increment is determined by the facts that the phase-lock loop produces an in-phase $8f_s$, and the PN generator clock is $2f_s$. Division-by-two of $8f_s$ results in $\pm 4f_s$, a twofold ambiguity. Division of $\pm 4f_s$ results in $\pm\pm 2f_s$, i.e., the code clock has an inherent fourfold ambiguity. Therefore, every ¼ bit shift of the local PN code must be tested.

It is well to reconsider the correlation curve of Fig. 41 in the light of the information that each ¼-bit step of the local code phase must be investigated. Figure 50 is a

[3]Comparison with a threshold is suboptimal: A better way would be to make a "largest-of" selection from samples at all possible code phases. The suboptimal method was used because it performs adequately with much less hardware.

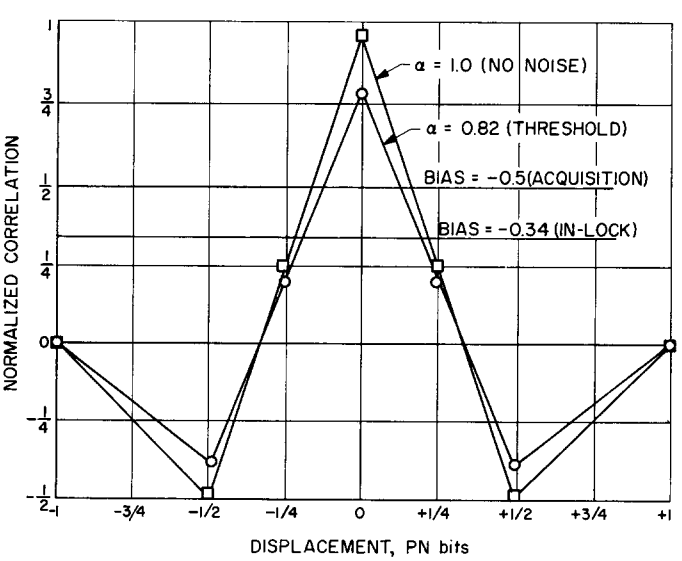

Fig. 50. Sync correlation curve illustrating the effect of the limiter suppression

UNCLASSIFIED [redacted]

redrawing of Fig. 41 with the ¼-code-bit points identified on the curve. Also, Fig. 50 shows the effect of limiter suppression factor on the correlation curve, which will be dealt with presently.

It may be seen from Fig. 50 that there are correlations of normalized magnitude $+¼$ at $+¼$ code bit and $-¼$ code bit from the inlock point (the correlations outside the two-bit interval shown on Fig. 42 are all zero). The presence of these positive points requires that a bias be added to the correlation voltage in order that a simple polarity detector may be used to discern between the in-phase point at (0, 1) and the points at $(\pm¼, ¼)$. A reasonable value for this bias is midway between $+¼$ and $+1$, at $+⅝$, where it would seem that the probability of a false alarm would be the same at the $-¼$, 0, and $+¼$ bit points. This appearance is false, because the real-world correlation curve is somewhat distorted, and the effect of limiter suppression is to reduce the amplitude of the correlation curve. In practice, the bias is set at ½ during the acquisition process and switched automatically to 0.34 after acquisition. These values were determined experimentally to produce the best compromise. A rigorous analysis must await solution of the complete probability density function of a limiter output.

The mechanization of the code step-by circuits is to delete one cycle of $8f_s$ per word time, while out-of-lock, from the divider chain. This process effectively deletes ½ cycle of $4f_s$, and ¼ cycle of $2f_s$, as desired. The ambiguity in $4f_s$ is automatically resolved by acquisition of the PN code at $2f_s$; if $2f_s$ is in phase, then all of its harmonics will also be in phase.

The interval of integration chosen for the in-lock decision was one word-time (seven bits). This period results in a probability of acquisition (measured) of 0.89 per code cycle and a probability of false alarm (once lock is attained) of 0.01, at data threshold. The *Mariner C* demodulator requires three consecutive out-of-lock indications before it automatically enters a sync search mode, so that the probability of falsely dropping lock is $(10^{-2})^3 = 10^{-6}$. These figures are all at data threshold, where the probability of a data bit error is 1/200.

The time to sync acquisition, once the phase-locked loop has been normally locked (a process which takes 0–2 min depending on the operator and signal conditions) is a random variable whose mean is 106 sec at no-noise and 118 sec at data threshold, both at 8⅓ bps. At higher bit rates these figures are reduced proportionally.

F. Space Sciences

1. TV Subsystem Camera-Shutter Electronics

Experience with the *Mariner C* TV subsystem flight cameras has indicated that, with extended operation, the shutter action may become uncertain. This has been attributed to the increased friction caused by wear. It has been noted that, at times when "open-shutter" has been maintained, "close-shutter" has faltered. Among other steps that have been taken to alleviate this problem, the electronic mechanization has been more closely investigated in order to determine operating margins and possible improvements.

a. Description of electromechanism. The TV camera used a two-pulse electromechanical shutter where the exposure time is determined by the spacing between the pulses. The shutter drive is by rotary electrical solenoid. The axial thrust of the solenoid plunger is transferred to rotary motion by a self-contained mechanism, using the principle of a frictionless screw thread. The screw-thread action is provided by a suitably indented rotary plate that is driven by the plunger through ball bearings. The relationship of the drive to the magnetic circuit is illustrated in Fig. 51. With a nominal power input to the solenoid coil of 14 w, 0.5 amp at 28 v, a torque of 3.5 in.-oz is produced at the plate. The associated electronic circuitry provides two synchronized power pulses that have an absolute minimum drain on the spacecraft power supply. This is accomplished by using charged capacitors as the source of supply for the solenoid drive. The basic circuitry

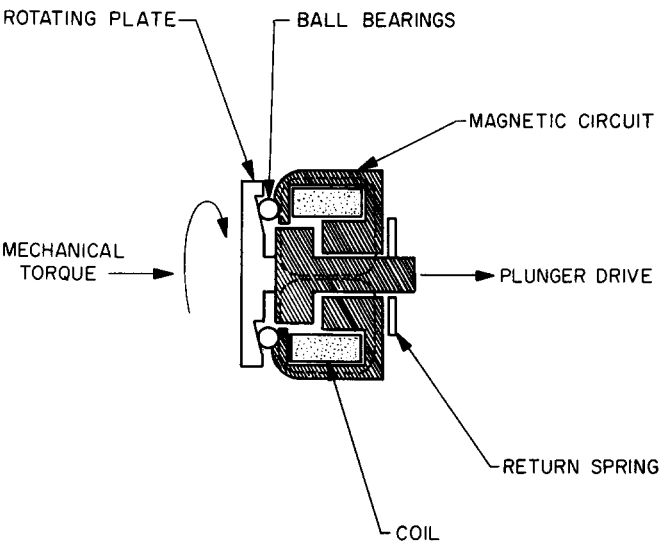

Fig. 51. Magnetic circuit operation of *Mariner C* TV subsystem shutter solenoid

UNCLASSIFIED [redacted]

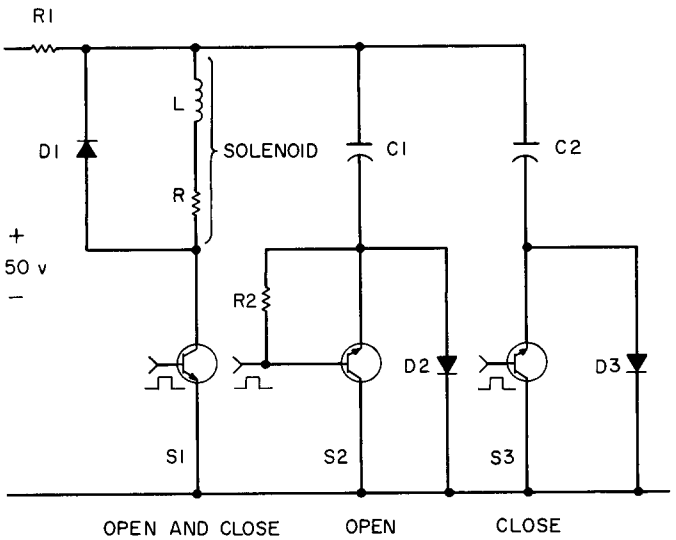

Fig. 52. Capacitor discharge drive to solenoid

is shown in Fig. 52. Drive pulses to the solenoid are controlled by power transistor gates. The power transistor switch S1 closes with alternate closure of S2 and S3, the open and close gates. At all other times, S1, S2, and S3 are open and capacitors C1 and C2 are charging through diodes D2 and D3, respectively. The charging time is the time between pictures: 48 sec. Unwanted energy stored in the solenoid inductance after application of the pulse is discharged through D1 after S1, S2, and S3 open.

b. Efficiency. The relationship between electrical power input and torque is of interest. To a close approximation the torque produced by the solenoid is a direct function of power input, i.e.,

$$F = k_1 W = k_2 I^2.$$

It should be noted that power dissipated in the resistive component of the coil performs no useful work. For this solenoid, close to 90% of the total power input is dissipated in resistive losses. Power applied following plunger operation is also wasted power, but possible losses here can be minimized by controlling the pulse length. A preliminary estimate of electromechanical conversion efficiency η may be made by expressing the peak power taken to drive the shutter in terms of the current and an effective electrical resistance R_e that will be higher than R, the coil dc resistance. Neglecting for the present incidental electromechanical losses that are difficult to assess,

$$\eta = \frac{R_e - R}{R_e}.$$

For the solenoid of interest,

$$\eta = \frac{100 - 85}{100} = 0.15.$$

A conversion factor of 1 w = 141.5 in.-oz/sec permits an estimate of the torque F for a given power pulse. Thus,

$$F = 141.5\, W t \eta,$$

where W is the peak power, and t is the width of the applied current pulse. An optimum pulse width has been found to be 25 msec; hence, for an applied peak power of 14 w, $F = 141.5 \times 14 \times 0.025 \times 0.15 = 7.5$ in.-oz.

The manufacturer's specified torque verified in the laboratory for a 14-w input is 3.5 in.-oz, which reduces the efficiency estimated to above 0.07. This latter figure includes incidental electromechanical losses not allowed for in the preliminary estimate. The effective torque produced is thus 0.25 in.-oz/w. The required minimum power input to activate the solenoid only against the solenoid return spring was measured to be 6 w or 1.5 in.-oz torque. With the shutter mechanism attached to the solenoid, the minimum power input required was 12 w or 3 in.-oz torque. The electronic drive for *Mariner C* was designed for a minimum peak-power pulse for all expected conditions of 16 w or a torque of 4.0 in.-oz. This provides a 30% reserve for a normally operating shutter mechanism.

c. Available power. Power for the solenoid is derived from a charged capacitor. The input energy requirement W_i for a 16-w, 25-msec pulse is $16 \times 0.025 = 0.4$ w-sec. The capacitor discharge must be adequate to supply this solenoid energy over the 25-msec interval. The percentage of power utilized may be determined by integration in terms of the discharge time constant. Thus, the normalized power discharge

$$W_d = \int_0^t \exp\left(-\frac{2t}{T}\right) dt = \frac{1}{2}\left[\exp\left(-\frac{2t}{T}\right)\right]_0^t$$

When t is infinite, $W_d = 0.5$. For a discharge capacitance $C = 660$ μf, a solenoid $R = 85$ ohms, $T = RC = 56$ msec. The normalized power removed from the capacitor during a 25-msec pulse is $W_d = 1 - 0.4/2 = 0.3$. Hence, 60% of the stored energy is available for use in the first 25 msec. The power discharge is illustrated in Fig. 53. The available stored energy in the capacitor

$$W_s = \frac{1}{2} C E^2 = 0.83 \text{ w-sec}$$

UNCLASSIFIED [redacted]

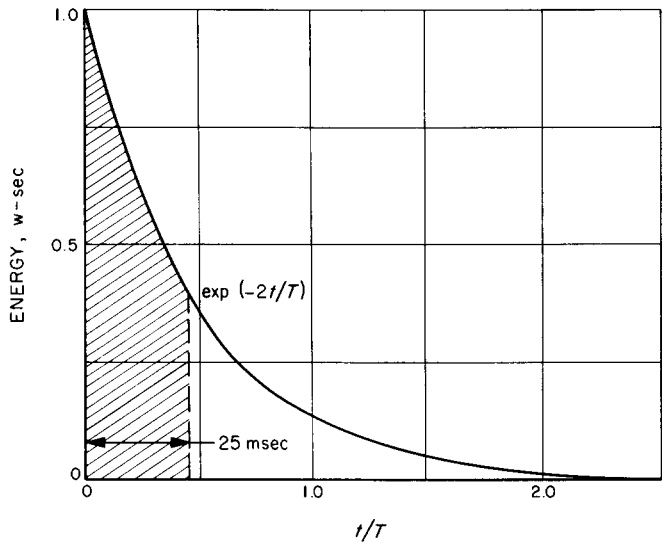

Fig. 53. Normalized energy discharge of capacitor

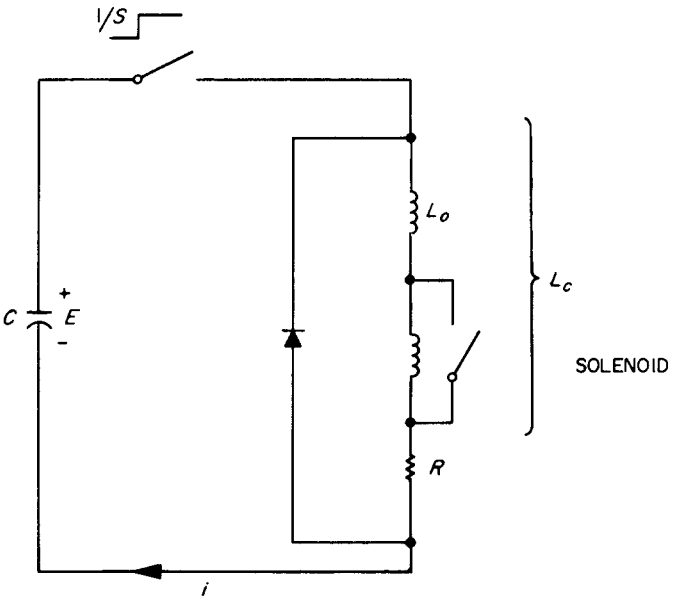

Fig. 54. Solenoid operation as a switched impedance function

for a charging potential of 50 v. Hence, the available power in a 25-msec interval $W_d = 0.83 \times 0.6 = 0.5$ w-sec. This indicates that the capacitor storage is adequate for a 16-w drive pulse of 25-msec duration.

d. Current pulse. Because of the presence of storage elements, deviations from an ideal square-wave current pulse are to be expected. The current pulse waveform may be determined from the impedance function *LCR* that represents the solenoid circuit shown in Fig. 54. The transform current

$$I(s) = \frac{E(s)}{sL + R + \frac{1}{sC}}.$$

For unit voltage drive,

$$i = \frac{\frac{1}{s} \cdot \frac{s}{L}}{s^2 + \frac{R}{L}s + \frac{1}{LC}} = \frac{\frac{1}{L}}{(s + \alpha_1)(s + \alpha_2)},$$

where α_1 and α_2 are the roots of the equations. Using the Laplace transformation, the solution is of the form

$$i = A_1 \exp(-\alpha_1 t) + A_2 \exp(-\alpha_2 t),$$

where

$$\alpha_{1,2} = -\frac{R}{2L} \pm \left[\left(\frac{R}{2L}\right)^2 - \left(\frac{1}{LC}\right)\right]^{1/2}.$$

In this particular case where $(R/2L)^2$ is substantially greater than $1/LC$, the roots of the equation may be expressed with sufficient accuracy and with more meaning in terms of the time constants RC and L/R, noting $(1-\delta)^{1/2} \approx 1 - \delta/2$. Hence,

$$i = \frac{\frac{1}{L}}{\left(s + \frac{1}{RC}\right)\left(s + \frac{R}{L}\right)},$$

so that

$$i = A_1 \exp\left(-\frac{t}{RC}\right) + A_2 \exp\left(-\frac{Rt}{L}\right)$$

Evaluating the constants by partial fractions,

$$A_1 = \left.\frac{1}{s + \frac{R}{L}}\right|_{S=-1/RC} \qquad A_2 = \left.\frac{1}{s + \frac{1}{RC}}\right|_{S=-R/L}$$

$$\approx \frac{RCL}{R^2CL} \qquad \approx \frac{RCL}{-R^2CL} \quad \text{as } R^2C > 4L$$

$$= \frac{L}{R} \qquad = -\frac{L}{R}$$

For a voltage pulse of amplitude E,

$$i = \frac{E}{R}\left[\exp\left(-\frac{t}{RC}\right) - \exp\left(-\frac{Rt}{L}\right)\right].$$

The current is seen to be the difference of two exponentials associated with the time constants of L and C.

The value of L may be found by applying a step function current of appropriate magnitude to the solenoid, first with the relay held open and then with the relay held closed. In this particular application, 400-cps bridge measurements of L without dc current are quite erroneous. The value of L is estimated from the time-constant characteristic as observed on an oscilloscope trace. The measured value for the solenoid relay held open was $L_o = 0.22H$, and that for the solenoid held closed was $L_c = 0.5H$. Briefly, the flow of solenoid current with the application of a voltage pulse is as follows: At transistor switch closure, e_L is in direct oppostion to e_c so that the current at t_0 is zero. The current rapidly rises to a peak as e_L drops to zero. After reaching a peak, i steadily decreases as the capacitor discharges. However, as the plunger is fully inserted, L is suddenly increased. The inductive potential e_L is, at this time, in phase conjunction with e_c by virtue of

$$e_L = -L\frac{di}{dt}.$$

The resultant discontinuity produces a current boost to the solenoid. The switch now opens, and the inductive energy is discharged through diode D1. Using the equation developed above, a plot of current versus time was made, as shown in Fig. 55. After the initial current surge, $E^{-(R/L)t}$ becomes insignificant, and the current falls off at the rate of $E^{-(t/RC)}$. Following switch opening at $t = 25$ msec, the current decays at the rate of $E^{-(R/L)t}$. For comparison purposes, a photograph of the actual current waveform is shown in Fig. 56(a). The waveforms agree within the tolerances of the various circuit parameters, including the value of the applied potential.

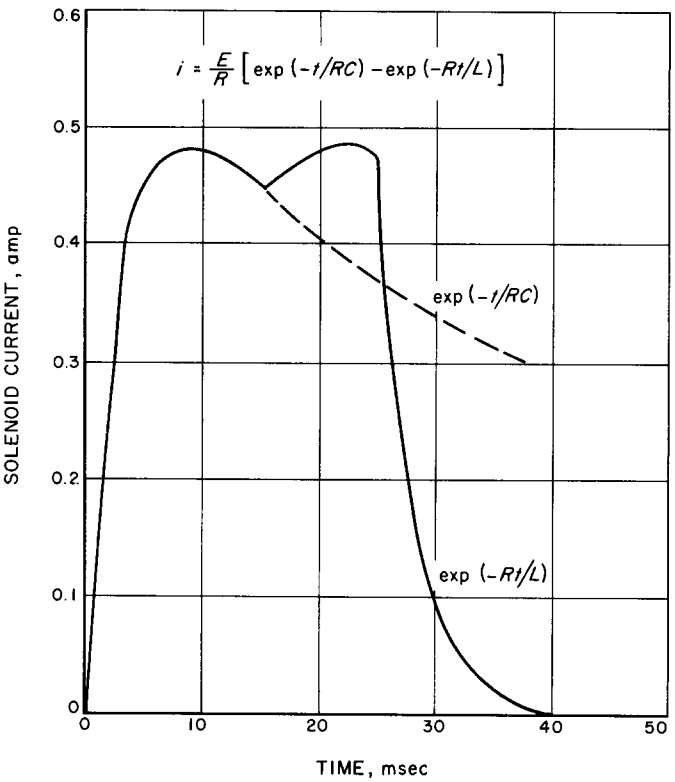

Fig. 55. Calculated solenoid-current waveform

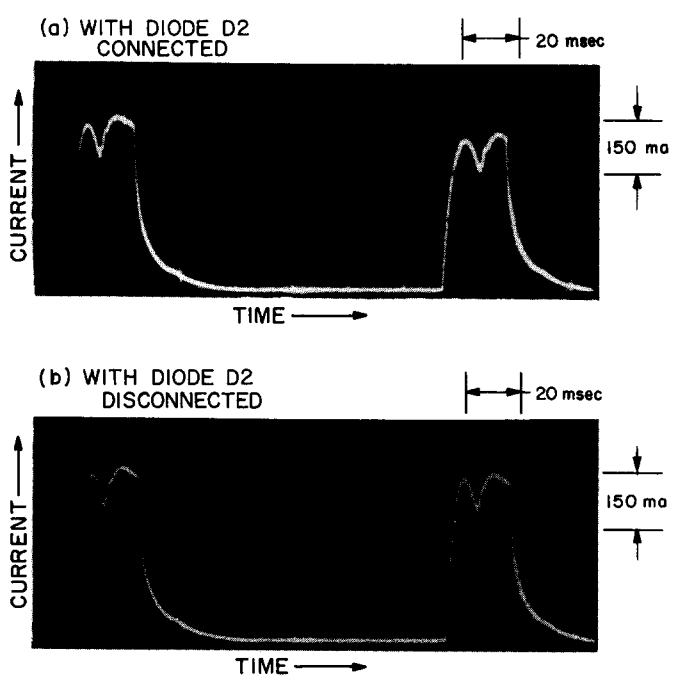

Fig. 56. Measured solenoid-current waveform

e. Unequal pulses. Fig. 56(a) indicates that the close-current pulse magnitude is somewhat less than that of the open pulse, representing a 20% drop in torque. Returning to Fig. 52, the open pulse is produced when C1 discharges through S1 and S2. A short time later (200 msec or less), S1 and S3 close to produce the close-current pulse. However, part of the charge on C2 boosts the charge on C1 via the diode D2, resulting in a loss of energy to the solenoid. This loss in charge may be prevented by removing the diode D2. This deletion is possible since the charge cycle can, in fact, proceed through the transistor switch S2 without the diode D2 being connected. This is because, during charge, the base-collector contact becomes reverse-biased and acts as a forward-biased diode. But, in this case, the base resistor R2 is sufficiently high to allow only

a small fraction of the charge on C2 to be transferred and yet is inconsequential in the charging of C1. Without the diode, the current pulses are almost identical, as shown in Fig. 56(b).

Replacement of the transistor switches by hard-circuit elements, i.e., mechanical relays, has indicated that any losses introduced by the transistor switching are negligible.

f. Conclusion. The design of the shutter drive illustrates a typical difficulty encountered with an integrated electromechanical subassembly. Whereas for the mechanical designer a 50% increase in torque requirement probably presents no real hardship, for the electronic designer a change in power, say from 20 to 30 w, may represent a complete redesign with the replacement of many of the key components.

In the design of the *Mariner* TV subsystem shutter mechanization, an inadequate allowance was made for any increased torque requirements produced by wear. However, the margin of power reserve built into the electronics appears to be sufficient to accommodate a 50% increase in the torque demand resulting from wear. Equalizing the pulse drive on open- and close-shutter operation increases the operating margin. Extensive tests give no indication of any new problems arising when D2 is disconnected.

G. Supporting Activities

1. Environmental Test Program

From mid-June to mid-August, 1964 the following tests associated with the *Mariner C* program were performed by the Environmental and Dynamic Test Laboratory (Table 9): 177 experimental, 95 type-approval, and 151 flight-acceptance.

2. Vibration

a. Mariner C. Flight-acceptance vibration tests were performed on *Mariner C-2* and *Mariner C-3* during July and August (Fig. 57). JPL Spec. MCO-50308-FAT was the governing specification. Test conditions which were satisfactorily met were:

Transverse (*xy*-axes through bays II-VI and through bays IV-VIII).

Table 9. *Mariner* C usage of environmental test facilities from June 15 to August 15, 1964

Facility	No. of tests
Vibration	182
Acoustic	0
Centrifuge	13
Shock	20
Handling shock	4
Temperature	17
Explosive atmosphere	2
Vacuum	185
Total	423

Shaped noise: 10.7 *g* rms; duration, 60 sec. The spectrum for equalization verification and flight-acceptance level runs was flat at 0.07 g^2/cps from 550 to 2000 cps and rolled off at the rate of 6 db/octave below 550 cps and 24 db/octave above 2000 cps.

Sine sweep Range, 200–20–200 cps; level, 0.5 *g* rms; sweep rate, 2 octaves/min; duration, 3 min 16 sec.

Longitudinal (*z-axis*).

Shaped noise: The conditions were the same as for the *xy*-axis.

Sine sweep: Range, 200–20–200 cps; level, 1.0 *g* rms; sweep rate, 2 octaves/min; duration, 3 min 16 sec.

Control during the low frequency tests used the peak reading of 6 accelerometers located around the periphery of the vibration fixture at 60-deg intervals. The force limiting was set at 4500 lb for vibration in the lateral directions and 6500 lb for vibration along the *z*-axis. The control during random noise tests used the quadratic mean of the 6 accelerometers. (The quadratic mean circuit supplies a voltage for control of the vibration exciter which is proportional to the square root of the sum of the squared outputs of each accelerometer. The circuit provides a spatial average of the acceleration inputs to the spacecraft. This prevents over- or under-testing by minimizing acceleration gradients across the interface between the spacecraft and the vibration exciter.)

3. Thermal Vacuum Testing

a. Mariner C life tests. Life tests have recently started on the following *Mariner C* equipment (Fig. 58): gyro control assembly 7A2 (6 wk); scan actuator (50 days);

UNCLASSIFIED [redacted]

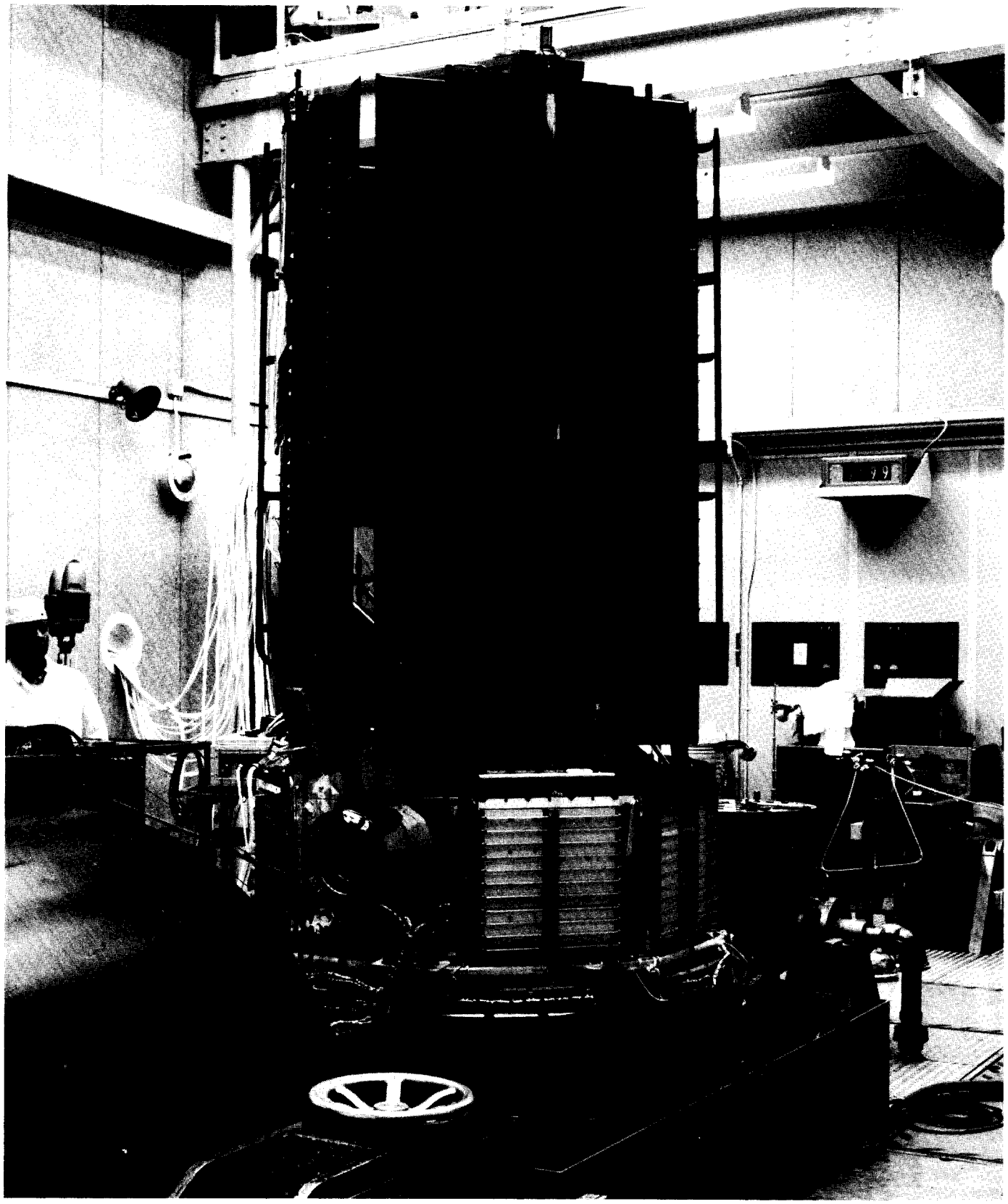

Fig. 57. *Mariner C-3* flight-acceptance vibration test

UNCLASSIFIED [redacted]

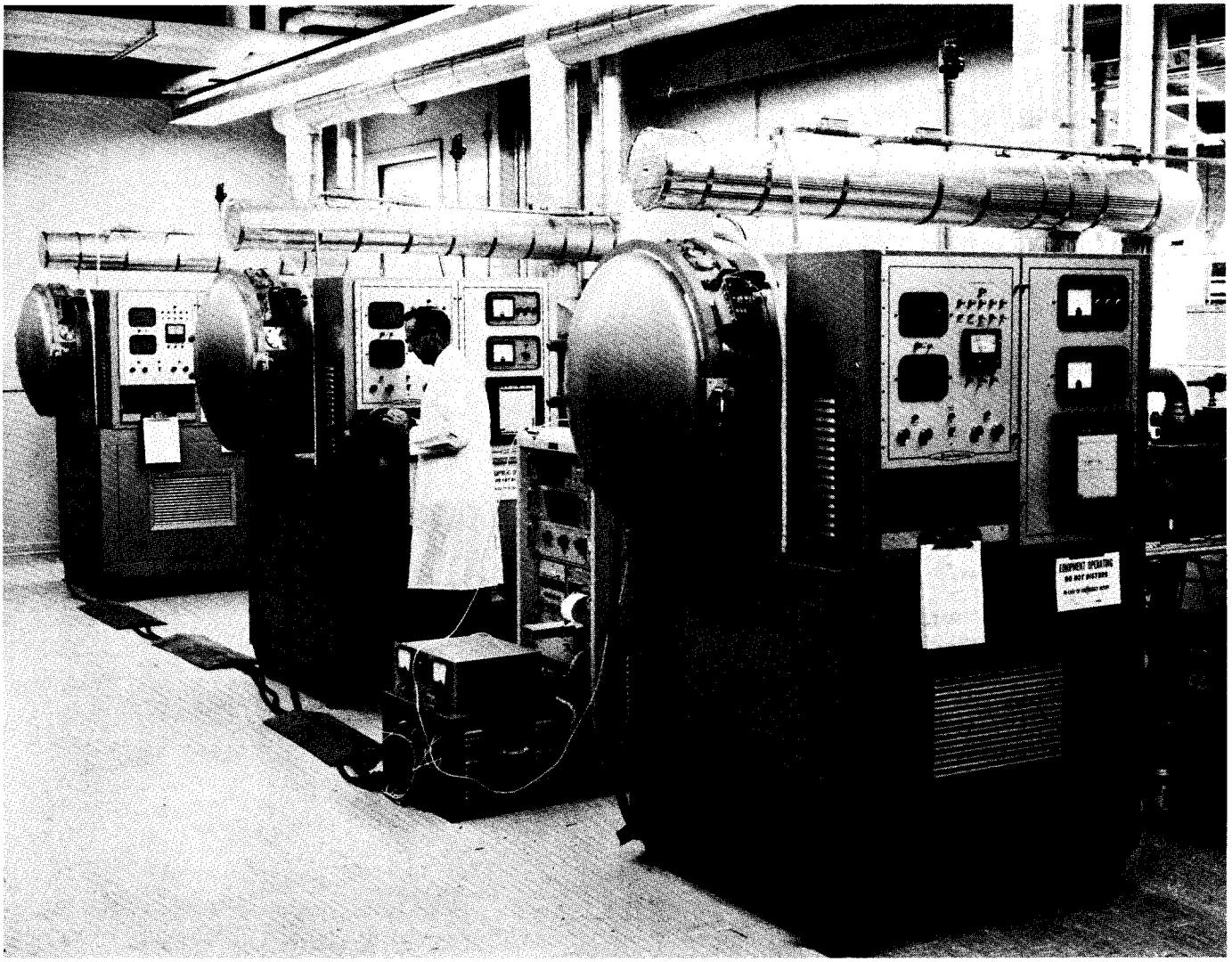

Fig. 58. *Mariner* C life tests in 30- × 60-in. horizontal thermal-vacuum chambers

video storage subsystem (9 mo); power subsystem (5 mo); battery (8 mo); science cover assembly and support; latch actuator (50 days); solar panel retarder, cruise damper, boost damper; separation initiation timer (6 mo).

The tests are to determine the effect of long term exposure to thermal-vacuum environments; they are being conducted in the 30- × 50-in. horizontal chambers and 18-in. bell jars and in the 30- × 60-in. horizontal chambers.

References

1. "*Mariner* C 1964 Cabling," *SPS 37-19*, Vol. II, pp. 65–67, Jet Propulsion Laboratory, Pasadena, California, January 31, 1963 (Confidential).

2. "Cabling," *SPS 37-21*, Vol. II, p. 20, Jet Propulsion Laboratory, Pasadena, California, May 31, 1963 (Confidential).

UNCLASSIFIED

References (cont'd)

3. "Packaging," *SPS 37-24,* Vol. II, pp. 6–18, Jet Propulsion Laboratory, Pasadena, California, November 30, 1963 (Confidential).

4. "Roll Acquisition" and "Canopus Tracker," *SPS 37-21,* Vol. II, pp. 39–51, Jet Propulsion Laboratory, Pasadena, California, May 31, 1963 (Confidential).

5. Elsasser, H., and Hang, V., "Photoelectron Surface Photometry of the Southern and Northern Milky Way in Two Colors and the Structure of the Galactic System," Report No. 48, Astronomical Institute of the University of Tübingen, *Zeitschrift für Astrophysik,* Vol. 50, No. 196: pp. 121–144, 1959.

6. "*Mariner* (1962) Command Subsystem," *SPS 37-17,* Vol. VI, pp. 29–31, Jet Propulsion Laboratory, Pasadena, California, October 31, 1962.

7. *Research Summary* Nos. 36-5 through 36-10, November 1, 1960–September 1, 1961; *SPS 37-17,* Vol. IV, October 31, 1962.

8. Titsworth, R. C., and Welch, L. R., "Power Spectra of Signals Modulated by Random and Pseudorandom Sequences," Technical Report 32-140, Jet Propulsion Laboratory, Pasadena, Calif., October 10, 1961.

9. Fultz, G. L., "Square Wave Subcarrier for *Mariner* Telemetry," *SPS 37-18,* Vol. IV, pp. 202–207, Jet Propulsion Laboratory, Pasadena, California, December 31, 1962.

10. Gilchriest, C. E., "Correlation Functions of Filtered PN Sequences," *SPS 37-16,* Vol. IV, pp. 81–86. Jet Propulsion Laboratory, Pasadena, California, August 31, 1962.

11. Davenport, W., and Root, W., "An Introduction to the Theory of Random Signals and Noise," McGraw-Hill, 1958, Chap. 12.

UNCLASSIFIED

II. Future Missions

1. Mariner Mars 1966 Project

The *Mariner* Mars 1966 Project has been cancelled.

2. Advanced Mariner

The Lockheed Corporation parametric study of orbiter missions has been completed and their final report is in process of preparation. The results of the study provide estimates of the capability of orbiters ranging in gross weight from 1200 to 2200 lb, providing data on the types of experiments which might be carried in this weight range and technical concepts of the spacecraft required to support such experiments. Although the prime intent of the study contract was this parametric analysis, Lockheed was asked to perform a detailed conceptual design at one point on the curve, namely, the 2200 lb level. This design was completed and was used primarily as a check on the general parametric results obtained.

A comparable study in landers is in its final month at the Avco Corporation. The same weight range is being studied as in the case of the Lockheed contract, although the mission in this case is a flyby/capsule combination. The effort is scheduled to be completed by the end of September with the final report due the end of October.

In-house at JPL the capsule study effort which has been under way for several months has been somewhat reduced in scope due to reassignment of personnel; however, the effort is still continuing and is expected to yield primarily an understanding of the critical problem areas to be faced when a capsule mission is formally initiated.

As a result of a directive from NASA Headquarters during July, an orbiter study team has been organized at the Laboratory. The prime function of this study team is to determine the feasibility of an orbiter mission for the 1969 Mars opportunity. The results of this study will be used by NASA Headquarters in the determination of the 1969 mission.

Concurrent with the above studies, a *Mariner* 1969 Project Office is being organized at JPL, and preparations

are being made to begin Project operations with a request for proposal (RFP) to industry in December of this year.

3. Voyager

The *Titan III-C Voyager* spacecraft study has been completed by the General Electric Company and the final report has been submitted. During this current reporting period a supplement to this contract was processed and General Electric is now performing a comparable study of possible *Voyager* missions to be conducted with the *Saturn V* launch vehicle. The study is primarily a parametric analysis evaluating the capabilities of a spacecraft carrying from 500 to 5,000 lb of scientific instruments. This study is of four months' duration and is scheduled for completion by the end of November of this year.

Upon completion of this study, JPL plans to organize an in-house *Voyager* study team to summarize the results of past *Voyager* studies on the *Titan III-C*, three-stage *Saturn I-B*, and the *Saturn V* launch vehicles for submission to NASA Headquarters to assist in the determination of the launch vehicle to be selected for the *Voyager* Project. This selection is scheduled for early 1965.

4. Comets and Asteroids

During the past reporting period the two industry studies mentioned in the last *SPS* were initiated.

Philco Western Development Laboratories have received a contract from JPL to perform mission studies of comets and near asteroids which can be reached by low-energy boost vehicles.

Lockheed Missiles and Space Company, of Sunnyvale, California, has been assigned the study of high-energy asteroid missions with a possible Jupiter flyby as an ultimate limit to these missions. Both studies are now under way and initial results will be available shortly.

5. High-Energy Missions

Statements of Work for RFPs to industry are currently in the course of preparation for the initial mission studies of possible high-energy missions such as probes and orbiters of Jupiter, Jupiter's moons, Mercury missions, and out-of-the-ecliptic shots. These RFPs are scheduled for submission to industry early in 1965.